UNIVERSITY OF CALIFORNIA

Santa Barbara

Quantitative Analysis for Efficiency Studies in III-Nitride Light Emitting Diodes (LEDs) using Electron Emission Spectroscopy (EES)

A dissertation submitted in partial satisfaction of the

requirements for the degree Doctor of Philosophy

in Materials

by

Wan Ying Ho

Committee in charge:

Professor James S. Speck, Co-Chair

Professor Claude Weisbuch, Co-Chair

Dr. Jacques Peretti, École Polytechnique, Paris, France

Professor Christopher J. Palmstrøm

September 2022

The dissertation of Wan Ying Ho is approved.

_____

Christopher J. Palmstrøm

_____

Jacques Peretti

_____

Claude Weisbuch, Committee Co-Chair

_____

James S. Speck, Committee Co-Chair

August 2022

ACKNOWLEDGEMENTS

I thank

The cleanroom staff, for their godly aid

The committee, for guidance unswayed

Keeping my nerves from, being frayed

I thank

My adorable cat, for existing

My family, silently, yet firmly supporting

My friends, together laughing

And of course, I thank

My funding agencies

Support at UCSB was provided by the Solid State Lighting and Energy Electronics Center (SSLEEC); the University of California, Santa Barbara (UCSB) – Collaborative Research of Engineering, Science and Technology (CREST) program; U.S. Department of Energy under the Office of Energy Efficiency & Renewable Energy (EERE) Award Nos. DE-EE0007096 and DE-EE0009691; the Simons Foundation (Grant #s 601952 and 601954 for JSS and CW, respectively); the National Science Foundation (NSF) RAISE program (Grant No. DMS-1839077 for JSS and CW); and Sandia National Laboratory (Award # 2150283). A portion of this work was performed at the UCSB Nanofabrication facility.

VITA OF WAN YING HO
August 2022

EDUCATION

Master of Physics in Physics, University of Oxford, July 2014
Doctor of Philosophy in Materials, University of California, Santa Barbara, September 2022 (expected)

PROFESSIONAL EMPLOYMENT

Summer 2012: Summer Internship, Freescale Semiconductor Ltd., Glasgow
2014-2016: Graduate Research Assistant, Nanotechnology and Catalysis Centre, University of Malaya
Winter 2018: Teaching Assistant, Department of Materials, University of California, Santa Barbara
Fall 2021: Teaching Assistant, Department of Materials, University of California, Santa Barbara

PUBLICATIONS

D. J. Myers, K. Gelžintė, **W. Y. Ho**, J. Iveland, L. Martinelli, J. Peretti, C. Weisbuch, and J. S. Speck, "Identification of low-energy peaks in electron emission spectroscopy of InGaN/GaN light-emitting diodes," *Journal of Applied Physics* **124 (5)**, 005703 (2018).

J. Wang, E. C. Young, **W. Y. Ho**, B. Bonef, T. Margalith, and J. S. Speck, "III-nitride blue light-emitting didoes utilizing hybrid tunnel junction with low excess voltage," *Semiconductor Science and Technology* **35 (12)**, 1125026 (2020).

C. LYnsky, R. C. White, Y. C. Chow, **W. Y. Ho**, S. Nakamura, S. P. DenBaars, and J. S. Speck, "Role of V-defect density on the performance of III-nitride green LEDs on sapphire substrates," *Journal of Crystal Growth* **560**, 126048 (2021).

W. Y. Ho, Y. C. Chow, D. J. Myers, F. Wu, J. Peretti, C. Weisbuch, and J. S. Speck, "Quantitative correlation of hot electron emission to Auger recombination in the active region of *c*-plane blue III-N LEDs," *Applied Physics Letters* **119 (5)**, 051105 (2021).

E. Farzana, F. Alema, **W. Y. Ho**, A. Mauze, T. Itoh, A. Osinky, and J. S. Speck, "Vertical *β*-Ga_2O_3 field plate Schottky barrier diode from metal-organic chemical vapor deposition," *Applied Physics Letters* **118 (16)**, 162109 (2021).

K. S. Qwah, M. Monavarian, **W. Y. Ho**, Y.-R. Wu, and J. S. Speck, "Vertical hole transport through unipolar InGaN quantum wells and double heterostructures," *Physics Review Materials* **6 (4)**, 044602 (2022).

W. Y. Ho, A. I. Alhassan, C. Lynsky, Y. C. Chow, D. J. Myers, S. P. DenBaars, S. Nakamura, J. Peretti, C. Weisbuch, and J. S. Speck, "Detection of hot electrons originating from side valley at ~1.7 eV above the Γ-valley in wurtzite GaN using electron emission spectroscopy (EES)," *submitted*.

W. Y. Ho, Y. C. Chow, S. P. DenBaars, S. Nakamura, J. Peretti, C. Weisbuch, and J. S. Speck, "Measurement of minority carrier diffusion length in *p*-GaN using electron emission spectroscopy (EES)," *in preparation*.

ABSTRACT

Quantitative Analysis for Efficiency Studies in III-Nitride Light Emitting Diodes (LEDs) using Electron Emission Spectroscopy (EES)

by

Wan Ying Ho

As the average luminous efficacy of light emitting diodes (LEDs) has increased over the years, the energy performance of LEDs has surpassed preceding lighting technologies such as incandescent and fluorescent lighting. One way to reduce the cost per lumen.hour would be to maximize the wall-plug efficiency (WPE), where the internal quantum efficiency (IQE), η_{rad}, plays a major role. η_{rad} represents the number of photons created per injected electron-hole (*e*-*h*) pair and is known to peak at a low current density ~1-10 A cm^{-2}. This reduction in efficiency at higher current densities has been referred to as efficiency droop, or simply droop, posing a roadblock to full penetration of the lighting market and for applications in display technologies.

An effective technique to study efficiency droop is electron emission spectroscopy (EES). EES is capable of measuring and detecting hot electrons generated in the active region of an LED, thus allowing direct investigation of the recombination, and scattering processes in the device. Electrons were detected to be emitted from a side valley at ~0.9 eV above the Γ-valley of GaN, which can only be generated by Auger recombination. The intensity of these hot

electrons was showed to increase with increasing droop, thereby providing direct evidence of Auger recombination as the cause of droop.

The work presented here concerns taking the experimental technique towards a full quantitative approach. Using the light output power of an LED as a proxy for active region carrier density n, we were able to directly obtain the power law dependence of the various valley peaks on n, distinguishing between 2-body trap-assisted Auger recombination (TAAR) and 3-body band-to-band Auger combination. Efficiency and thermal droop studies in *c*-plane blue and green III-nitride LEDs were made to quantify the prevalence of TAAR and investigate the sources of the defects. We report on detection of a new high energy upper valley at ~1.7 eV above Γ-valley, which was predominantly generated by TAAR. Its detection was contingent on a low number of pre-well InGaN/GaN superlattice (SL) period, higher [In] quantum wells, and presence of AlGaN in the active region – indicating the defect reduction capabilities of SLs and presence of a deep trap at the AlGaN/(In)GaN interfaces. Through systematic thinning of the *p*-region by growth or by *ex-situ* etching, we present work leading towards obtaining the absolute TAAR and 3-body Auger electron currents for full LED recombination physics quantification.

Table of Contents

I. Introduction

A. Wurtzite III-Nitride Light Emitting Diodes

As the average luminous efficacy of light emitting diodes (LEDs) has increased over the years, the energy performance of LEDs has surpassed preceding lighting technologies such as incandescent and fluorescent lighting. According to the United States Department of Energy 2022 Solid-State Lighting R&D Opportunities report, in the U.S. alone the adoption of solid-state lighting (SSL), which encompasses LEDs, has saved 185 billion kWh per year.[1] Not only do LEDs have direct impact on the climate due to reduction in CO_2 emissions, they can be easily integrated into intelligent lighting systems for grid load reduction and more energy efficient buildings.[1]

The white LEDs we see in the market mainly consist of III-nitride LEDs – they are made up by layers of aluminium nitride (AlN), gallium nitride (GaN), indium nitride (InN) and alloys of these three materials. As semiconductors, these materials contain bands of energy states in which electrons are allowed to travel, as depicted in Fig. 1.1. These bands are separated by a forbidden gap, where no allowed states exist in, called the *band gap*. The top band is called the *conduction band* (CB) and is mostly unoccupied, while the bottom band is called the *valence band* (VB) and is mostly occupied by *electrons* which has negative charge. Since an electron travelling in the VB requires an empty state to be vacated by another electron first, one can more conveniently represent the flow of carriers by the empty states in the VB

compared to tracking all the electrons. These can be represented as *holes*, which are positively charged.

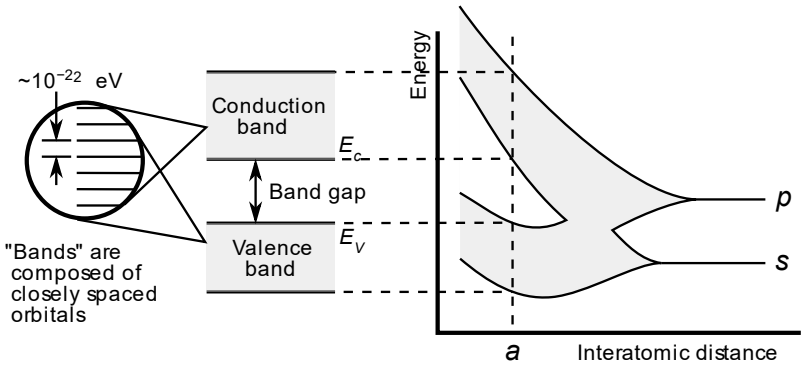

Figure 1.1: Atoms have orbitals in which electrons reside, such as the *s*-orbital and *p*-orbital. When a large number of atoms are brought close to each other, their orbitals begin to overlap and their separation in energy are so small it can be thought of as continuous bands. Picture reproduced from Ref. 2.[2]

It is possible for an electron from the conduction band to fall into the VB and recombine with a hole. When this happens the electron loses energy, which can be released in the form of a photon, or light. This is the foundation to light emitting diodes. Such phenomenon can be encouraged by forming heterojunctions – by introducing spatial confinement using dissimilar materials to increase the likelihood of an electron meeting a hole. An example of a simple unbiased LED structure is shown in Fig. 1.2, where an InGaN quantum well (QW) is sandwiched between a *p*-doped GaN layer and an *n*-doped GaN layer. The GaN layers confine the electrons in the InGaN quantum well. Doping was achieved by introducing specific impurities into the material, either to add surplus holes (*p*-doped) or electrons (*n*-doped). The difference in doping and charge changes the Fermi level, E_F of the material which is defined as the energy level which has 50% probability of being occupied at thermodynamic

equilibrium. At zero bias, the Fermi levels of the different material segments in Fig. 1.2 must align as it is at thermodynamic equilibrium. There is a potential barrier for electrons from travelling from the *n*-region to the *p*-region, and for holes from the *p*-region to the *n*-region. By applying a voltage across the device, we can reduce this barrier and allow carriers to travel down a concentration gradient, much like heat travelling from a hotter to a colder. When sufficient voltage is supplied, a significant amount of current will flow , turning on the diode.

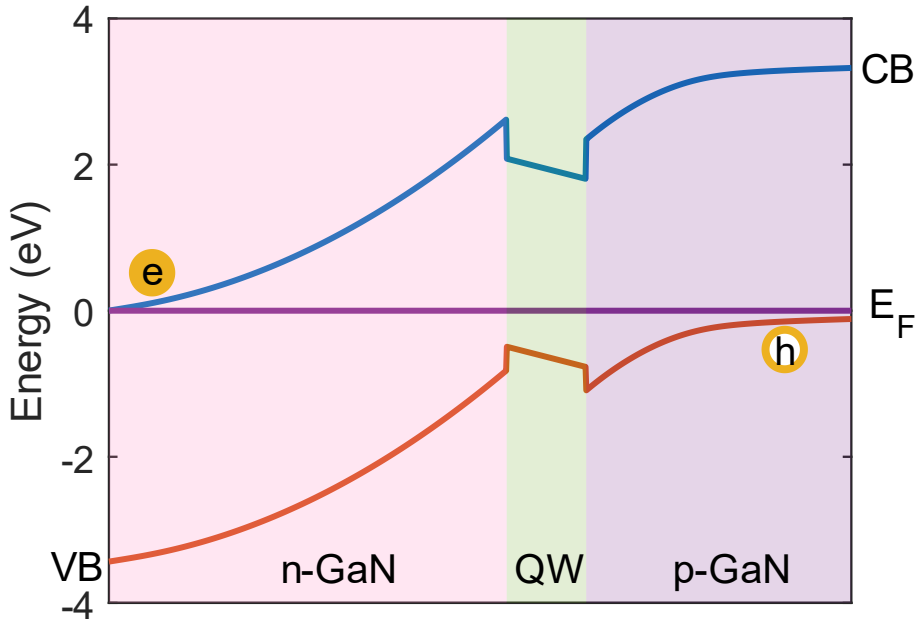

Figure 1.2: Band diagram of a simplistic III-nitride LED at zero bias. The CB, VB and E_F are drawn as blue, orange, and purple lines, respectively. Electrons predominantly travel from the electron rich *n*-GaN to the electron depleted *p*-GaN in CB down a concentration gradient, and vice versa for holes in the VB.

The color of the LED is determined by the energy released when the electron recombines with the hole. In general, this implies that the wavelength is decided by the band gap, E_G of

the confining material, i.e. the quantum well. For wurtzite III-nitrides, AlN, GaN and InN have band gaps of 6.12 eV (203 nm),[3,4] 3.4 eV (364 nm),[5,6] and 0.85 eV (1459 nm) at room temperature,[7,8] respectively. We can engineer the band gap by alloying between the ultraviolet (UV) AlN or GaN with the infrared (IR) InN to obtain light spanning the entire visible spectrum (400 to 700 nm).

It is important to discuss the meaning of these materials being of wurtzite crystal structure. When the numerous atoms are brought close together, they form bonds with one another which require the atoms to rearrange themselves physically into a specific structure. In the case of III-nitride for LEDs, the crystal structure of interest is called a wurtzite, as shown in Fig. 1.3 (a).

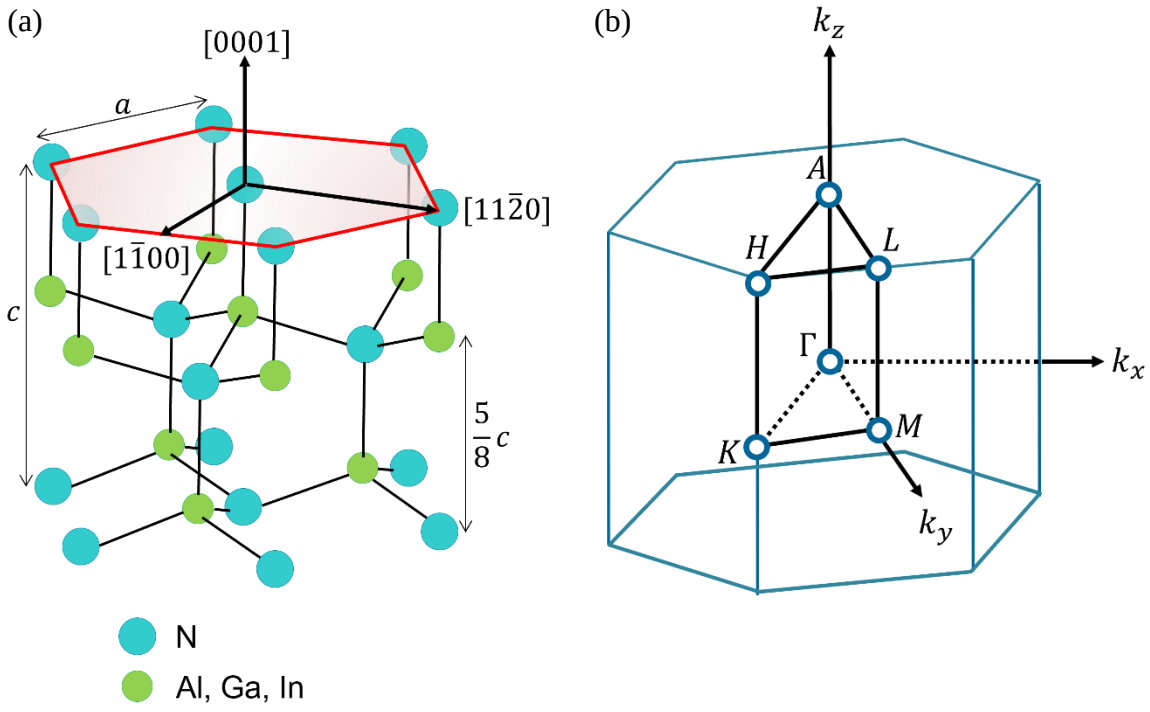

Figure 1.3: (a) A hexagonal unit cell for wurtzite crystal structure with the atom positions detailed. Lattice constants are labelled as a and c. The c-plane is shaded in red/pink. The corresponding unit

cell in momentum space ($\vec{k}$-space), known as the Brillouin Zone is drawn in (b), where high symmetry points are labelled.

If one takes the unit cell as a building block and stack multiples of it, one obtains a massive periodic landscape of atoms and potentials. An electron travelling in this periodic landscape will hence have energy E and momentum $\vec{k}$ restrictions placed upon them by the periodic landscape. This specific set of allowed states $E(\vec{k})$ is unique to each crystal structure and material and is known as the *bandstructure* of a material. Once again, the allowed states are shown to gather into the conduction band and valence band, separated by a band gap.

In the case of wurtzite GaN, the material is classified as a direct band gap semiconductor – meaning its conduction band minimum and the valence band maximum are located at the same crystal momentum $\vec{k}$, which happens to be at the Γ point, or $\vec{k} = (0,0,0)$. If one is to plot the $E(\vec{k})$ diagram about the Γ point, one will find a conduction band valley at the Γ point (Γ-valley). Such valleys are located at various $\vec{k}$ which typically coincides with a high symmetry point in the corresponding momentum unit cell, as depicted in Fig. 1.3 (b). Interestingly, while the band gap of GaN is well determined,[5,6] the rest of the energy and positions of the conduction band valleys remains a topic of debate, arising from disagreements between calculations and experimental results.[5,6,9–13] The measurement of electrons originating from these valleys, or lack thereof, is essential in EES, and shall be discussed in later sections.

B. Efficiency Droop

With the general physics for a III-nitride LED outlined, we return our attention to energy savings enabled by use of LEDs. One way to reduce the cost per lumen.hour would be to maximize the wall-plug efficiency (WPE), where the internal quantum efficiency (IQE), η_{rad}, plays a major role. η_{rad} represents the number of photons created per injected electron-hole (*e*-*h*) pair and is known to peak at a low current density ~1-10 A cm^{-2}. This reduction in efficiency at higher current densities has been referred to as efficiency droop, or simply droop.

To date, the dominant mechanism of droop remains a topic of debate.[14–17] The ABC model is commonly used to describe the shape of the IQE curve in discussions of efficiency droop. A carrier in the quantum well can undergo either: (i) Shockley-Read-Hall (SRH) recombination; (ii) radiative recombination; or (iii) band-to-band Auger recombination, as shown schematically in Fig. 1.4.

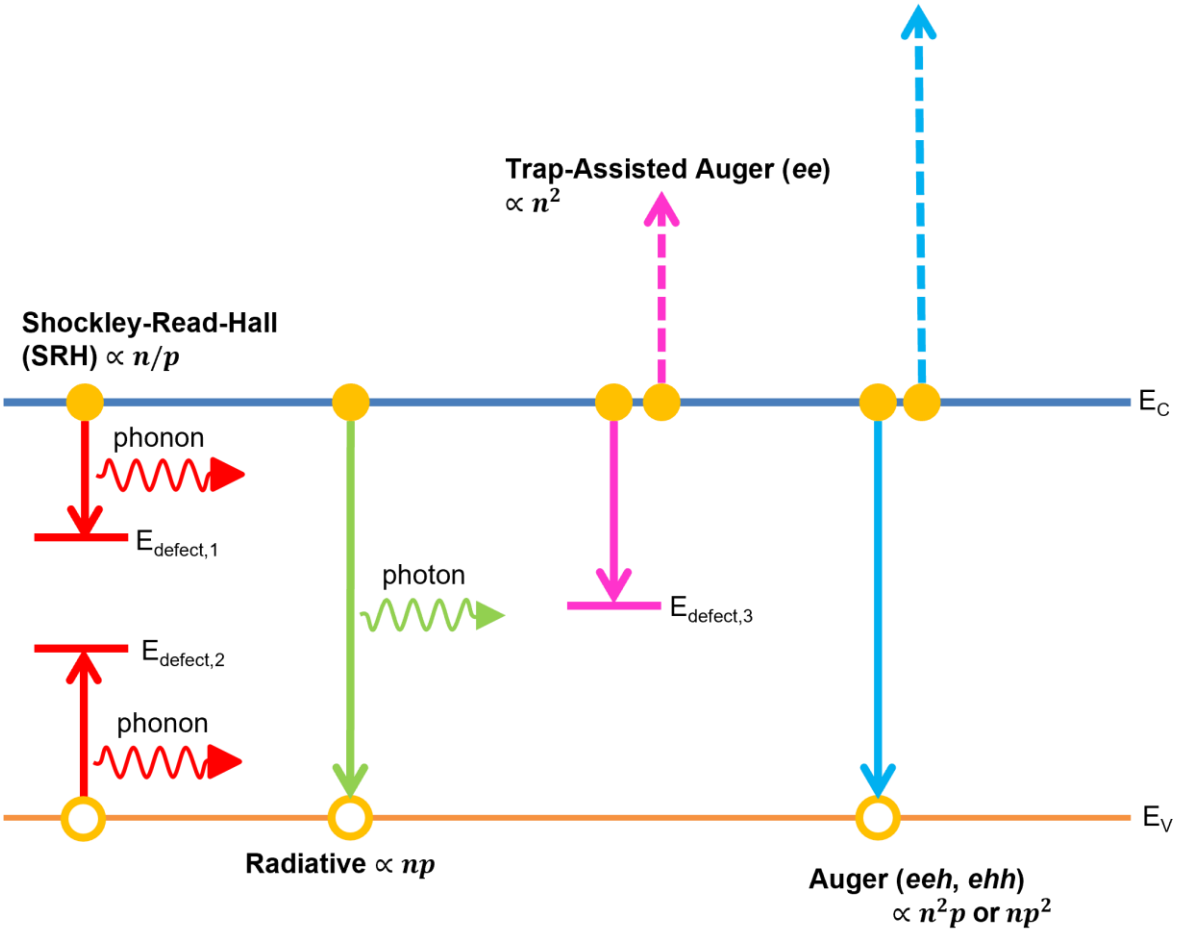

Figure 1.4: Depiction of Shockley-Read-Hall (SRH), radiative, trap-assisted Auger (*ee*), and traditional 3-body *eeh* Auger recombination.

In the SRH deep-trap model, presence of traps facilitates loss of carriers from the conduction band E_c and valence band E_v via recombination with these traps.[18,19] The expected dependence on carrier density n is hence linear, as only one carrier was required for the process. It was experimentally verified that the dependence on n was linear.[18,20–22] The second possible recombination mechanism is radiative recombination. This is the desired outcome in the case of LEDs, where an electron recombines with a hole releasing energy in the form of a photon. When n is large, there is a high probability of an additional electron or hole in

proximity of the recombining electron-hole pair. Under such conditions the released energy may be absorbed by the nearby electron/hole, which is then excited to a higher band. It is typically taken that the electron carrier density is the same as the hole density, ie. $n = p$. In the ABC model, the IQE is hence given as:

$$\eta_{rad} = \frac{Bn^2}{An + Bn^2 + Cn^3} \tag{1.1}$$

with corresponding current densities:

$$J = qd_{QW}(An + Bn^2 + Cn^3) \tag{1.2}$$

$$= J_{SRH} + J_{rad} + J_{eeh\ Auger}$$

where q is the fundamental charge, d_{QW} the thickness of the active region, while A, B and C are the SRH, radiative and 3-body Auger recombination coefficients, respectively. The carrier density at which η_{rad} peaks is at $n^* = \sqrt{A/C}$, with corresponding current density at:

$$J^* = qd_{QW}\left(2A\sqrt{\frac{A}{C}} + B\frac{A}{C}\right) \tag{1.3}$$

A typical use of Eq. 1 is to first measure the radiative coefficient B using time-resolved photoluminescence (TRPL) techniques and then fit the measured IQE to obtain SRH and 3-body Auger coefficients A and C. Clearly the fit will be non-unique as there are two unknowns to a single equation. The disagreements extend beyond data fitting into theoretical results on calculated indirect phonon assisted Auger recombination rates, with values ranging from 10^{-34} to 10^{-31} cm^6 s^{-1}.[14,23] At the same time, this simplistic model does not account for other forms of non-radiative loss.[15,23,24]

One of the non-radiative mechanisms that is recently gaining traction is trap-assisted Auger recombination (TAAR) (see Fig. 1.4), which is not considered in the simplistic ABC model. It can be understood as energy released by a SRH recombination event being absorbed by a nearby carrier, hence will scale as n^2. Equations 1.1 and 1.2 are hence modified to be:

$$\eta_{rad} = \frac{Bn^2}{An + Bn^2 + B'n^2 + Cn^3} \tag{1.4}$$

$$J = qd_{QW}(An + Bn^2 + B'n^2 + Cn^3) \tag{1.5}$$

$$= J_{SRH} + J_{rad} + J_{TAAR} + J_{eeh\ Auger}$$

Note that the carrier density at which η_{rad} peaks remain at $n^* = \sqrt{A/C}$ after inclusion of TAAR, but the peak amplitude is reduced. The corresponding current density at which η_{rad} peaks is now:

$$J^* = qd_{QW}\left(2A\sqrt{\frac{A}{C}} + (B + B')\frac{A}{C}\right) \tag{1.6}$$

Clearly J^*, which is a measurable quantity, is a strong indicator of the magnitude of A and the relative defect densities in an LED. It is important to mention that thus far in the derivation of J^* it has been assumed, as with the ABC model, that the coefficients are independent of carrier density, which was shown by theory and experiments as untrue.[25,26]

Another shortcoming of the simplistic ABC model is the failure to consider overflow current, which is a major category of mechanisms proposed as cause of efficiency droop. Overflow current corresponds to carriers that were injected into the active region but survived to the *p*-region without undergoing any recombination. This includes carrier leakage – where the carrier escaped from the quantum wells, as well as overshoot – where carriers ballistically

bypass the quantum wells.[24,27–29] Photoluminescence (PL) measurements led to ambiguous conclusions on occurrence of carrier leakage, further complicating the attempt to explain droop.[24,27–30]

As such it is unsurprising that a huge range of mechanisms have been proposed to explain this phenomenon in group III-nitrides LEDs, some of which include carrier overflow from the active regions, defect-assisted tunneling, carrier localization and carrier delocalization.[14–17,23,24]

C. "The Green Gap"

A key potential application for III-Nitride LEDs is for micro and flexible displays, where pixels are each made from micrometer-sized LEDs (μLEDs) of red, green, and blue wavelengths. Being self-emissive, InGaN μLEDs has advantage over liquid crystal display technology by bypassing the need for slow and expensive filters.[31–34] Compared to organic LEDs (OLEDs), another self-emissive technology, LEDs are more efficient and stable.[31,32]

However, there are many challenges on the path to realization of such display technology. Firstly, to meet both the light output power requirement and size constraints of each pixel, the onset of droop must be delayed. This further emphasizes the need to understand droop not just in blue LEDs, but also in green and in red. For power and energy efficiency purposes, the voltages of these LEDs should be as low as possible, which is yet another challenge for growth and fabrication.

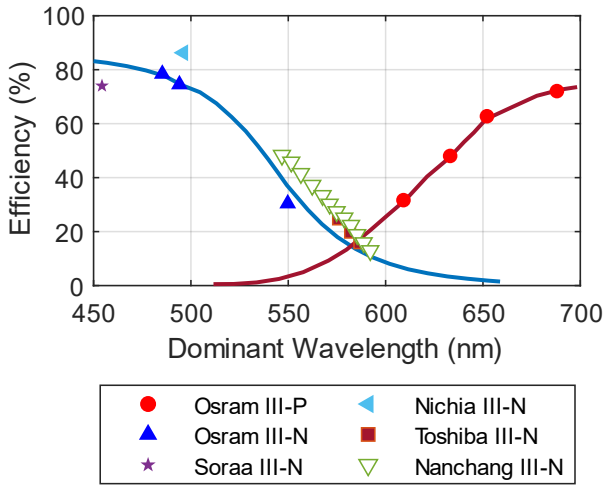

Figure 1.5: The external quantum efficiencies of various LEDs taken from numerous literature sources, while lines are drawn to guide the eye. Filled symbols correspond to peak efficiencies while open symbols correspond to efficiencies at 20 A cm^{-2}.[35–40]

Secondly, for material and fabrication cost reasons the μLED displays should be monolithic, that is, the LEDs are all made from the same material. III-nitrides are shown to have lower surface recombination velocity than III-phosphides, and different compositions of InGaN QWs can produce light spanning the full visual spectrum, making it the most promising material candidate. In either case, the efficiencies of LEDs are known to decrease towards the greener wavelengths as shown in Fig. 1.5. This is known as the "green gap", whose physical origin is not well understood.

Auf der Maur *et al*. proposed that the radiative recombination coefficient decreases with increasing alloy fluctuation due to reduced effective electron-hole wavefunction overlap.[41] Similarly increased polarization fields and in-plane carrier localization was suggested as causes of the "green gap" by reducing wavefunction overlap.[42,43] Studies showed that point

defects increase with increased In content, which will lead to increased Shockley-Read-Hall (SRH) coefficient.[44,45] David *et al*. demonstrated that there is a corresponding increase in a defect-assisted Auger recombination process.[26]

D. Electron Emission Spectroscopy (EES)

With all the uncertainties in theoretical calculations, data fitting and experimental data, there is a drive for new experimental techniques to probe and understand the problems plaguing LEDs. Electron Emission Spectroscopy (EES) was hence proposed and employed to understand efficiency droop LEDs.

As the name suggests, in EES electrons are injected electrically into a sample of interest and the energy spectrum of the emitted electrons is then investigated. The design and operation are detailed in Appendix A, as well as in references 33 – 35.[13,46,47] The measurements of hot electrons are made possible by utilizing a phenomenon known as negative electron affinity (NEA), where the vacuum level, E_{vac} is below the bulk conduction band minimum, as depicted in Fig. 1.6.

In some material systems, NEA can be achieved by sufficient downwards band-bending using heavy *p*-doping, while in others additional activation step(s) are required. For III-nitrides, the activation step involves a submonolayer deposition of Cs on the surface (cesiation). In the case of AlN it was shown that NEA can be obtained regardless of band-bending, while for GaN and InGaN high *p*-doping is necessary.[48–53] For Si, only the [100] surface can be activated,[54–56] while GaAs require multiple alternate doses of Cs and O_2.[57–62] There were reports of p-InGaN achieving NEA with band gap of ~2.8 eV, which unlike the

other III-nitrides, also require the alternating treatment of Cs and O_2 to achieve stable NEA.[63–65] The actual mechanism lying behind the activation processes achieving NEA is still poorly understood and is the subject of extensive literature.[56,66–71]

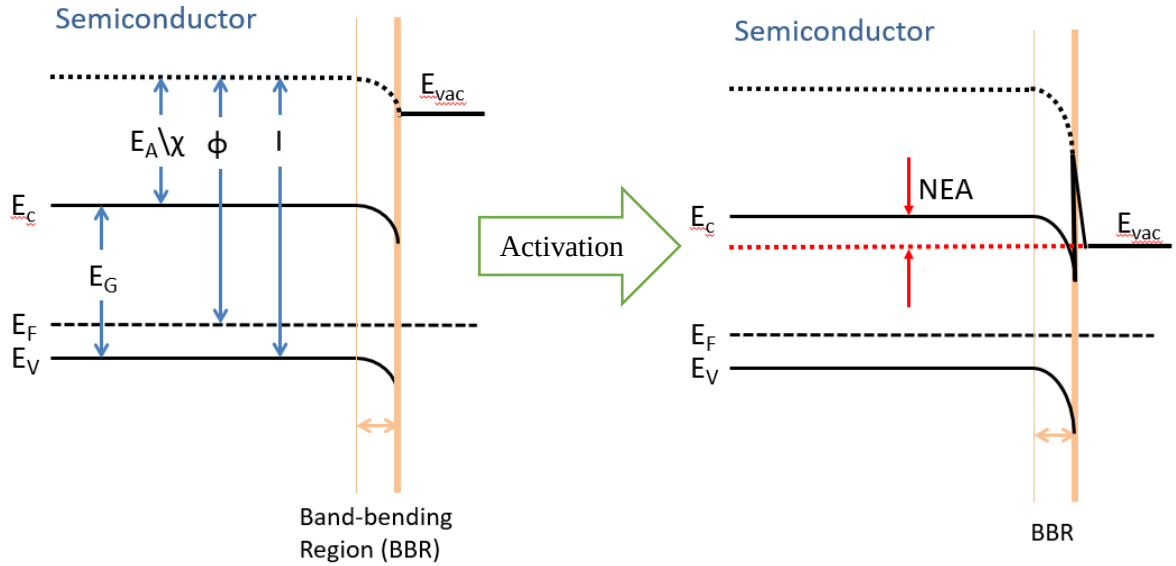

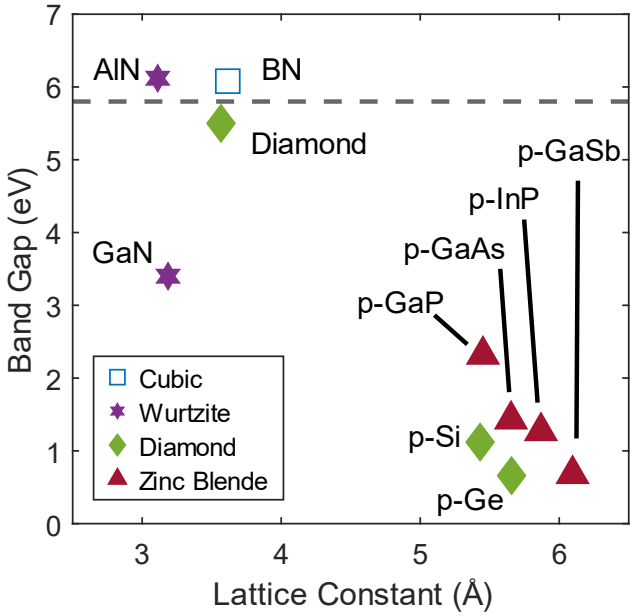

Figure 1.6: (a) The band profiles of a p-doped material before and after activation, achieving NEA, where $E_A\backslash\chi$, Φ, and I are the electron affinity, workfunction and ionization energy of the material,

respectively. (b) Semiconductor materials (excluding alloys) with NEA reported in literature – those with large band gaps are more likely to achieve NEA independent of band-bending.[49,56,57,59,71–74] The dashed line separates those reported to have achieved NEA without activation (above) from those requiring activation (below).

In EES, electrons are typically injected into the *n*-layer of the sample These electrons will then transit, scatter, and/or recombine in the active region as well as the top *p*-layer. As such, the emitted electrons in a sample will provide insight into the band structure of the emitting surface material, as well as the scattering and recombination processes in all the layers transited.

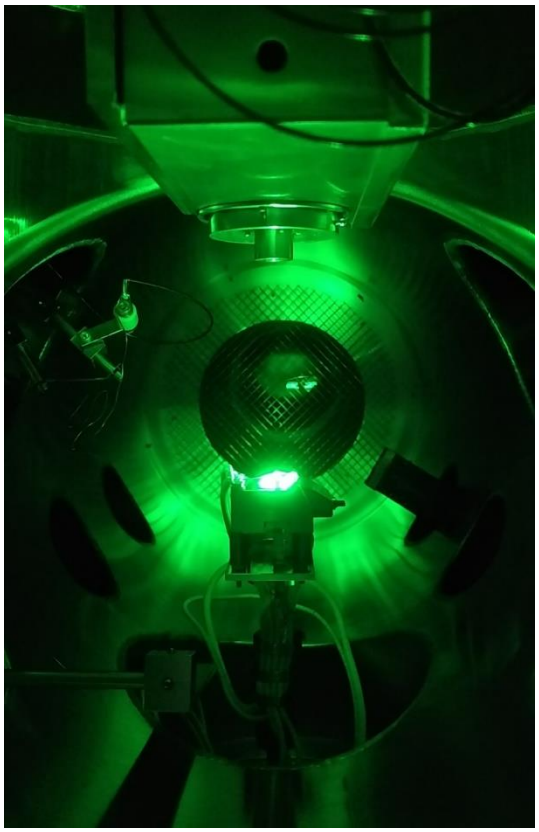

Figure 1.7: A green LED lights up in the chamber during electrical connectivity test as viewed from the top of the analyzer chamber.

References

[1] M. Pattison, M. Hansen, N. Bardsley, G.D. Thomson, K. Gordon, A. Wilkerson, K. Lee, V. Nubbe, and S. Donnelly, *2022 Solid-State Lighting R&D Opportunities* (Office of Energy Efficiency & Renewable Energy, U.S. Department of Energy, 2022).

[2] Wikipedia (2022).

[3] W.M. Yim, E.J. Stofko, P.J. Zanzucchi, J.I. Pankove, M. Ettenberg, and S.L. Gilbert, Journal of Applied Physics **44**, 292 (1973).

[4] J. Li, K.B. Nam, M.L. Nakarmi, J.Y. Lin, H.X. Jiang, P. Carrier, and S.-H. Wei, Appl. Phys. Lett. **83**, 5163 (2003).

[5] S. Bloom, Journal of Physics and Chemistry of Solids **32**, 2027 (1971).

[6] S. Bloom, G. Harbeke, E. Meier, and I.B. Ortenburger, phys. stat. sol. (b) **66**, 161 (1974).

[7] J. Wu, W. Walukiewicz, K.M. Yu, J.W. Ager, E.E. Haller, H. Lu, W.J. Schaff, Y. Saito, and Y. Nanishi, Appl. Phys. Lett. **80**, 3967 (2002).

[8] J. Wu, W. Walukiewicz, W. Shan, K.M. Yu, J.W. Ager, S.X. Li, E.E. Haller, H. Lu, and W.J. Schaff, Journal of Applied Physics **94**, 4457 (2003).

[9] J. Kolník, İ.H. Oğuzman, K.F. Brennan, R. Wang, P.P. Ruden, and Y. Wang, Journal of Applied Physics **78**, 1033 (1995).

[10] M. Suzuki, T. Uenoyama, and A. Yanase, Phys. Rev. B **52**, 8132 (1995).

[11] S. Wu, P. Geiser, J. Jun, J. Karpinski, D. Wang, and R. Sobolewski, Journal of Applied Physics **101**, 043701 (2007).

[12] S. Marcinkevičius, T.K. Uždavinys, H.M. Foronda, D.A. Cohen, C. Weisbuch, and J.S. Speck, Phys. Rev. B **94**, 235205 (2016).

[13] J. Iveland, L. Martinelli, J. Peretti, J.S. Speck, and C. Weisbuch, Phys. Rev. Lett. **110**, 177406 (2013).

[14] V. Avrutin, S. din A. Hafiz, F. Zhang, Ü. Özgür, H. Morkoç, and A. Matulionis, Journal of Vacuum Science & Technology A: Vacuum, Surfaces, and Films **31**, 050809 (2013).

[15] G. Verzellesi, D. Saguatti, M. Meneghini, F. Bertazzi, M. Goano, G. Meneghesso, and E. Zanoni, Journal of Applied Physics **114**, 071101 (2013).

[16] J. Cho, E.F. Schubert, and J.K. Kim, Laser & Photonics Reviews **7**, 408 (2013).

[17] H. Amano, J. Han, H. Morkoc, and T.-Y. Seong, editors , *III-Nitride Based Light Emitting Diodes and Applications*, 1st ed. 2013 (Springer Netherlands : Imprint: Springer, Dordrecht, 2013).

[18] R.N. Hall, Phys. Rev. **87**, 387 (1952).

[19] W. Shockley and W.T. Read, Phys. Rev. **87**, 835 (1952).

[20] G. Bemski, Phys. Rev. **100**, 523 (1955).

[21] J.S. Blakemore, Phys. Rev. **110**, 1301 (1958).

[22] G.B. Abdullaev, Z.A. Iskender-Zade, E.A. Dzhafarova, and V.E. Chelnokov, phys. stat. sol. (b) **21**, 423 (1967).

[23] C. Weisbuch, M. Piccardo, L. Martinelli, J. Iveland, J. Peretti, and J.S. Speck, Phys. Status Solidi A **212**, 899 (2015).

[24] J. Piprek, Phys. Stat. Sol. (a) **207**, 2217 (2010).

[25] R. Vaxenburg, A. Rodina, E. Lifshitz, and A.L. Efros, Appl. Phys. Lett. **103**, 221111 (2013).

[26] A. David, N.G. Young, C.A. Hurni, and M.D. Craven, Phys. Rev. Applied **11**, 031001(R) (2019).

[27] K.J. Vampola, M. Iza, S. Keller, S.P. DenBaars, and S. Nakamura, Appl. Phys. Lett. **94**, 061116 (2009).

[28] S.-H. Lim, Y.-H. Ko, and Y.-H. Cho, Appl. Phys. Lett. **104**, 091104 (2014).

[29] A. David and N.F. Gardner, Appl. Phys. Lett. **97**, 193508 (2010).

[30] M.F. Schubert, J. Xu, Q. Dai, F.W. Mont, J.K. Kim, and E.F. Schubert, Appl. Phys. Lett. **94**, 081114 (2009).

[31] J. Day, J. Li, D.Y.C. Lie, C. Bradford, J.Y. Lin, and H.X. Jiang, in edited by M. Razeghi, E. Tournie, and G.J. Brown (San Francisco, California, USA, 2012), p. 82681X.

[32] K. Ding, V. Avrutin, N. Izyumskaya, Ü. Özgür, and H. Morkoç, Applied Sciences **9**, 1206 (2019).

[33] M.S. Wong, C. Lee, D.J. Myers, D. Hwang, J.A. Kearns, T. Li, J.S. Speck, S. Nakamura, and S.P. DenBaars, Appl. Phys. Express **12**, 097004 (2019).

[34] D. Hwang, A. Mughal, C.D. Pynn, S. Nakamura, and S.P. DenBaars, Appl. Phys. Express **10**, 032101 (2017).

[35] Y. Narukawa, M. Ichikawa, D. Sanga, M. Sano, and T. Mukai, J. Phys. D: Appl. Phys. **43**, 354002 (2010).

[36] M.J. Cich, R.I. Aldaz, A. Chakraborty, A. David, M.J. Grundmann, A. Tyagi, M. Zhang, F.M. Steranka, and M.R. Krames, Appl. Phys. Lett. **101**, 223509 (2012).

[37] S. Saito, R. Hashimoto, J. Hwang, and S. Nunoue, Appl. Phys. Express **6**, 111004 (2013).

[38] M. Broell, P. Sundgren, A. Rudolph, W. Schmid, A. Vogl, and M. Behringer, in edited by K.P. Streubel, H. Jeon, L.-W. Tu, and M. Strassburg (San Francisco, California, United States, 2014), p. 90030L.

[39] K.A. Bulashevich, A.V. Kulik, and S.Yu. Karpov, Phys. Status Solidi A **212**, 914 (2015).

[40] F. Jiang, J. Zhang, L. Xu, J. Ding, G. Wang, X. Wu, X. Wang, C. Mo, Z. Quan, X. Guo, C. Zheng, S. Pan, and J. Liu, Photon. Res. **7**, 144 (2019).

[41] M. Auf der Maur, A. Pecchia, G. Penazzi, W. Rodrigues, and A. Di Carlo, Phys. Rev. Lett. **116**, 027401 (2016).

[42] S. Schulz, M.A. Caro, C. Coughlan, and E.P. O'Reilly, Phys. Rev. B **91**, 035439 (2015).

[43] F. Nippert, S.Yu. Karpov, G. Callsen, B. Galler, T. Kure, C. Nenstiel, M.R. Wagner, M. Straßburg, H.-J. Lugauer, and A. Hoffmann, Appl. Phys. Lett. **109**, 161103 (2016).

[44] A.M. Armstrong, B.N. Bryant, M.H. Crawford, D.D. Koleske, S.R. Lee, and J.J. Wierer, J. Appl. Phys. **117**, 134501 (2015).

[45] S. Hammersley, M.J. Kappers, F.C.-P. Massabuau, S.-L. Sahonta, P. Dawson, R.A. Oliver, and C.J. Humphreys, Appl. Phys. Lett. **107**, 132106 (2015).

[46] J. Iveland, Electron Emission Spectroscopy of InGaN/GaN Light Emitting Diodes, PhD. Thesis, University of California, Santa Barbara, 2015.

[47] D.J. Myers, Electron Emission Spectroscopy of III-N Semiconductor Devices, PhD. Thesis, University of California, Santa Barbara, 2019.

[48] M. Eyckeler, J. Vac. Sci. Technol. B **16**, 2224 (1998).

[49] C.I. Wu and A. Kahn, Journal of Applied Physics **86**, 3209 (1999).

[50] M.C. Benjamin, C. Wang, R.F. Davis, and R.J. Nemanich, Appl. Phys. Lett. **64**, 3288 (1994).

[51] M.C. Benjamin, M.D. Bremser, T.W. Weeks, S.W. King, R.F. Davis, and R.J. Nemanich, Applied Surface Science **104–105**, 455 (1996).

[52] C.I. Wu, A. Kahn, E.S. Hellman, and D.N.E. Buchanan, Appl. Phys. Lett. **73**, 1346 (1998).

[53] T.U. Kampen, M. Eyckeler, and W. Mönch, Applied Surface Science **123–124**, 28 (1998).

[54] F.G. Allen and G.W. Gobeli, Phys. Rev. **144**, 558 (1966).

[55] B. Goldstein, Surface Science **35**, 227 (1973).

[56] J.D. Levine, Surface Science **34**, 90 (1973).

[57] J.J. Scheer and J. van Laar, Solid State Communications **3**, 189 (1965).

[58] A.A. Turnbull and G.B. Evans, J. Phys. D: Appl. Phys. **1**, 155 (1968).

[59] L.W. James and J.L. Moll, Phys. Rev. **183**, 740 (1969).

[60] L.W. James, J.L. Moll, and W.E. Spicer, in *Proceedings of the International Symposium on GaAs*, edited by C.I. Pederson (Institue of Physics and Physical Society, London, 1969), p. 270.

[61] A.H. Sommer, H.H. Whitaker, and B.F. Williams, Appl. Phys. Lett. **17**, 273 (1970).

[62] S. Moré, S. Tanaka, S. Tanaka, Y. Fujii, and M. Kamada, Surface Science **454–456**, 161 (2000).

[63] M. Kashima, D. Sato, A. Koizumi, T. Nishitani, Y. Honda, H. Amano, H. Iijima, and T. Meguro, Journal of Vacuum Science & Technology B **36**, 06JK02 (2018).

[64] M. Kashima, Y. Itokawa, T. Kanai, D. Sato, A. Koizumi, H. Iijima, T. Nishitani, Y. Honda, H. Amano, and T. Meguro, Applied Surface Science **599**, 153882 (2022).

[65] M. Sauty, N.M.S. Lopes, J.-P. Banon, Y. Lassailly, L. Martinelli, A. Alhassan, S. Nakamura, J.S. Speck, C. Weisbuch, and J. Peretti, (2022).

[66] A.F. Milton and A.D. Baer, Journal of Applied Physics **42**, 5095 (1971).

[67] W.E. Spicer, Appl. Phys. **12**, 115 (1977).

[68] M.G. Burt and V. Heine, J. Phys. C: Solid State Phys. **11**, 961 (1978).

[69] F. Machuca, Z. Liu, Y. Sun, P. Pianetta, W.E. Spicer, and R.F.W. Pease, J. Vac. Sci. Technol. B **21**, 1863 (2003).

[70] P. Strak, P. Kempisty, K. Sakowski, and S. Krukowski, Journal of Vacuum Science & Technology A: Vacuum, Surfaces, and Films **35**, 021406 (2017).

[71] V.V. Bakin, S.N. Kosolobov, S.A. Rozhkov, H.E. Scheibler, and A.S. Terekhov, Jetp Lett. **108**, 180 (2018).

[72] F.J. Himpsel, J.A. Knapp, J.A. VanVechten, and D.E. Eastman, Phys. Rev. B **20**, 624 (1979).

[73] B.F. Williams and R.E. Simon, Phys. Rev. Lett. **18**, 485 (1967).

[74] D.G. Fisher, R.E. Enstrom, J.S. Escher, and B.F. Williams, Journal of Applied Physics **43**, 3815 (1972).

II. Quantitative Analysis of Electron Emission in Blue LEDs

A. Correlating hot electron emission to Auger recombination in commercial blue LEDs

The following section is reproduced from W. Y. Ho, Y. C. Chow, D. J. Myers, F. Wu, J. Peretti, C. Weisbuch, and J. S. Speck, "Quantitative correlation of hot electron emission to Auger recombination in the active region of *c*-plane blue III-N LEDs," *Applied Physics Letters* **119 (5)**, 051105 (2021), with the permission of AIP Publishing. The main article has been combined with the supplementary material for clarity.

In 2013, Iveland *et al.* reported direct measurements of hot electrons from higher side valleys using Electron Emission Spectroscopy (EES) and correlated the appearance and intensity of these hot electrons with efficiency droop.[1] In EES, the energy distribution of electrons emitted from an electrically driven semiconductor device, such as an LED, can be measured. By realizing negative electron affinity (NEA) on *p*-GaN through the deposition of Cs or Cs/O complexes, electrons can be emitted even from occupied states near the Γ valley bulk position.[2] While there is little ambiguity in that detection of hot electrons can only be generated by an Auger process, the correlation relied on the extraction of a "supplementary current". The supplementary current was taken as the extra current necessary to realize the measured light output power (LOP) when compared to the "expected" current that would

produce the same LOP in the absence of droop.[1] There is some uncertainty in the procedure defining the supplementary current on which we will improve in the present chapter.

In this work, EES was performed on a commercial blue LED with an improved EES device design for enhanced signal-to-noise ratio.[3] We report on a robust method of analysis that correlates droop with the generation of hot electrons. The blue LED studied in this work was grown using metal-organic chemical vapor deposition (MOCVD). The structure of the epitaxial material is shown in Fig. 2.1.

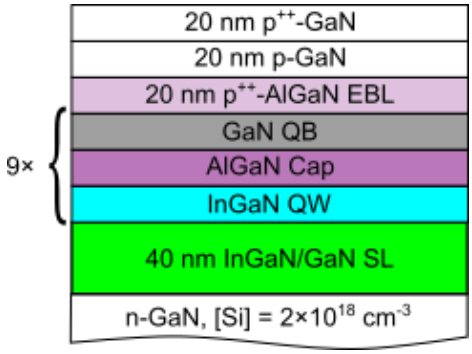

Figure 2.1: Schematic of the epi layer stack for the LED discussed in this article, grown by Seoul VioSys (not to scale).

The Seoul VioSys LED structure was grown on top of a sapphire substrate and an unintentionally-doped (UID)-GaN buffer layer. The subsequent material consisted of an *n*-type GaN:Si layer, 20 nm of InGaN/GaN superlattice, an 8 period multiple quantum well (QW) (InGaN QW/ AlGaN cap layer/ GaN barriers), a 20 nm AlGaN:Mg electron blocking layer (EBL), and finally a 40 nm GaN:Mg ([Mg]~ 2×10^{19} cm^{-3}) with p^{++} contact layer ([Mg]=10^{20} cm^{-3}).

The epitaxial materials were processed into devices suited for EES measurements, cleaned and introduced into the ultra-high-vacuum (UHV) EES set-up as described elsewhere.[1,3] The

epitaxial materials were contacted with 30 nm Pd/ 300 nm Au on the p-GaN in a honeycomb pattern, forming a single EES device of area 0.22 mm^2 with an array of 2257 hexagonal open apertures with an apothem of 3.5 μm separated by 3 μm metal strips.[3] Negative electron affinity (NEA) was achieved by depositing a submonolayer of cesium (cesiation) using a SAES cesium source and optimized by monitoring photoexcited electrons emitted from *p*-GaN.[1] The energy of the electrons was measured with a Comstock AC-901 spherical sector electrostatic analyzer operated in constant pass energy mode with a resolution of 90 meV, referenced to the Fermi level of the *p* contact.[3] As such, with increasing current, there was an increased ohmic voltage drop across the metal-semiconductor interface which shifted the measured energy of electrons emitted from the semiconductor surface to higher values. However, this shift did not affect the Pd and Au photoemission peaks (which are a result of diode light).[1,4] The LOP of the EES device was measured under continuous wave (CW) mode at room temperature using a photodetector. The EQE reached its peak value at approximately 10 A cm^{-2}. EES was performed with the device biased under pulse mode with a 5% duty cycle and 1.7 μs pulses to minimize self-heating, for injection currents ranging from 1 mA to 100 mA corresponding to current densities ranging from 0.45 A cm^{-2} to 45 A cm^{-2}.

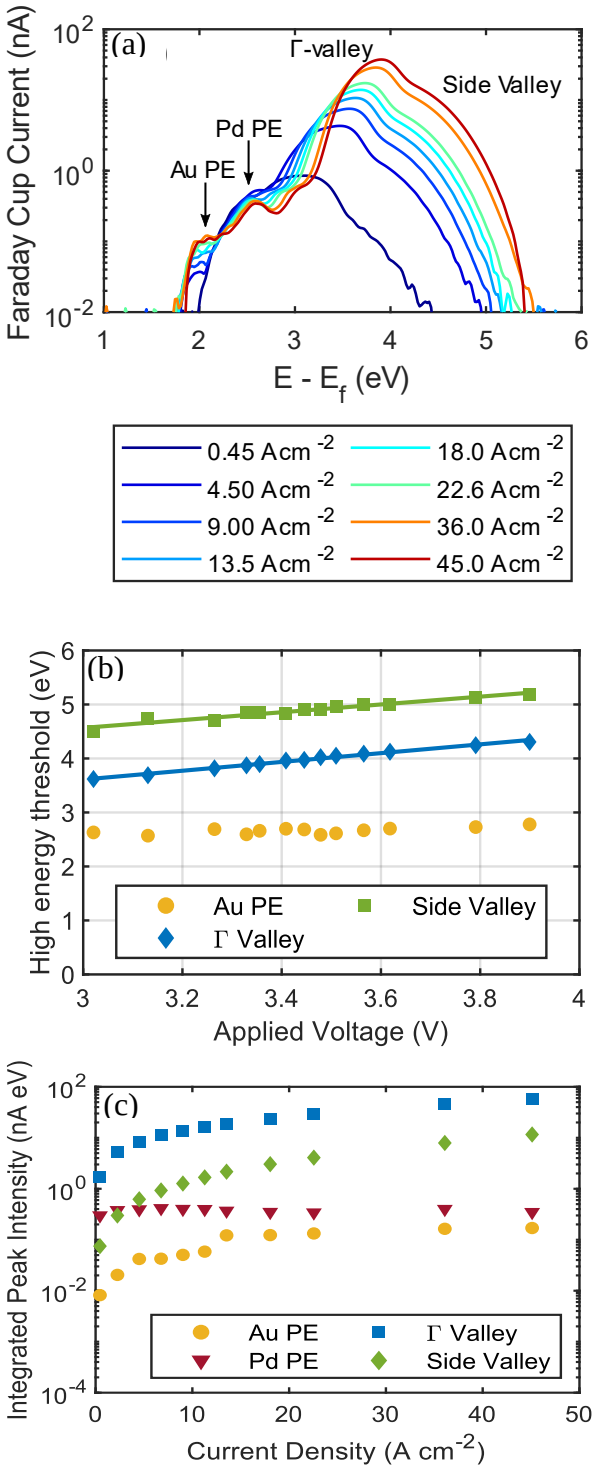

Figure 2.2: The EDCs, peak high energy thresholds, and integrated peak intensities are plotted in (a) – (c) respectively. For all peaks, except Pd PE, the integrated intensities increase with current density.

The Pd PE varied very slightly with increasing current densities but the differences are within EDC background noise levels.

The corresponding energy distribution curves (EDCs) from EES under different currents of are shown in Fig. 2.2(a), where the EDCs for pulsed mode EES were scaled to account for the duty cycle by multiplying with a factor of 20.[1] The EDCs show 4 distinct peaks. Peaks with a semiconductor origin have energies that increase with the applied voltage due to the voltage drop from p-contact to the sample surface.[1,3,5] The extrapolated high energy thresholds at the photon voltage of 2.67 V should correspond to the bulk valley minimum as shown in Fig. 2.2(b).[1,3,5] The high energy thresholds were extracted by taking the extrapolation to zero of the high energy slopes of the derivative EDC, as described in Chapter 3 and Appendix A. Based on the extrapolated values, we assign the measured peaks in increasing energies in the following order: Au PE and Pd PE (both peaks are due to diode light), Γ and first side valley at ~0.9 eV higher energy than Γ.[1,4,6–9] A low energy shoulder appears on Γ valley at high current density, which may be ascribed to thermalization in the band-bending region.[9] The semiconductor related peaks are one or two orders of magnitude larger than our previous works which employed thicker *p*-regions, showing significant improvement in signal-to-noise ratio.[1,3,5,9] This further implied that hot electrons are indeed generated in the bulk region and not by light or other hot electron generation mechanism at the surface.

The magnitude of Γ valley is higher than that of the side valley, unlike previous reported EES spectra of commercial LEDs with much thicker *p*-GaN,[1,3,5,9] but more similar to Ref. 10 where the sample had 85 nm *p*-GaN.[10] This is notable as it suggests that with thinner *p*-GaN more Γ valley electrons successfully reach the sample surface to be emitted. In fact, the side-

valley mainly depopulates by scattering into the Γ valley since the side-valley electrons have very few recombination pathways due to weaker radiative recombination or SRH recombination because of the larger energy difference and limited k-extension of defects.[7] In contrast, electrons in Γ valley, whether scattered from the side-valley or overflowed from the active region, may recombine radiatively or non-radiatively (likely the dominant mechanism) within a diffusion length. One can then assume that the side valley depopulates less during the transit through the p-region to the surface than the Γ valley. Therefore, the ratio of the Γ-valley electron population to the side-valley electron population may increase when decreasing the *p*-GaN layer thickness.

Analytic fits to the EES spectra were performed by superposing four exponentially modified Gaussians (EMGs) to the four EES peaks, respectively.[5] The dependence of the integrated intensities (given as a current) of the four peaks on the LED current density are shown in Fig. 2.2(c). As expected, the integrated peak intensities of Au PE, Γ valley and side valley increases with increasing current density. The Pd PE peak intensity increased initially but remained almost constant at higher current densities, a saturation that was observed in previous work.[3]

(a)

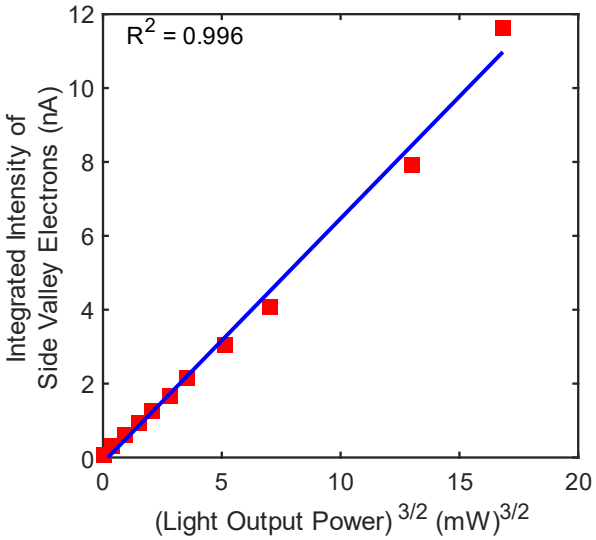
R2 = 0.996
Integrated Intensity of Side Valley Electrons (nA)
(Light Output Power) 3/2 (mW)3/2

(b)

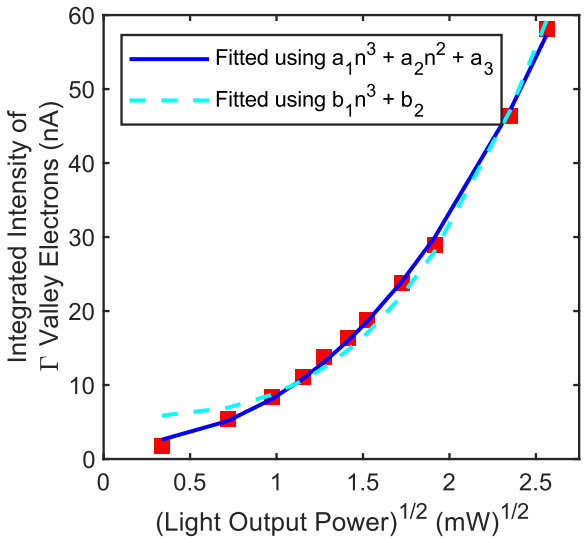
Fitted using a1n3 + a2n2 + a3
Fitted using b1n3 + b2
Integrated Intensity of Γ Valley Electrons (nA)
(Light Output Power)1/2 (mW)1/2

(c)

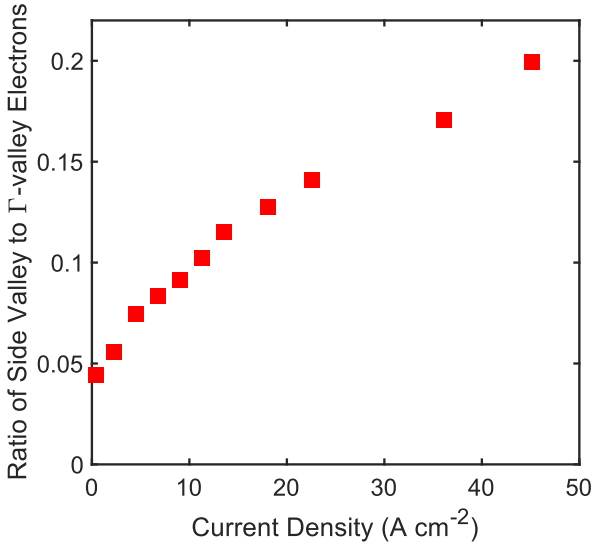
Ratio of Side Valley to Γ-valley Electrons
Current Density (A cm-2)

Figure 2.3: In (a), by comparing the cube of the square root of LOP, which is proportional to n^3 with the side valley peak intensity, a good linear correlation is obtained. In (b), it is found that the Γ valley peak intensities demonstrated a similar cubic dependence of n. A quadratic term is required for improved fit. In (c), the ratio of hot electrons in first side valley to electrons in Γ valley is found to increase with increasing current density, ruling out escape and overshoot as cause of droop.

The Au PE intensities acts like an in-situ photometer,[5] varying linearly with the LOP of the device. Since every electron in the Au PE peak must correspond to one photon emitted by the LED, we expect both the LOP and Au PE peak intensity to vary as radiative recombination rate, hence vary as n^2. Similarly, if hot electrons in the side valley originate from *eeh* recombination, we expect the peak intensity to vary as n^3. Hence the side valley peak intensities should vary linearly as Au PE peak intensity to the power of 3/2. Since the Au PE peaks had been partially masked by Pd PE and semiconductor peaks and hence is subject to fitting errors, a similar analysis was repeated using LOP to the power of 3/2 and comparing to the side valley electron intensity. A good linear fit was obtained with a Pearson's coefficient of 0.992 as shown in Fig. 2.3(b). The produced intercept of 0.02 nA is of the order of the background noise in the EDCs. From the good fits, we conclude that the side valley electrons originate from 3-body *eeh* Auger events. Interestingly, the intensity of Γ valley electrons demonstrated a partial cubic dependence of n at higher current densities. A least square curve fit is attempted instead where the fits are bounded to only return positive coefficients for n^2 and n^3 terms to keep the analysis physically viable. No n term is included as Shockley-Read-Hall recombination is incapable of generating hot electrons. The fit was improved significantly when a quadratic term is included into the fit, with the norm of residuals

decreasing from 33.7 to 4.0, and intercept tending towards zero from 5.75 to 1.97 nA. While introducing a lower power term is expected to improve fits at lower current densities, the fit is improved even past the peak EQE in the droop regime. This n^2 dependence of hot electrons may be attributed to trap-assisted Auger recombination (TAAR).[5,10,11]

At the same time, the LED has EBL in its structure, which is expected to mitigate both escape and overshoot of electrons from the active region.[12] Simulations also showed that leakage currents are small compared to Auger currents.[13] Should either phenomenon be present, we should detect these events as presence of Γ valley electrons in the EDCs as they will not have enough energy to reach the side valley.[6] If either were the dominant cause of droop, we would expect the peak intensities of Γ valley to increase relative to the side valley peak with increasing current density. As shown in Fig. 2.3(c), this is not the case, strongly indicating that the rate of increase of escape and overshoot currents with increasing current density must be low compared to that of Auger currents and should not cause droop. Combining this knowledge with the carrier density dependence of Γ valley electrons, it is possible that the source of detected Γ valley electrons is either by scattering of Auger electrons from the side valley, or by 3-body *eeh* or 2-body TAAR events.[5,10,11] Given the n^3 dependence of 3-body Auger recombination, it is expected that Auger recombination current will dominate rapidly over radiative recombination current with increasing injected carrier density. The presence of detected side valley electrons even at very low current densities implies that the Auger recombination current is significant in magnitude and should lead to droop.[1,9] Thus, we conclude that droop in this LED must be hence dominantly caused by Auger recombination.

In conclusion, we have measured hot electrons from a higher energy side valley in addition to those from the conduction band minimum with vastly improved semiconductor peak signal-

to-noise ratio attributed to reduced electron loss due to use of thinner *p*-GaN. By integrating peaks and investigating the correlation of their intensities with the LOP, we have proven that hot electrons originate dominantly from a 3-body event. This further confirms that droop is dominantly caused by Auger recombination.

The analysis performed above was built on one commercial blue *c*-plane light emitting diode (LED) grown using metal-organic chemical vapor deposition (MOCVD) by Seoul VioSys in 2019. In the following paragraphs we show that the analysis applies to other commercial blue *c*-plane LEDs from a different supplier or year of fabrication. The various structures of the epitaxial materials are shown in Fig. 2.4.

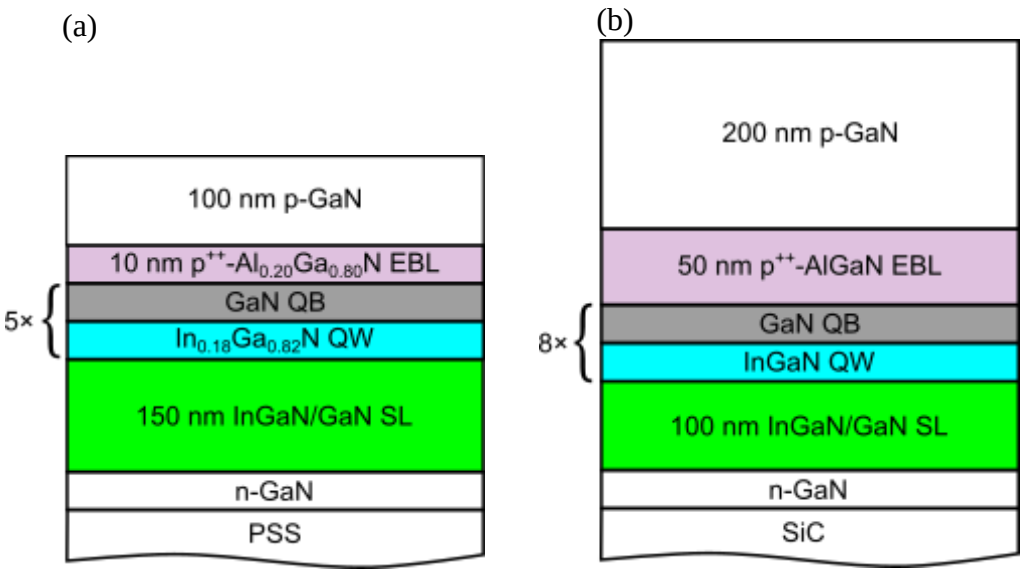

Figure 2.4: Schematic of the epi layer stack for the LEDs discussed in this article, grown by (a) Seoul VioSys in 2013 and (b) Cree in 2016 (not to scale).

The 2013 Seoul VioSys LED structure was grown on top of a patterned sapphire substrate and an unintentionally-doped (UID)-GaN buffer layer. The subsequent material consisted of

an *n*-type GaN:Si layer, 150 nm of InGaN/GaN superlattice, a 5 period multiple quantum well (QW) (InGaN QW/ GaN barriers), a 10 nm AlGaN:Mg electron blocking layer (EBL) with [Mg] = 10^{20} cm^{-3}, and finally a 100 nm GaN:Mg (with [Mg] = 10^{20} cm^{-3}) with contact layer.[3–5]

The 2016 Cree LED structure was grown on top of a silicon carbide (SiC) substrate and an unintentionally-doped (UID)-GaN buffer layer. The subsequent material consisted of an *n*-type GaN:Si layer, 100 nm of InGaN/GaN superlattice, an 8 period multiple quantum well (QW) (InGaN QW/ GaN barriers), a 50 nm AlGaN:Mg EBL ([Mg] = 10^{20} cm^{-3}), and finally a 200 nm GaN:Mg ([Mg] = 10^{20} cm^{-3}) with contact layer.

The epitaxial materials were processed into devices and measured using electron emission spectroscopy (EES) as described in the paper.[3] The corresponding energy distribution curves (EDCs) from EES under different currents of are shown in Figs. 2.5(a) and (b) respectively for the 2013 Seoul VioSys and 2016 Cree LEDs, where the EDCs for pulsed mode EES were scaled to account for the duty cycle.[1] The EDCs show 4 distinct peaks for both LEDs. For 2013 Seoul VioSys, by extracting the high energy thresholds (HETs) and extrapolating as described in the paper the peaks were assigned, in increasing energies, in the following order: Au PE and Pd PE (both peaks are due to diode light), a peak associated to the band-bending region and lastly Γ.[1,3–10] The HET of the Pd PE peak appears to track diode voltage initially, only to separate from the BBR peak as current density increases. The BBR HET continued this tracking behaviour while the Pd PE HET remained almost constant. This is evidence that at low current density the two peaks are both present but highly convolved. For the 2016 Cree LED, the peaks were assigned to be Au PE, 2 peaks due to Pd PE (possibly from the shape of Pd's density of states), and Γ.[1,3–10]

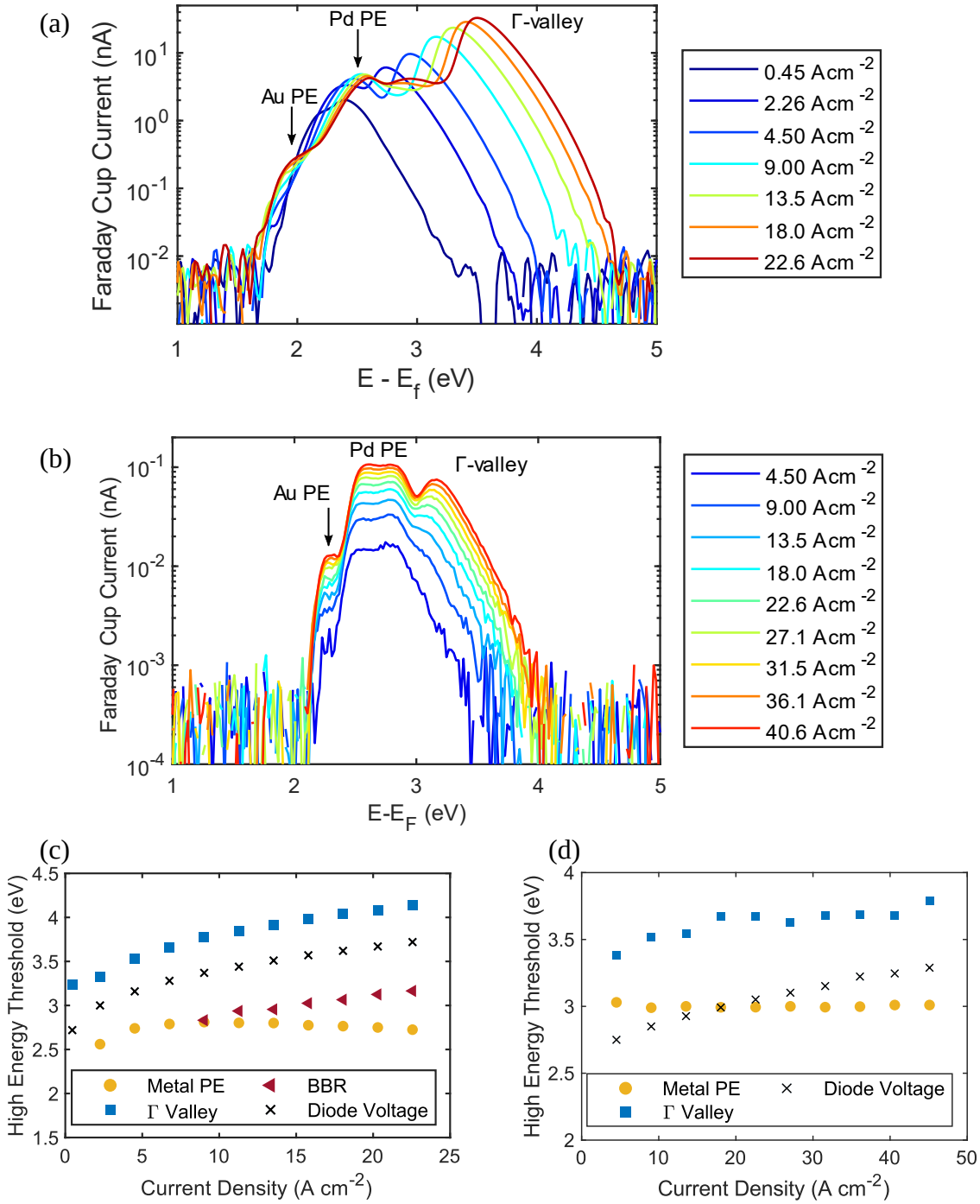

Figure 2.5: The EDCs of the Seoul VioSys LED and the Cree LED measured for different values of the injected current density are plotted in (a) and (b) respectively. By extracting the high energy thresholds and extrapolating to 0 mA the peaks are identified as shown in (c) and (d) respectively.

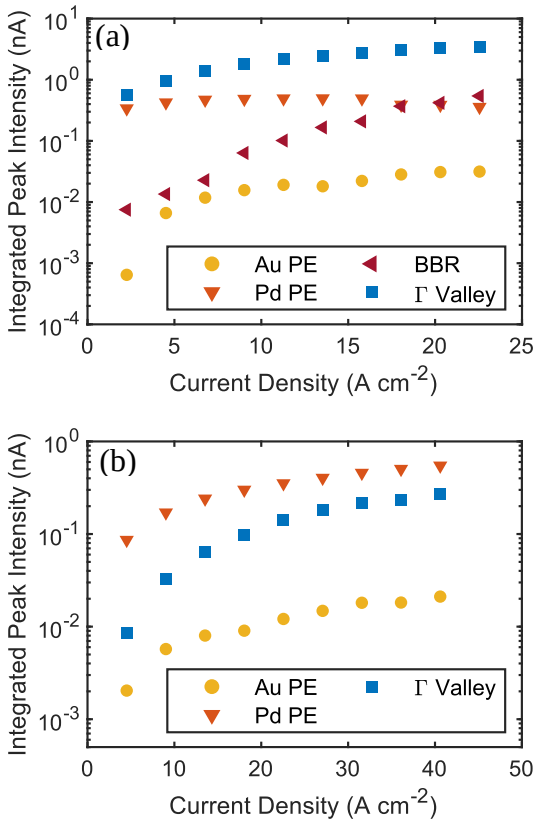

Figure 2.6. The integrated intensities of the different peaks appearing in the 2013 Seoul VioSys and 2016 Cree LED EDCs are plotted in (a) and (b) respectively as a function of injected current density. For all peaks, except Pd PE and BBR peaks of the 2013 Seoul VioSys , the integrated intensities increase with current density.

Analytic fits were attempted by superposing four exponentially modified Gaussians (EMGs) respectively to the pulse mode EDCs to differentiate peak contributions.[5] The dependence of the integrated intensities (given as a current) of the four peaks on the LED current density are shown in Figs. 2.6 (a) and (b). As one would expect, the integrated peak intensities of Au PE and Γ increases with increasing current density. For the 2016 Cree LED, the Pd PE peak intensity increases in a similar trend as its Au PE peak intensity. The Pd PE

peak intensity for 2013 Seoul VioSys appeared to increase initially but remained almost constant at higher current densities, a saturation that was observed in previous work.[3] This is possibly due to the convolution of the Pd PE and BBR peaks at low current densities, where part of the BBR peak intensity is fitted as Pd PE instead. In these LEDs, the p-region (110 nm and 250 nm) is sufficiently thick that the side valley electrons completely depopulate into the Γ valley within a diffusion length of the surface and escaped as Γ valley electrons. Since the detected side valley electron intensity for the 2019 Seoul VioSys with 60 nm p-region was only 5 to 20% of detected Γ valley electrons, it is possible for this ratio to drop to near zero while travelling another 40 to 190 nm.

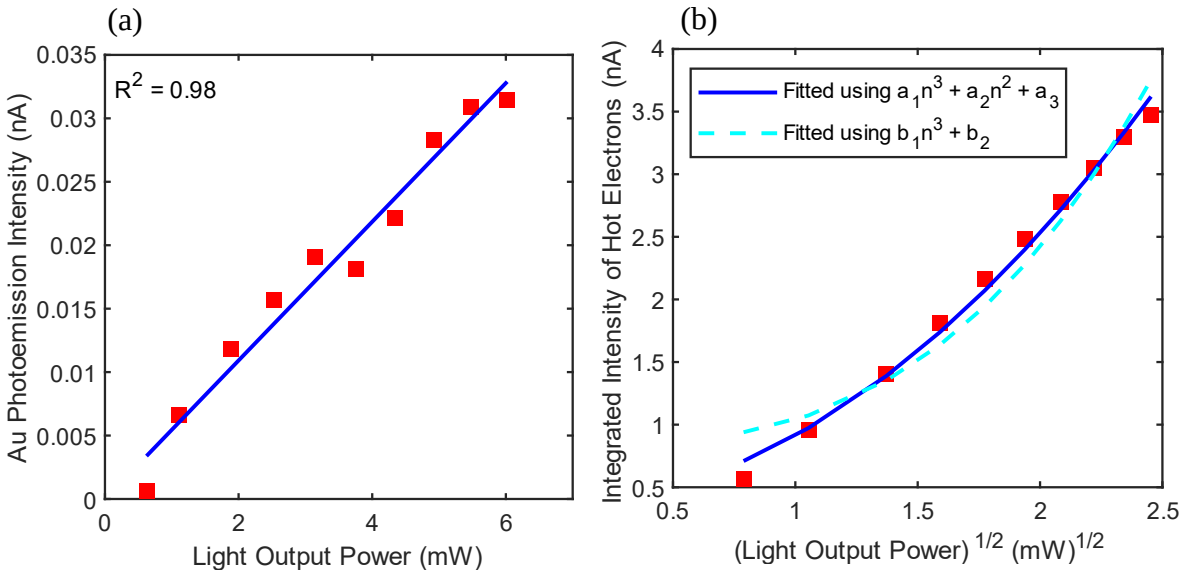

Figure 2.7: The LOP vs Au PE peak intensity is plotted in (a) to show their linear correlation for the 2013 Seoul VioSys LED. In this LED the hot (Γ) electron intensity cannot be described as having a purely cubic dependence on carrier density (square root of Au PE or LOP), requiring a quadratic dependence as showed in (b).

The Au PE intensities acts like an in-situ photometer, varying linearly with the LOP of the device, which was confirmed for the 2013 Seoul VioSys LED as shown in Fig. 2.7(a).[5] Here, hot electrons in the Γ valley do not vary as purely as the cube of carrier density, n^3, similar to the Γ valley electrons in the main manuscript. The same fit procedure was performed to include an n^2 term. The fit is clearly improved with the norm of the residuals decreasing from 39 to 7 and decreased *y*-intercept, as plotted in Fig. S4(b). While introducing a lower power term is expected to improve fits at lower current densities, the fit is improved even past the peak EQE in the droop regime. This n^2 dependence of hot electrons is attributed to trap-assisted Auger recombination (TAAR).[5,10,11]

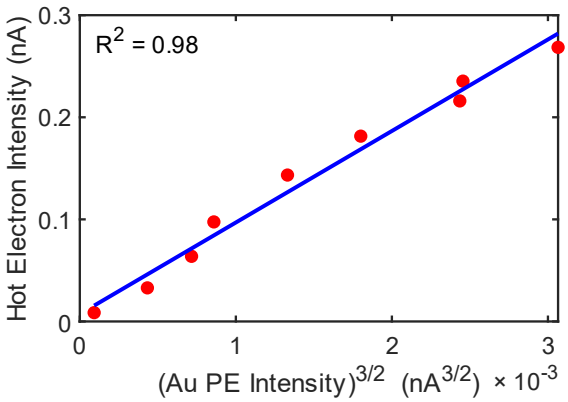

Figure 2.8: The cube of the square root of Au PE peak intensity is found to have a very good linear correlation to the hot electron intensity for the 2016 Cree LED.

For the 2016 Cree LED, as plotted in Fig. 2.8 a very good linear correlation between (Au PE)$^{3/2}$ and electron intensity were found. We attribute the lack of n^2 dependence for this LED to improved LED quality. TAAR was shown to be significant only for LEDs with peak IQEs much less than 100% while commercial LEDs have improved significantly over the years.[10,11]

For several III-Nitride LEDs from different era and suppliers we conclusively showed that hot electrons originate from either 3-body eeh Auger recombination and/or 2-body TAAR recombination. Following arguments in the main manuscript, this study further solidified the claim that droop is caused dominantly by Auger recombination.

B. Thermal droop experiments in blue LED

Armed with the improved quantitative analysis technique we turn our attention to reproducing thermal droop experiments carried out in reference.[5] We subject the device fabricated in the section IIA to increasing heating *in situ* to raise the sample temperature. The sample was resistively heated using a tantalum heating coil located on the backside of the sample. The temperatures were measured using a separate temperature calibration using an IR camera.[14] The energy distribution curves (EDCs) for pulsed diode current of 1 mA at 5% duty cycle are shown in Fig. 2.9 (a).

The peaks retain their identification from the previous section (IIA). The extrapolated high energy thresholds are plotted as a function of current density and temperature in Fig. 2.9 (b). The difference in energy between Γ-valley and SV1 measured over 42 sample points is 0.88 ± 0.07 eV. In Fig. 2.9 (b), the high energy threshold for the BBR PE peak at 147°C (red triangles) clearly tend towards the LED photon energy of 2.67 eV at low current densities, further reinforcing its origins as a photoexcited peak from the semiconductor.

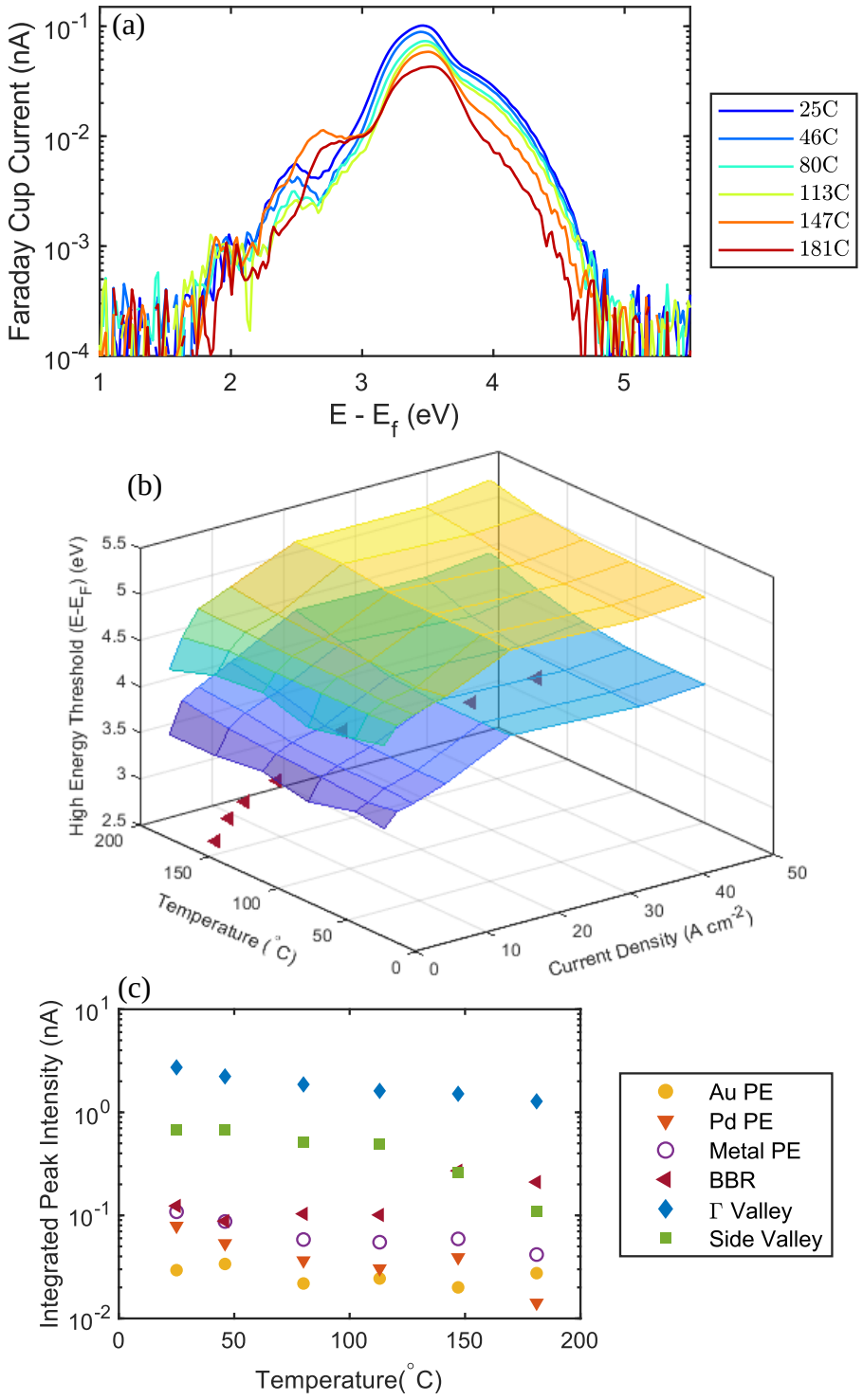

Figure 2.9: (a) The EDCs and (b) the integrated peak intensities for 5 mA, 5% duty cycle at various sample temperatures. (c) The extrapolated high energy thresholds for the semiconductor originating

peaks are shown as a function of temperature and current density. The red triangles correspond to the strong BBR PE peaks at 147˚C, and clearly tend towards photon energy at low current densities.

The general drop in intensity of Γ-valley and side-valley 1 (SV1) peaks with increasing temperature, at first glance, may be attributed to decesiation of the p-GaN. Extracting the low energy threshold of the Γ-valley peak shows that the vacuum level for the p-GaN is increasing with increasing temperature. The SV1 peak decreases sharply at 147˚C, coinciding with the sharp increase in the band-bending region (BBR) PE, but this trend is absent in other current densities hence does not constitute a true correlation. The Au photoemission (PE) peaks are unaffected by heating at the same current densities, while the Pd PE peaks decreased in intensity with increasing temperatures, as depicted in Fig. 2.9 (c). It was previously demonstrated that Pd decesiates with heating, while Au retains its cesiated state hence is a suitable *in situ* photometer.[5] The near constant Au PE peak indicate may be attributed to very small or unresolvable amounts of thermal droop in these samples, as the signal is very low in comparison to the background noise and the semiconductor peaks. An external light output power (LOP) dependence on temperature measurement is hence needed.

The sample was heated using a hot plate and its temperature was monitored using a type-K thermocouple in contact with the sample surface. The diode was biased under 5% duty cycle, such that the conditions are identical to the thermal droop measurements in EES. The LOP at different temperatures were measured using a calibrated photodiode positioned above the device. and are plotted in Fig. 2.10.

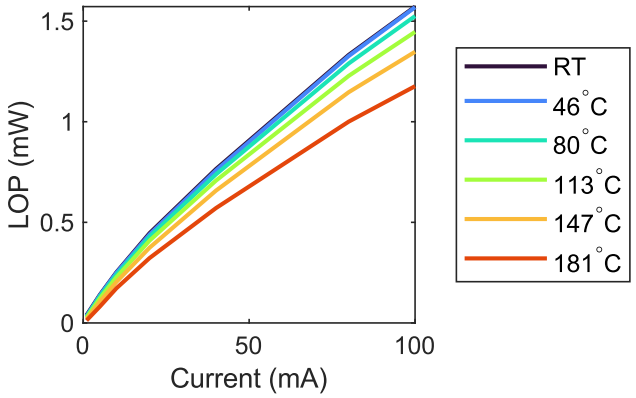

Figure 2.10: The light output power (LOP) of the EES device clearly demonstrates thermal droop, with a drop of 25% in LOP from room temperature to 181℃ at 100 mA diode current.

Unlike the Au PE peaks, the LOP of the EES device clearly demonstrates thermal droop, with a drop of 25% in LOP from room temperature (21℃) to 181℃ at 100 mA diode current. The LOP measured here is much smaller than the real LOP, as most of the emitted light is blocked by the large absorbing metal pads used in the EES device design.

Taking the square root of LOP once again we have a proxy for carrier density n, where $\sqrt{\text{LOP}} \propto n$. If a valley has predominant contributions from *ee* TAAR or *eeh* Auger generated electrons, its peak intensity will scale as n^2 or n^3, respectively.[5,10,15] If the valley has mixed contributions of both, we will expect its peak intensity to have a power dependence between 2 and 3, or $ln(\text{Peak Intensity}) \propto \alpha\, ln(n)$ for a slope α where $2 \leq \alpha \leq 3$. In the case of thermal droop, there is possibility that the dependence deviates from this range due to larger thermal escape rates. As such, the least-square fits will not be bounded.

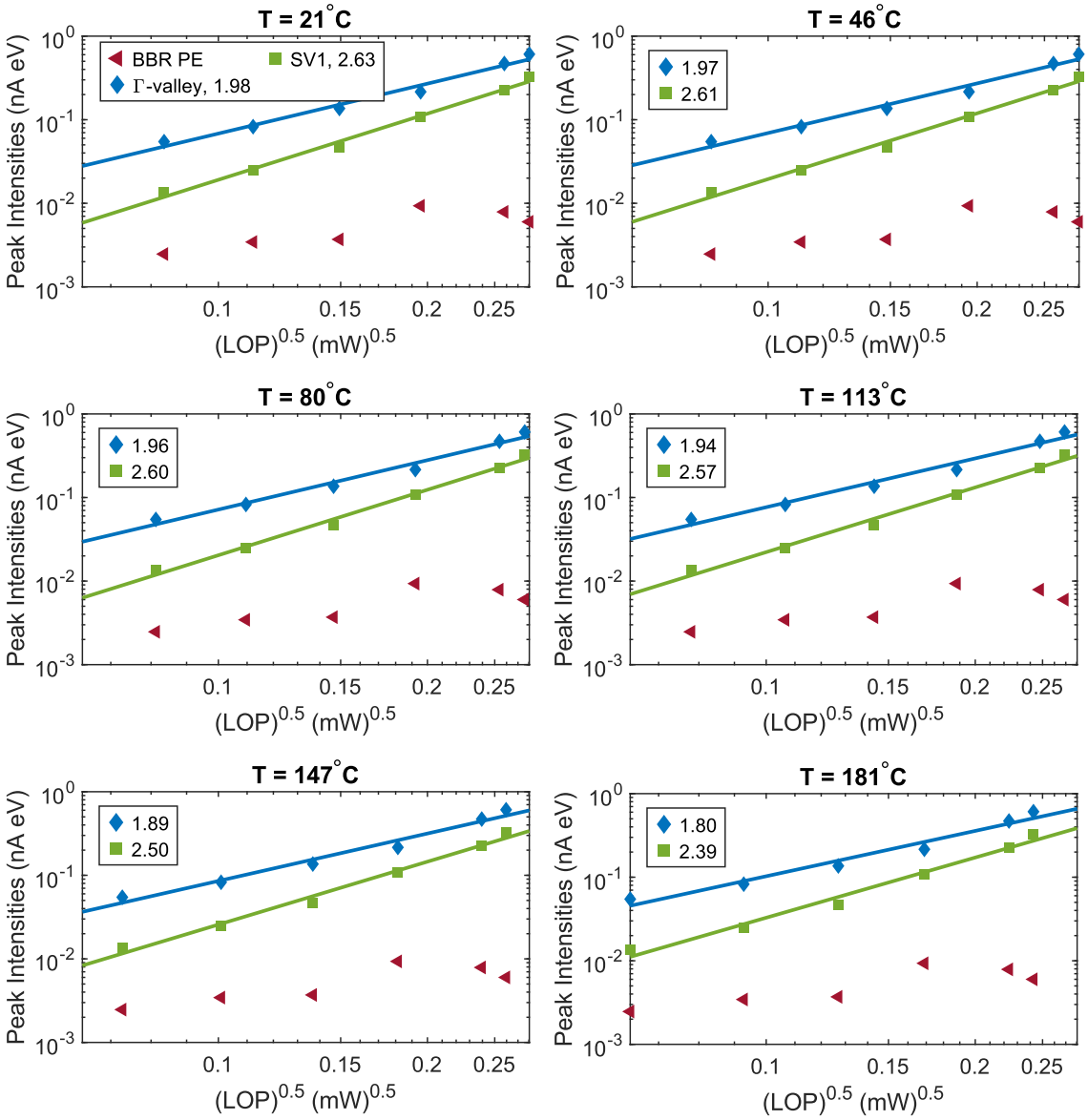

Figure 2.11: The fitted peak intensities of the emission peaks corresponding to the two semiconductor valleys are plotted as a function of $\sqrt{\text{LOP}}$, or n. The gradients of the fitted lines for both valleys are included in the insets of each graph, indicating their power law dependence on n.

The fitted peak intensities as a function of $\sqrt{\text{LOP}}$ is plotted in Figure 2.11. The thermal droop is implicitly indicated by the general left-shifting of the plotted data points from room temperature to 181°C. In general, we observed a decrease in the power dependence of the

peaks on n, decreasing from 1.98 to 1.80 for Γ-valley and from 2.63 to 2.39 for SV1. In the previous section, the SV1 peaks at room temperature was shown to have a strong cubic dependence. We attribute this difference to weighting of the fit to data of different magnitudes. In the previous section, the fit prioritizes fitting to the higher current density data due to its residual minimizing non-linear fit algorithm. The advantage of such fitting procedure is minimizing the effect of low signal-to-noise ratio on the fit at the expense of requiring more data points to be statistically significant. In this section, the logarithm of the data is taken, reducing the difference in magnitude between the high and low current density data, hence an equal weightage is applied to all the data. For this fitting procedure, a smaller number of data points is required, but the fit will be more susceptible to masking by background noise, skewing the gradients towards the lower numbers by placing a lower bound on the low intensity data. In either case, the power dependencies serve as a guide, for predominantly TAAR for a slope ~2, predominantly *eeh* Auger for a slope ~3, and mixed contributions for ~2.5. Hence, in the thermal series, we measure Γ-valley to have predominantly TAAR origins, SV1 to have predominantly *eeh* Auger origins at room temperature. It is possible that TAAR contributed to SV1 but was not accounted for in the previous section.

The change in fitted dependence of Γ-valley on n is small in comparison to the decrease in slope of SV1. The change in dependency from predominantly *eeh* Auger recombination tending towards predominantly TAAR points towards possible activation of traps by thermal energy. At the same time, we observe a sharper drop of SV1 intensity with increasing temperature compared to that Γ-valley. This implied that the decrease in overall valley peak intensities is not purely due to loss of signal due to decesiation, but indicative of a net decrease in n and hence hot electron currents J_{TAAR} and $J_{eeh\ Auger}$. If the carriers are lost to overflow

by thermal escape, we would expect corresponding increase in Γ-valley peak intensity, which should potentially be reflected in strong deviation from the standard slope numbers of $2 \leq \alpha \leq 3$. Since neither was observed, the carriers must be lost through other mechanisms. We hence turn our attention to a mechanism that does not generate hot electron and is thermally generated – Shockley-Read-Hall (SRH) recombination. The SRH coefficient is given by:

$$A_0 = \frac{np - n_i^2}{\tau_n\left(p + n_i e^{\frac{E_i - E_t}{k_B T}}\right) + \tau_p\left(n + n_i e^{-\frac{E_i - E_t}{k_B T}}\right)} \tag{2.1}$$

where τ_n and τ_p are the electron and hole lifetimes, respectively, E_t is the energy level of the trap of interest, n_i is the intrinsic carrier concentration and E_i is the intrinsic Fermi level.

It was calculated that SRH lifetime scales as $\tau_T \sim \tau_{300}(300/T)^{3/2}$, where with increasing temperature T in K the SRH coefficient and recombination rate increases.[16] For an increase in temperature from room temperature to 181℃, this corresponds to an estimated 51% decrease in SRH lifetime, or a two-fold increase in SRH rate. This may explain thermal droop in this LED. An increase in SRH rate correspond to an increase in active defects and hence TAAR. The combined effect will result in decrease of n and radiative recombination current at the same current density.

If A is indeed increasing with increasing temperature, by the ABC model the peak position should increase. In our experiment, the measured EQE is as shown in Fig. 2.12, which was calculated using the LOP showed above in Fig. 2.10. The very low values were due to the poor light extraction efficiency of the EES device design and poor collection efficiency of the measurement set-up.

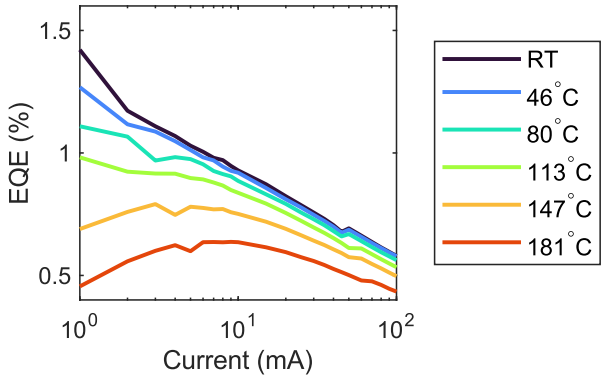

Figure 2.12: The external quantum efficiency curves measured. The peak position is observed to increase with increasing temperature.

The peak position for EQE is observed to increase with increasing current density. A similar peak position shift was observed in various other literature.[17–21] This is another strong indicator for the increase in A and by extension B' as cause of thermal droop in this sample.

In conclusion, we have performed EES on a c-plane blue LED with an electron blocking layer under different sample temperatures from 21℃ to 181℃. The peak position for EQE was observed to increase in parallel to decrease in detected electron current in EES, as well as increase in TAAR related currents. The results indicate thermal activation of traps involved in SRH and TAAR, which in turn leads to thermal droop.

References

[1] J. Iveland, L. Martinelli, J. Peretti, J.S. Speck, and C. Weisbuch, Phys. Rev. Lett. **110**, 177406 (2013).

[2] O.E. Tereshchenko, G.É. Shaibler, A.S. Yaroshevich, S.V. Shevelev, A.S. Terekhov, V.V. Lundin, E.E. Zavarin, and A.I. Besyul'kin, Phys. Solid State **46**, 1949 (2004).

[3] D.J. Myers, K. Gelžinytė, W.Y. Ho, J. Iveland, L. Martinelli, J. Peretti, C. Weisbuch, and J.S. Speck, Journal of Applied Physics **124**, 055703 (2018).

[4] M. Piccardo, L. Martinelli, J. Iveland, N. Young, S.P. DenBaars, S. Nakamura, J.S. Speck, C. Weisbuch, and J. Peretti, Phys. Rev. B **89**, 235124 (2014).

[5] D.J. Myers, K. Gelžinytė, A.I. Alhassan, L. Martinelli, J. Peretti, S. Nakamura, C. Weisbuch, and J.S. Speck, Phys. Rev. B **100**, 125303 (2019).

[6] J. Peretti, C. Weisbuch, J. Iveland, M. Piccardo, L. Martinelli, and J.S. Speck, in edited by K.P. Streubel, H. Jeon, L.-W. Tu, and M. Strassburg (San Francisco, California, United States, 2014), p. 90030Z.

[7] S. Wu, P. Geiser, J. Jun, J. Karpinski, D. Wang, and R. Sobolewski, Journal of Applied Physics **101**, 043701 (2007).

[8] S. Marcinkevičius, T.K. Uždavinys, H.M. Foronda, D.A. Cohen, C. Weisbuch, and J.S. Speck, Phys. Rev. B **94**, 235205 (2016).

[9] J. Iveland, M. Piccardo, L. Martinelli, J. Peretti, J.W. Choi, N. Young, S. Nakamura, J.S. Speck, and C. Weisbuch, Appl. Phys. Lett. **105**, 052103 (2014).

[10] D.J. Myers, A.C. Espenlaub, K. Gelzinyte, E.C. Young, L. Martinelli, J. Peretti, C. Weisbuch, and J.S. Speck, Appl. Phys. Lett. **116**, 091102 (2020).

[11] A.C. Espenlaub, D.J. Myers, E.C. Young, S. Marcinkevičius, C. Weisbuch, and J.S. Speck, Journal of Applied Physics **126**, 184502 (2019).

[12] V. Avrutin, S. din A. Hafiz, F. Zhang, Ü. Özgür, H. Morkoç, and A. Matulionis, Journal of Vacuum Science & Technology A: Vacuum, Surfaces, and Films **31**, 050809 (2013).

[13] C.-K. Li, M. Piccardo, L.-S. Lu, S. Mayboroda, L. Martinelli, J. Peretti, J.S. Speck, C. Weisbuch, M. Filoche, and Y.-R. Wu, Phys. Rev. B **95**, 144206 (2017).

[14] D.J. Myers, Electron Emission Spectroscopy of III-N Semiconductor Devices, University of California, Santa Barbara, 2019.

[15] W.Y. Ho, Y.C. Chow, D.J. Myers, F. Wu, J. Peretti, C. Weisbuch, and J.S. Speck, Appl. Phys. Lett. **119**, 051105 (2021).

[16] A. Schenk, Solid-State Electronics **35**, 1585 (1992).

[17] I.E. Titkov, S.Yu. Karpov, A. Yadav, V.L. Zerova, M. Zulonas, B. Galler, M. Strassburg, I. Pietzonka, H.-J. Lugauer, and E.U. Rafailov, IEEE J. Quantum Electron. **50**, 911 (2014).

[18] L. Zhao, D. Yan, Z. Zhang, B. Hua, G. Yang, Y. Cao, E.X. Zhang, X. Gu, and D.M. Fleetwood, IEEE Electron Device Lett. **39**, 528 (2018).

[19] A. Rashidi, M. Monavarian, A. Aragon, and D. Feezell, Sci Rep **9**, 19921 (2019).

[20] A. David, N.G. Young, C. Lund, and M.D. Craven, Appl. Phys. Lett. **115**, 223502 (2019).

[21] D.-P. Han, G.W. Lee, S. Min, D.-S. Shin, J.-I. Shim, M. Iwaya, T. Takeuchi, S. Kamiyama, and I. Akasaki, Sci Rep **10**, 17433 (2020).

III. Electron Emission Spectroscopy of Green LEDs

Building on past work in the blue regime, it is of interest to investigate efficiency droop mechanisms in green LEDs as part of the effort to understand the green gap. This chapter details EES measurements of several c-plane green LEDs grown on here at UCSB, as well as commercially sourced samples.

A. Detection of Higher Energy Side Valleys

The green LED presented in this section was grown using metal-organic chemical vapor deposition (MOCVD) and were activated in air at 600 ºC. The samples were grown on top of a patterned sapphire substrate and an unintentionally-doped (UID) GaN buffer layer. The subsequent material consisted of an *n*-type GaN:Si layer ([Si] $= 4 \times 10^{18}$ cm$^{-3)}$, 7 periods of *n*-type 5 nm $In_{0.04}Ga_{0.96}N$/ 3 nm GaN SL, a 2 period multiple quantum well (QW) with 3 nm InGaN QW/ 2 nm $Al_{0.05}Ga_{0.95}N$ cap layer/ 2.75 nm low temperature GaN barrier/ 4 nm high temperature GaN barrier, and 90 nm GaN:Mg ([Mg] = 5×10^{19} cm^{-3}) with a 11 nm p^{++} contact layer ([Mg] = 2.3×10^{20} cm^{-3}). The epitaxial structure of the LED is shown below in Fig. 1.

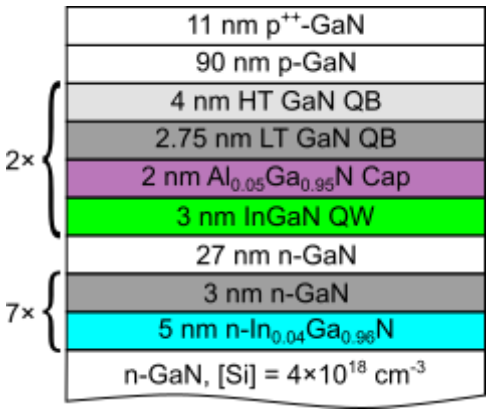

Figure 3.1: Schematic of the epi layer stack for the LEDs discussed in this work, grown by MOCVD (not to scale).

The sample was fabricated to form devices described in Ref. 1 and in Appendix B.[1] The devices were cleaned using acidic piranha and HCl prior to introduction into the EES system. EES was performed with the device biased under CW mode, with currents ranging from 1 mA to 90 mA for corresponding current density range of 0.45 to 40.7 A cm^{-2}. The high energy thresholds (HETs) of the peaks were extrapolated numerically by obtaining the zero-intercept of the high energy positive slope of the energy derivative curves.[2–4] These HETs are then compared to the diode bias voltage to distinguish metal photoemission (PE) peaks and semiconductor peaks, as well as obtaining the bulk valley minimum values for valley identification.

At low current densities, 3 peaks were observed as shown in Fig. 3.2 (a) – the first peak has a high energy cut off near the emission wavelength around 2.4 eV, the second is a broad peak in the range of 3 to 4.3 eV, and there is a very high energy peak with a cut off energy around 5.5 eV at 1 mA. The second peak appears with a high energy shoulder at low current densities, and with a low energy shoulder at higher current densities.

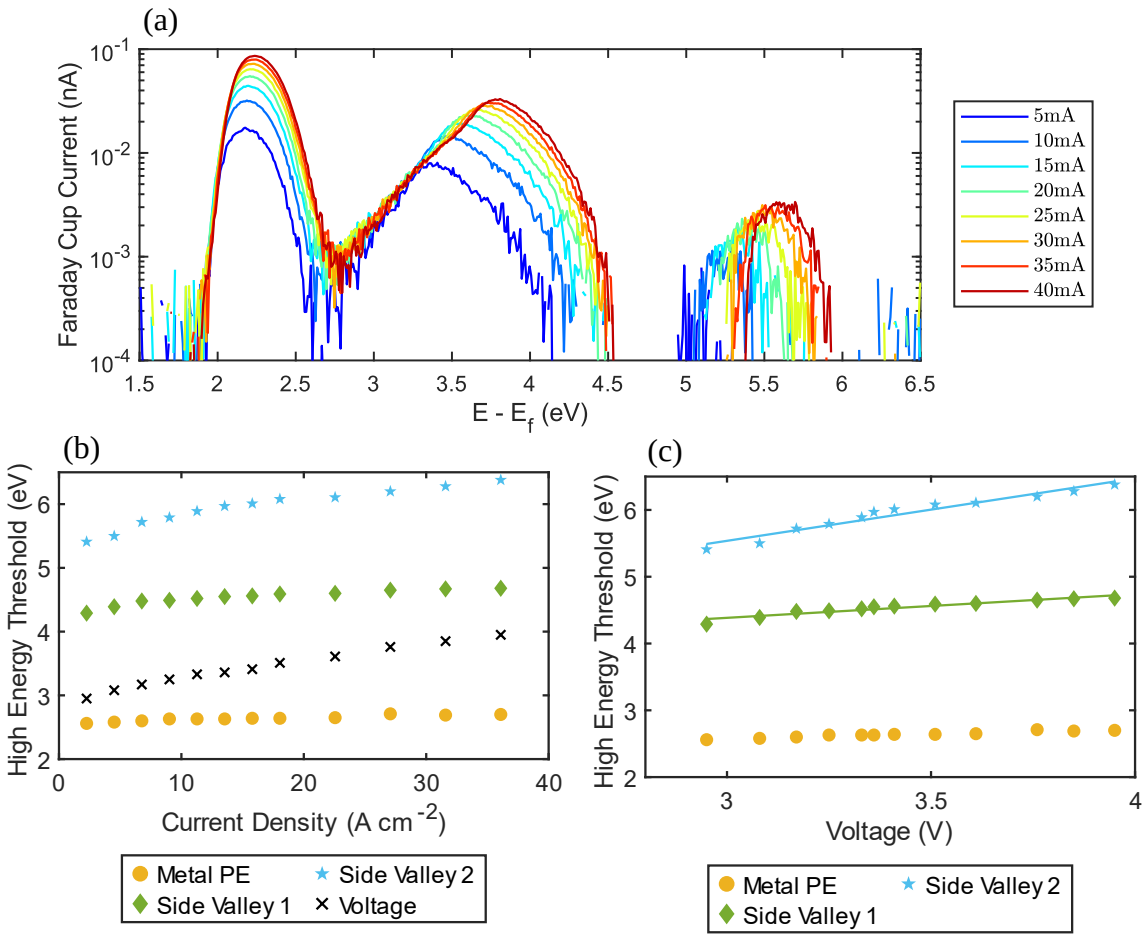

Figure 3.2: (a) Energy distribution curves plotted for multiple diode currents. (b) The high energy thresholds of the resolved features as a function of diode current and diode voltage.

Comparing to published blue LED emission spectra, we deduce that the first peak is due to metal photoemission excited by LED emitted light.[1,5] Unlike previous data, even though a Pd/Au metal stack is used as the p-contact, only one peak is observed. This peak decreases in magnitude with increasing temperature – so we conclude it must be due to photoemission from Pd.[1,5] As of now we have no explanation to the missing Au peak, requiring more repeats of this measurement.

The low energy cut-off at ~2.7 eV for the second broad peak corresponds to the vacuum level of the *p*-GaN with respect to the Fermi level and is observed to remain constant for all diode current, indicating no decesiation over the course of measurements.

Given the HET data as depicted in Figs. 3.2 (b) and (c), we conclude that the broad peak is a convolution of BBR PE, Γ-valley and first side valley (SV1). One can resolve two distinct features in the differential EDC (DEDC), corresponding to Γ-valley at ~3.4 eV and SV1 and ~4.3 eV. A low energy shoulder is resolved at higher diode currents, which was previously observed.[6,7]

The very high energy peak with high cut-off at ~5.7 eV was not seen in any previous blue InGaN/GaN LEDs without EBL.[5] This peak is observed for 5 mA and all higher currents, and the signal, if present, is too low to resolve for less than 5 mA. The cut-off is observed to shift over 1.1 eV to 6.5 eV as the current changes from 10 mA to 90 mA. This change is much larger than the SV1 walk out of 0.4 eV (from 4.3 to 4.7) or the photoemission blue shift. This peak is located at an average of 2 eV above Γ-valley. There are several possibilities for the origin of this peak. We must verify that this is not excitation of Γ-valley electrons at the p-GaN surface by photoemission. The fact that the spectral shift exceeds that of SV1 implies this possibility. However, combining spectral shift effect from both voltage drops over the contacts (0.4 eV) and photoemission shift from wavelength blueshift (0.2 eV) does not sum up to the same amount of spectral shift. A photomodulated EES experiment is required for full verification.

Another concern was excitation of electrons from the analyzer. To maximize signal intensity and to reduce Franz-Keldysh effect, the testing devices are placed very close to the analyzer entry slit. It is possible that the desorbed Cesium from samples over many

measurements may be adsorbed onto the walls of the analyzer. If this is true, we should observe an increase in the intensity of this very high energy peak over measurements, especially over thermal droop experiments, which was not the case. The spectra for 1 to 90 mA were repeated and taken in randomized order over time, showing that the signal intensity and spectral shift is only dependent of the current.

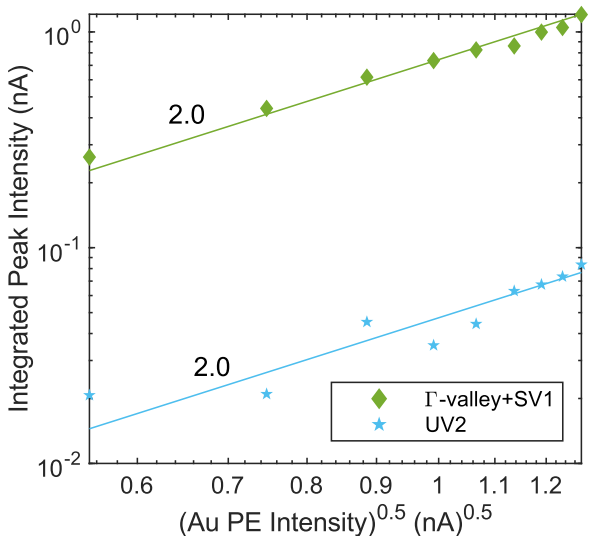

Figure 3.3: The integrated peak intensities of the various semiconductor peaks are shown to have n^2 dependence, indicating their origins as predominantly trap-assisted Auger recombination.

The valley intensities were obtained by fitting superposed exponentially modified Gaussians to each peak. Utilizing power law fitting with $\sqrt{\text{LOP}} \propto n$, we determined that Γ - SV1 combined peak has a strong n^2 dependence as shown in Fig. 3.3, indicating that it was generated predominantly by trap-assisted Auger recombination (TAAR). The unidentified peak was demonstrated to have n^2 dependence as well. In the same line of argument as with the SV1 signal, it is possible that this signal arises from electrons excited to a higher energy via Auger recombination in the active region (2.36eV for 524nm emission wavelength). The location of this peak agrees with theoretical prediction of wurtzite GaN for L-M, A, or Γ3-

valley calculated using empirical pseudopotential method (EPM).[8,9] By conservation of momentum, this peak cannot be the A-valley. At higher currents, the higher energy threshold is observed to walk out to 2.9 eV above Γ-valley, requiring energies not available in the quantum wells. If this signal is not a measurement artefact, then there must be a deep trap at the InGaN well - AlGaN barrier interface in the active region participating in a trap-assisted Auger recombination process.

B. Effect of including pre-well InGaN/GaN superlattices in green LEDs

The following section is mostly reproduced from W. Y. Ho, A. I. Alhassan, C. Lynsky, Y. C. Chow, D. J. Myers, S. P. DenBaars, S. Nakamura, J. Peretti, C. Weisbuch, and J. S. Speck, "Detection of hot electrons originating from side valley at ~1.7 eV above the Γ-valley in wurtzite GaN using electron emission spectroscopy (EES)," *submitted*. The main article has been combined with the supplementary material for clarity.

While advances in light-emitting diodes (LEDs) have allowed their widespread use and application in the lighting industry, the technology still faces a major limitation posed by the "green gap" where the internal quantum efficiency (IQE) of LEDs decrease with increasing wavelength. The origins of the "green gap" are still under debate, with the increase in electron-hole separation decreasing radiative rates, while decreasing growth temperatures for the InGaN quantum wells may result in a high density of nonradiative recombination centers.[10–13]

At the same time, it is known that addition of an InGaN/GaN pre-well superlattice (SL) will improve the performance of green LEDs, though the reason for such improvement also

remains an open question. These superlattices introduce V-defects that have been proposed improve hole injection through the V-defect sidewall.[14–16] The inclusion of SLs are also proposed to reduce Auger recombination;[17,18] or reduce defects and/or dislocations.[14,19] In most of these studies the authors correlate the pre-well SL with defect density and photo- or electroluminescence intensities, which ultimately are only indirect measurements of the recombination processes. Electron Emission Spectroscopy (EES) of electrons emitted in vacuum enables direct measurement of hot electrons that are generated from Auger recombination processes including band-to-band Auger (electron-electron-hole, *eeh*) and trap-assisted Auger recombination (TAAR) (electron-electron, *ee*).[5,7,20,21] In this work we observe hot electrons in EES spectra that accumulate in a high energy GaN conduction band valley for LEDs without a pre-well SL and the suppression of these hot electrons with the inclusion of a pre-well SL.[5,7,20,21]

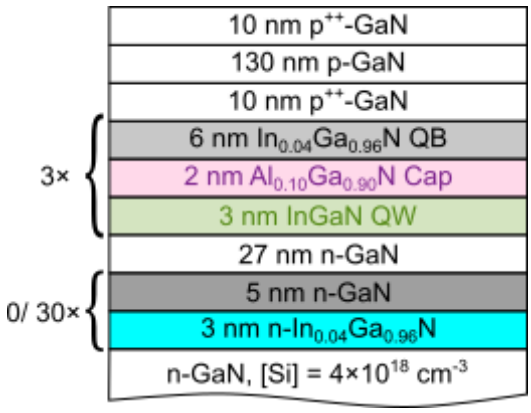

Figure 3.4: Schematic of the epi layer stack for the LEDs discussed in this work, grown by MOCVD (not to scale). The LEDs have different pre-well SL periods of 0 or 30 corresponding to total pre-well InGaN thicknesses of 0 and 90 nm respectively.

The green LEDs presented in this work were grown using metal-organic chemical vapor deposition (MOCVD) and were activated at 600 ºC. The samples were grown on top of a

patterned sapphire substrate and an unintentionally-doped (UID) GaN buffer layer. The subsequent material consisted of an *n*-type GaN:Si layer ([Si] = 4×10^{18} $cm^{-3)}$, 0 or 30 periods of *n*-type 5 nm $In_{0.04}Ga_{0.96}N$/3 nm GaN SL, a 3 period multiple quantum well (QW) with 3 nm InGaN QW/2 nm $Al_{0.10}Ga_{0.90}N$ cap layer/ 6 nm $In_{0.04}Ga_{0.96}N$ barriers), and 150 nm GaN:Mg ([Mg] = 5×10^{19} cm^{-3}) with a p^{++} contact layer ([Mg] = 2.5×10^{20} cm^{-3}). The epitaxial structures of the LEDs (henceforth referred as 0SL and 30SL corresponding to their SL periods) are shown in Fig. 3.4. The use of AlGaN cap layers had been shown to improve efficiency in longer wavelength LEDs by preventing desorption of the indium in QW during growth of the higher temperature barriers.[22]

The epitaxial materials were processed in parallel into devices suited for EES measurements.[1] The p-contact was 30 nm Pd/ 300 nm Au deposited in a honeycomb pattern, forming a single EES device of area 0.22 mm^2 with 0.096 mm^2 exposed p-GaN comprised of an array of hexagons with an apothem of 3.5 μm separated by 3 μm wide metal strips.[1] Each of the samples were cleaned and introduced into an ultra-high-vacuum (UHV) EES system as described in Ref. 11. For each sample a submonolayer of Cs was deposited (cesiation) using a SAES cesium source. By monitoring photoexcited electrons emitted from *p*-GaN during Cs deposition, we confirmed that negative electron affinity (NEA) was achieved.[20] EES was performed with the devices biased under CW mode for injection currents ranging from 1 mA to 50 mA corresponding to current densities *J* ranging from 0.45 A cm^{-2} to 22.5 A cm^{-2} - these current densities were chosen to be low to avoid self-heating without sacrificing signal-to-noise ratio. The energy of the emitted electrons was measured referenced to the Fermi level of the *p* contact using a Comstock AC-901 spherical sector electrostatic analyzer operated in constant pass energy mode with an energy resolution of 40 meV.[6] With increasing diode

current, there was an increased ohmic voltage drop across the metal-semiconductor interface. This increased voltage drop shifted the measured energy of electrons emitted from the semiconductor surface to higher values but did not affect the Pd and Au photoemission peaks which are a result of diode light.[1,6] This voltage shift was employed to distinguish electrons originating from the semiconductor and to extract bulk valley minimum values at extrapolated zero bias.

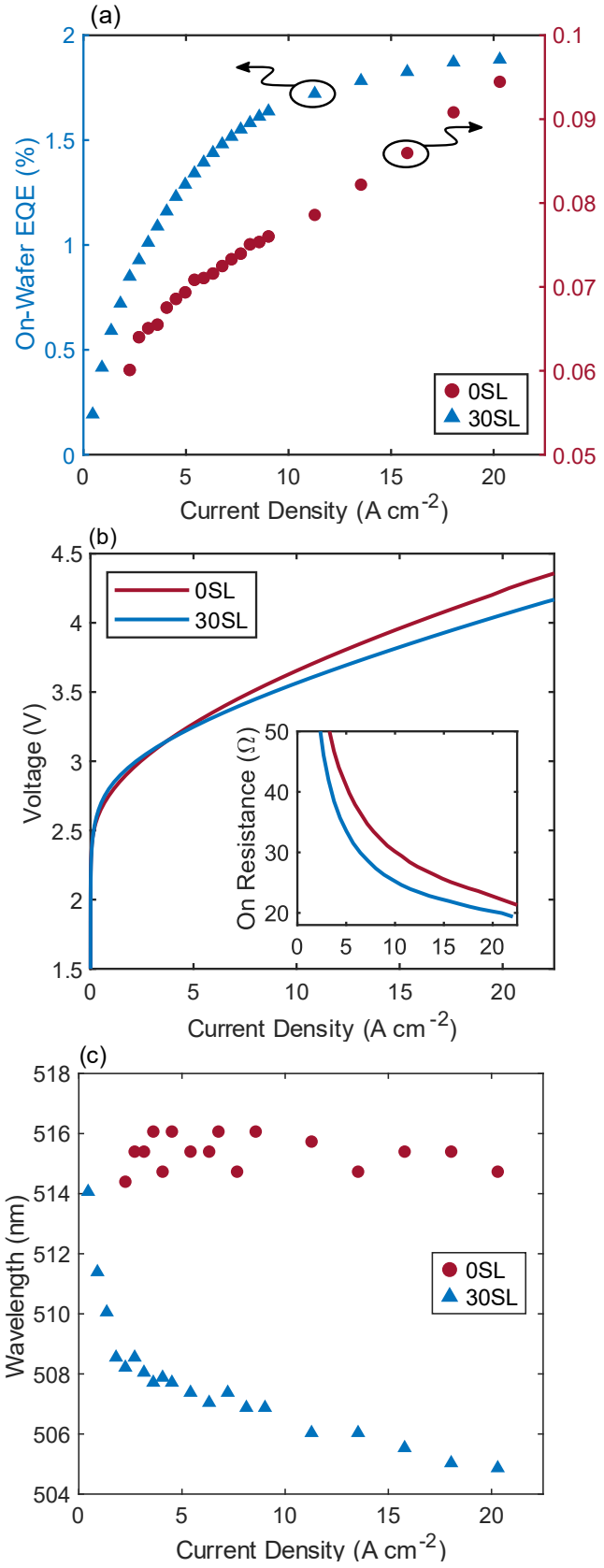
(a)
On-Wafer EQE (%)
Current Density (A cm-2)
0SL
30SL
(b)
Voltage (V)
On Resistance (Ω)
Current Density (A cm-2)
0SL
30SL
(c)
Wavelength (nm)
Current Density (A cm-2)
0SL
30SL

Figure 3.5: (a) Measured EQE of 0SL and 30SL devices as a function of current density. The EQE is shown to increase significantly with inclusion of pre-well SL. (b) Dependence of diode voltage and the on-resistances (inset) on current density. The inclusion of pre-well SL in the epitaxial structure reduced the operating voltages and on resistance. (c) Peak wavelength of 0SL and 30SL device as a function of current density.

The corresponding $J-V$, external quantum efficiency (EQE) and wavelength curves of the EES devices for the series were measured on die with a photodetector. The results are shown in Fig. 3.5 (a) – (c), with the on-resistances plotted as inset in Fig. 3.5 (b). The light output power (LOP) and hence the EQE markedly increased from 0SL to 30SL. The operating voltages improved as well. Circular transmission line measurements (CTLMs) demonstrated ohmic contact behavior to *p*-GaN for both samples, with similar specific contact resistivities in the low 10^{-3} Ω cm^{-2} range. Hence the $J-V$ trends are not a result of contact resistances and originates from the semiconductor diode. This improvement in resistance may be attributed to reduced injection barriers at the sidewalls of V-defects, which are more numerous in the sample with pre-well SL.[23,24] Hence with addition of a pre-well SL the on resistance decreased. The current density at which the quantum efficiencies of these samples reached maximum, J^*, is lower for the sample with a pre-well SL, where $J^* \sim 22.5$ A cm^{-2} for 30SL and at $J^* > 450$ A cm^{-2} for 0SL. The current densities of the LEDs are given by:

$$J = J_{\mathrm{SRH}} + J_{\mathrm{rad}} + J_{\mathrm{TAAR}} + J_{eeh\,\mathrm{Auger}} + J_{\mathrm{overflow}}$$

$$= q d_{\mathrm{QW}}(An + Bn^2 + B'n^2 + Cn^3) + J_{\mathrm{overflow}}$$

where q is the elemental charge and d_{QW} is the thickness of the active region. $J_{\mathrm{SRH}}, J_{\mathrm{rad}}, J_{\mathrm{TAAR}}$, and $J_{eeh\,\mathrm{Auger}}$ are Shockley-Read-Hall (SRH) recombination, radiative recombination, TAAR

and *eeh* Auger recombination currents with recombination coefficients A, B, B', and C, respectively. J_{overflow} correspond to overflow currents. Since the corresponding carrier density for peak EQE, $n^* = \sqrt{A/C}$, the high numbers for J^* is indicative of the high SRH rates in these samples.[25] This can be attributed to the use of InGaN barriers, which are grown at lower temperatures than traditional GaN barriers. The overall reduction in J^* with inclusion of a pre-well SL indicates a reduction of SRH defects. The 30SL sample wavelength blue-shifted as expected when J increased due the free-carrier screening of internal electric field.[26] Reduced wavelength shift is observed for the 0SL sample. The high non-radiative recombination rate leads to lower carrier density, thus delaying the onset of free carrier screening of the polarization-related charges at the QW/quantum barrier interfaces.

Let us focus on the energy distribution curves (EDCs) from EES under different currents of the 0SL sample shown in Fig. 3.6 (a) upper panel. Five peaks were observed in the energy distribution curves (EDCs) of the LED without pre-well SL (0SL), while five corresponding features are resolved in the negative parts of the derivative of the EDCs (DEDCs). The high energy thresholds of these peaks were obtained by taking the extrapolation to zero of the high energy slopes, as depicted in Fig. 3.7.[2–4]

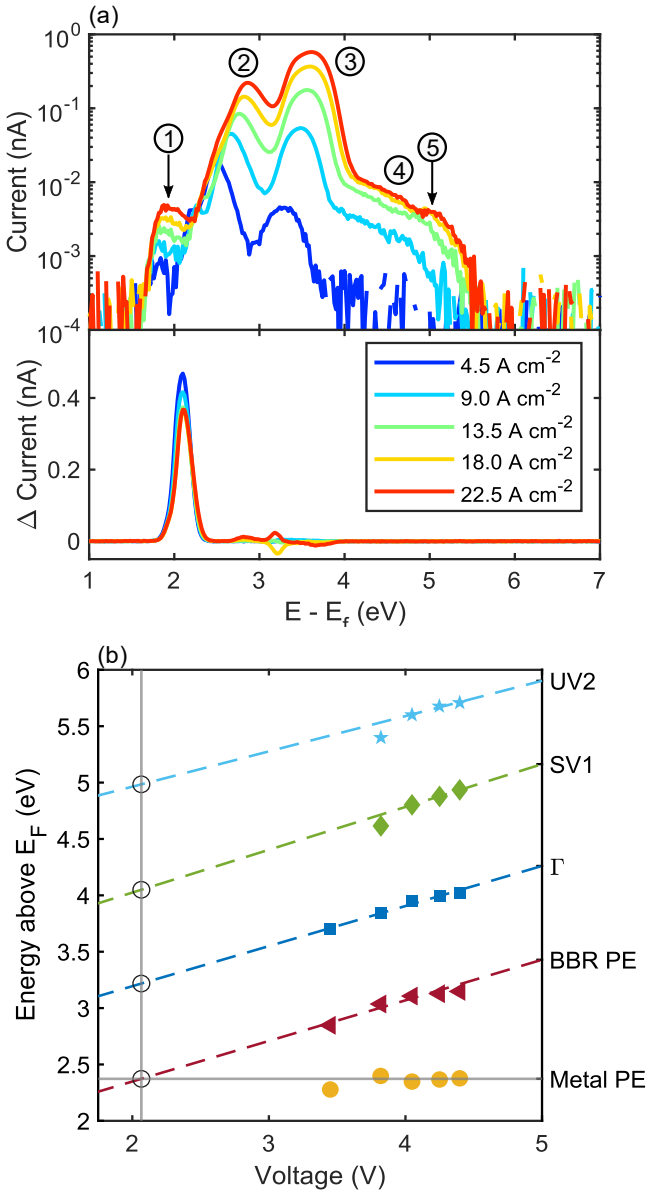

Figure 3.6: (a) Upper panel: measured electroemission energy distribution curves (EDCs, in terms of Faraday cup current) as shown in (a) for the 0SL sample at different current densities displaying 5 distinct peaks. Lower panel: differential photoemission EDCs measured when an external 532 nm laser was incident on the sample during LED operation (current injection), showing no significant change for peaks of semiconductor origin and only an increase in Au PE intensity. By extrapolating to the expected 0 mA position as shown in (b), the peaks are assigned to be arising from ① Au photoemission,

② photoexcitation from the BBR, ③ Γ-valley, ④ first side valley at ~0.9 *eV* above Γ, and ⑤ a higher energy peak of semiconductor origin at ~1.7 *eV* above Γ.

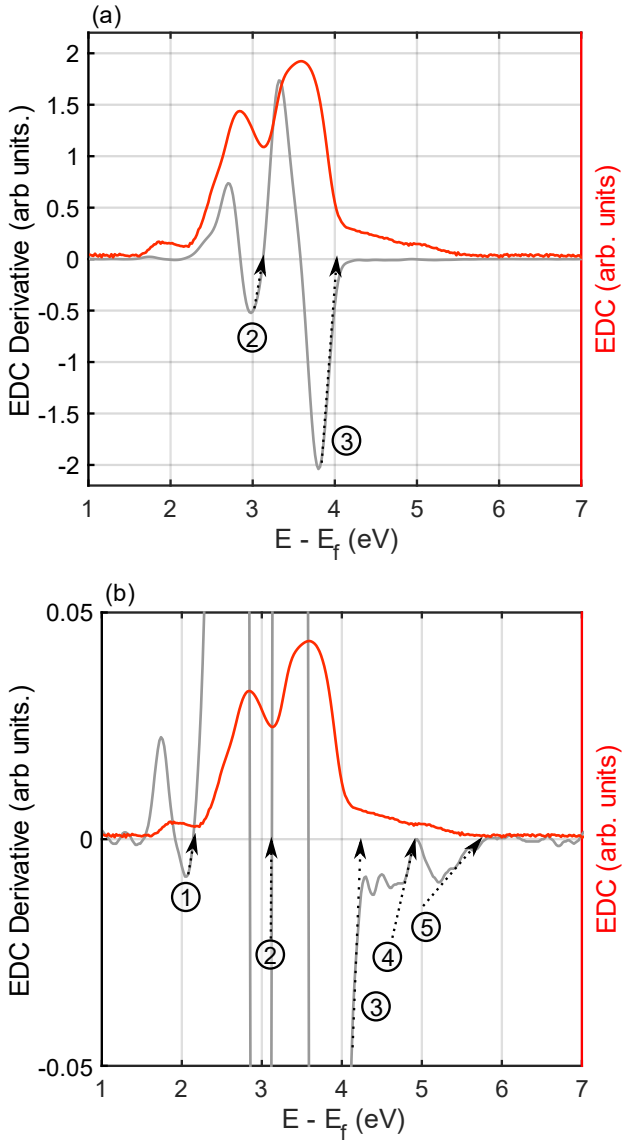

Figure 3.7: The derivative of the energy distribution curve (DEDC) overlaid with the corresponding EDC for 22.5 A cm^{-2} is plotted for the 0SL sample in full in (a) and magnified in (b). The EDC is smoothed using low pass Fourier filtering for clarity. The high energy thresholds for the 5 resolved features are marked by arrows labelled ① to ⑤. The extrapolation is repeated for all measured EDCs.

The first peak ① remains constant in energy with increasing diode current and exhibits a linear correlation with LOP, which is characteristic of photoemission (PE) from Au of the p-contacts due to LED light.[1] A low energy peak ② below the Γ-valley is identified as due to electrons originating from the band-bending region (BBR).[3,7] For peaks ③, ④, and ⑤ , the extracted high energy thresholds extrapolate to expected bulk valley minima at 0 mA of 3.22, 4.05 and 4.98 eV above Fermi level respectively as shown in Fig. 3.6 (b)[6,20]. These values imply that peak ③ is comprised of electrons originating from the Γ-valley while peak ④ originates from the first side valley (SV).[1,3,5–7,20,21,27,28] The position of peak ⑤ increases with increasing the diode voltage and hence must originate from the semiconductor.[7,20] In the same line of reasoning with electrons in the first SV it is not possible to have electrons excited ~1.7 eV above the conduction band minimum by electric fields in the band bending region due to conservation of energy.[29] Electrons that escaped the active region due to overflow from the active region will only end up in the Γ-valley.[29]

If peak ⑤ is due to a photoexcitation process, then by supplying additional photons on top of the LED light emission should increase the intensity of peak ⑤. We compared the measured 0SL EDCs with and without an external significantly brighter (than 0SL) 4.8 mW green laser of wavelength 532 nm (2.33 eV) incident on the sample. A shown in Fig. 3.6 (a) lower panel that while metal photoemission increased by orders of magnitude, there is negligible change in the semiconductor peaks. Thus, we conclude that peak ⑤ originates from the semiconductor through electrical injection. As such, there are 5 total contributions observed – from metal

photoemission, excitation from the BBR, Γ-valley, first side valley (SV1), and an unidentified peak of semiconductor origin which henceforth is referred to upper valley (UV2).

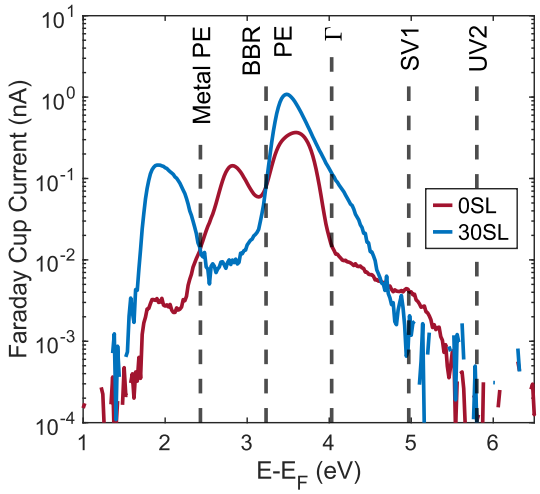

Figure 3.8: The EDCs measured at 22.5 *A cm*$^{-2}$ are plotted with intensities scaled such that the Au PE peak intensity scales with LOP across samples. The peak identification lines (vertical dashed lines) are only a guide (see Fig. 3c and the supplementary material for the analysis of the peak position).

A comparison of the EDCs for both samples at 22.5 A cm^{-2} is plotted in Fig. 3.8. For the 30SL sample, three peaks were present with the peaks identified as Au PE, Γ-valley and SV1. As with the case for 0SL, a low energy peak below the Γ-valley peak is present for 30SL which is attributed to the BBR.[3,7] Similar to previous reported EES measurements on various blue LEDs of different epitaxial structures, year of growth, and sources,[1,3,5,7,20,21,29] UV2 was not observed for 30SL.

The intensities of the various peaks were obtained by fitting superposed exponentially modified Gaussians to the EDCs using standard non-linear least squares method using

OriginPro (see Fig. 3.9 for the fit of the 0SL EDC at 22.5 A cm^{-2}).[5] The equation for a single peak is given by:

$$f(x) = \frac{A}{\tau} e^{\frac{1}{2}\left(\frac{w}{\tau}\right)^2 - \frac{x-x_c}{\tau}} \int_{-\infty}^{z} \frac{1}{\sqrt{2\pi}} e^{-\frac{y^2}{2}} dy,$$

$$z = \frac{x - x_c}{w} - \frac{w}{\tau}$$

where A, x_c, w is the area, center, width of the peak, respectively, and τ is the exponent relaxation parameter.[5,7,21] The metal photoemission peak is fitted such that it agrees with expected shapes arising from the density of states of the metal.[1]

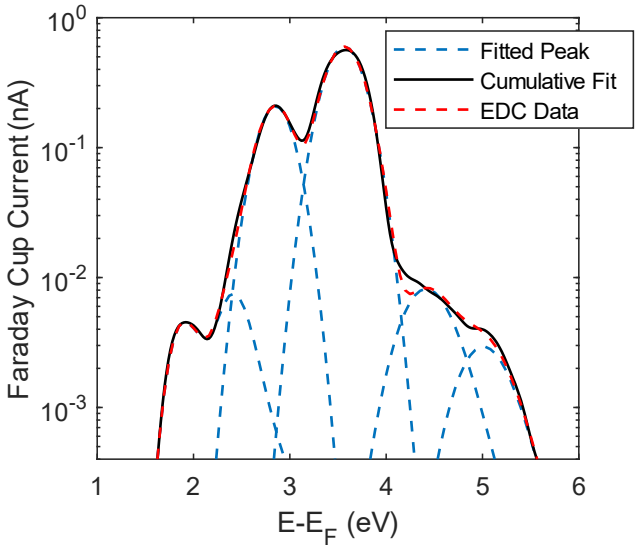

Figure 3.9: The peak intensities of the different valleys are obtained by non-linear square fits of superposed exponentially modified Gaussians, as shown for 0SL at 22.5 A cm^{-2}.

The internal quantum efficiency (IQE) and current – voltage ($J - V$) characteristics of these two LEDs were simulated using a 1D Poisson-drift-diffusion solver based on the Localization Landscape Theory.[30–32] The simulated structures for 0SL and 30SL are mostly identical, with the non-radiative lifetimes of 1×10^{-9} s and 2×10^{-8} s, respectively, chosen

such that the simulated IQE curves have matching J^* values with the experimental EQE. The overflow current is then given by the simulated electron current in the *p*-region. The simulated band profile and electron current at 22.5 A cm^{-2} are plotted in Fig. 3.10 (a) – (b), while the overflow currents as a function of current density is plotted in Fig. 3.10 (c). The overall overflow current was simulated to be low even in the absence of an electron blocking layer. At all current densities investigated, the overflow current density is larger for 30SL sample. This may be due to the smaller Shockley-Read-Hall (SRH) recombination rates for 30SL and hence larger electron density in the active regions. Since the overflow current densities are low at less than 0.2% injected current for both samples at all investigated current densities, and hence will not contribute significantly to the Γ-valley peak intensities.[30–32] The possible origins of the electrons detected from the semiconductor valleys are hence *ee* TAAR or *eeh* Auger recombination.[3,5,7,20,21,25,29] In *ee* TAAR an electron is captured by a trap and the released energy excites another electron into higher valleys. Using the square root of Au PE peak intensity as a proxy for carrier density n in the active region a quantitative investigation of the peaks dependence on n can be performed.[5,7] Since the two samples have nominally identical active region structure, we can use the same radiative recombination coefficients B for both 0SL and 30SL such that $\sqrt{\text{Au PE Intensity}} \propto n$. If the valley has predominant contributions from *ee* TAAR or *eeh* Auger generated electrons, its peak intensity will scale as n^2 or n^3, respectively.[5,7,21] If the valley has mixed contributions of both, we will expect its peak intensity to have a power dependence between 2 and 3, or $ln(\text{Peak Intensity}) \propto \alpha\ ln(n)$ for a slope α where $2 \leq \alpha \leq 3$.

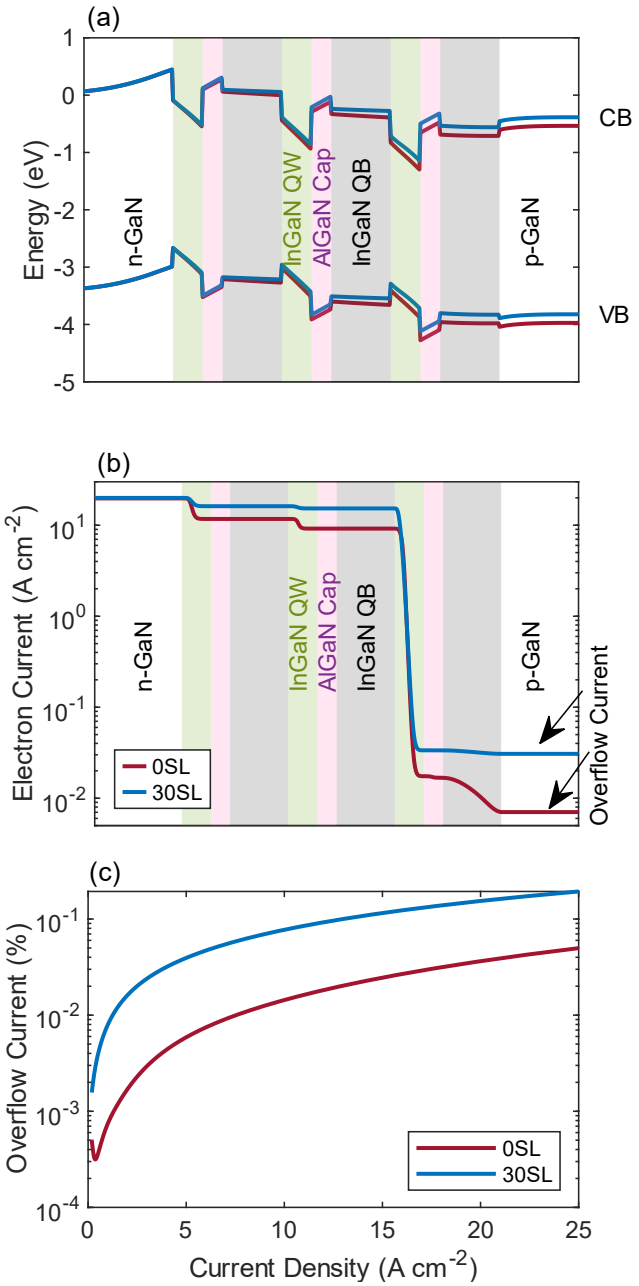

Figure 3.10: The simulated band profile and electron current at 20 A cm^{-2} diode current density are plotted in (a) and (b), respectively. The percentage overflow electron current at is plotted as a function of current density in (c).

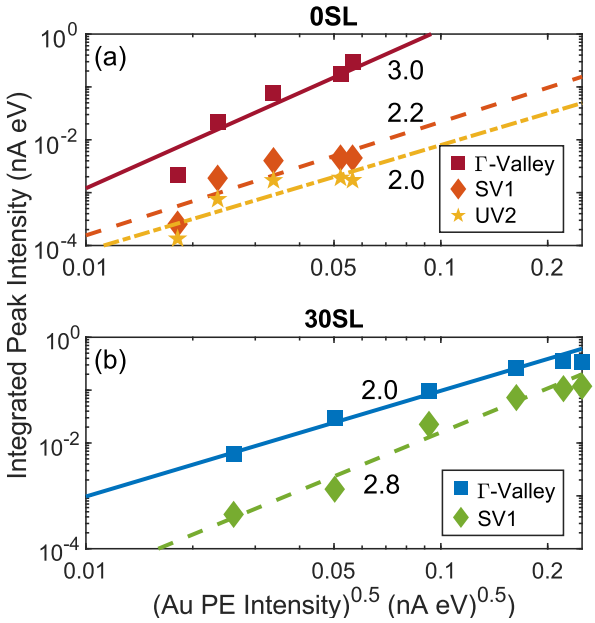

Figure 3.11: Using the square root of Au PE integrated intensity as a proxy for carrier density, n,[15,18] the peak intensities dependence of Γ-valley, SV1 and UV2 on $\sqrt{Bn^2}$ for 0SL and 30SL are plotted in (a) and (b), respectively. The slope of each line from bounded linear least square fits of the data are included. The slope of log-log plots gives the power dependence on n and hence indicate its origins. A slope of 2 corresponds to *ee* TAAR while a slope of 3 corresponds to *eeh* Auger recombination.

From the bounded least square fits as shown in Fig. 3.11, it was deduced that for 0SL Γ-valley, SV1 and UV2 have *eeh* Auger, mixed *eeh* Auger + *ee* TAAR, and *ee* TAAR contributions, respectively; while for 30SL, Γ-valley and SV1 have *ee* TAAR, and mixed contribution of *eeh* Auger + *ee* TAAR, respectively. The prominence of TAAR in these valleys is unsurprising as the EDCs are measured in the SRH dominant regime before peak EQE, where *ee* TAAR should be more dominant over *eeh* Auger. In the case of Γ-valley, the 3-body dependence implies that the electrons may have scattered from the higher energy SV1

through intervalley scattering. However, it is also possible for these electrons to be excited directly by *eeh* Auger or *ee* TAAR and scattered into the Γ-valley.[7] For the SV1 and UV2 peaks, the traps involved in their generation by TAAR are most likely located at the AlGaN cap, which was shown to generate TAAR electrons even in a *p*-*i*-*n* device with an AlGaN EBL on the p-side of the junction.[5,7] These deep traps can be located at energies lower than 1.7 eV below the GaN conduction band minimum, thus providing enough energy for an electron to be excited at higher energies position and into UVs at different crystal momenta because of their very localized wavefunction, extended in *k*-space.

For the same J, LOP (or Au PE peak intensity) is much larger for 30SL. While the radiative and Auger recombination coefficients B and C are approximately the same for same active region designs, as discussed prior from the EQE peak position J^*, A is much smaller for 30SL. Since TAAR pathways scale as trap density, as indicated by the absence of UV2 in 30SL's EDCs, B' is also smaller for 30SL. Hence at the same current densities, n must be larger for 30SL. This leads to larger TAAR current and *eeh* Auger recombination currents, corresponding to larger Γ-valley and SV1 peak intensities, respectively, in the 30SL sample.

The observation that with addition of a pre-well SL that (i) A decreases and (ii) total TAAR rate decreases is consistent with the claim that pre-well InGaN layers reduce the concentration of nonradiative recombination centers in the active region.[19] The results are, for most part, in good agreement with Ref. 7 which analyzed a commercial blue LED with AlGaN cap, an EBL layer and thin pre-well SL showing Γ and first SV. However, in Ref. 7 even with thin pre-well SL, no peak was observed at ~1.7 eV above Γ. There are three major differences between the measured sample in Ref. 7 and the green LEDs reported here. First, the LEDs in Ref. 7 have many more quantum wells, part of which may partially perform the same function

as the pre-well SLs; and secondly, the indium content is smaller in the blue wells. It has been proposed that the green gap was caused, in part, by TAAR which is exacerbated by the higher point defect density in green wells (higher In composition).[13] It is possible that the blue LEDs have smaller point defect densities which can act as TAAR pathways. The reason why UV2 is not observed in usual blue LEDs although its energy level lies within reach of *eeh* Auger electrons is not identified at the moment. We speculate that it relies on an interband Auger transition, usually forbidden for conduction electrons near Γ zone center, but which might become allowed for highly localized trapped electrons.[33] More systematic studies of defect-related peaks would be needed to put this on firmer ground.

In conclusion, we have measured hot electrons emitted from green LEDs with and without pre-well SL and quantitatively analyzed their origins. We have shown that in these green LEDs Γ-valley and SV1 electrons are generated by TAAR and *eeh* Auger processes, while there is significant overflow electrons contributing to Γ-valley for the sample with a pre-well SL due to higher active region carrier densities.[7] We have detected hot electrons from a higher energy side valley, in addition to those from the conduction band minimum and first side valley, which is located at ~1.7 eV above the conduction band minimum. Electrons excited to the higher energy side valley are due to TAAR processes. These results agree with the proposition that a pre-well InGaN suppresses defects in the active region, hence with a pre-well SL the TAAR generated UV2 peak decreased in intensity.[19]

References

[1] D.J. Myers, K. Gelžinytė, W.Y. Ho, J. Iveland, L. Martinelli, J. Peretti, C. Weisbuch, and J.S. Speck, Journal of Applied Physics **124**, 055703 (2018).

[2] H.-J. Drouhin, C. Hermann, and G. Lampel, Phys. Rev. B **31**, 3859 (1985).

[3] M. Piccardo, L. Martinelli, J. Iveland, N. Young, S.P. DenBaars, S. Nakamura, J.S. Speck, C. Weisbuch, and J. Peretti, Phys. Rev. B **89**, 235124 (2014).

[4] J. Peretti, H.-J. Drouhin, and D. Paget, Phys. Rev. B **47**, 3603 (1993).

[5] D.J. Myers, K. Gelžinytė, A.I. Alhassan, L. Martinelli, J. Peretti, S. Nakamura, C. Weisbuch, and J.S. Speck, Phys. Rev. B **100**, 125303 (2019).

[6] J. Iveland, M. Piccardo, L. Martinelli, J. Peretti, J.W. Choi, N. Young, S. Nakamura, J.S. Speck, and C. Weisbuch, Appl. Phys. Lett. **105**, 052103 (2014).

[7] W.Y. Ho, Y.C. Chow, D.J. Myers, F. Wu, J. Peretti, C. Weisbuch, and J.S. Speck, Appl. Phys. Lett. **119**, 051105 (2021).

[8] S. Bloom, G. Harbeke, E. Meier, and I.B. Ortenburger, phys. stat. sol. (b) **66**, 161 (1974).

[9] M. Suzuki, T. Uenoyama, and A. Yanase, Phys. Rev. B **52**, 8132 (1995).

[10] A.M. Armstrong, B.N. Bryant, M.H. Crawford, D.D. Koleske, S.R. Lee, and J.J. Wierer, J. Appl. Phys. **117**, 134501 (2015).

[11] S. Schulz, M.A. Caro, C. Coughlan, and E.P. O'Reilly, Phys. Rev. B **91**, 035439 (2015).

[12] M. Auf der Maur, A. Pecchia, G. Penazzi, W. Rodrigues, and A. Di Carlo, Phys. Rev. Lett. **116**, 027401 (2016).

[13] A. David, N.G. Young, C.A. Hurni, and M.D. Craven, Phys. Rev. Applied **11**, 031001(R) (2019).

[14] V.S. Sizov, A.F. Tsatsulnikov, A.V. Sakharov, W.V. Lundin, E.E. Zavarin, N.A. Cherkashin, M.J. Hÿtch, A.E. Nikolaev, A.M. Mintairov, Y. He, and J.L. Merz, Semiconductors **44**, 924 (2010).

[15] X. Wu, J. Liu, Z. Quan, C. Xiong, C. Zheng, J. Zhang, Q. Mao, and F. Jiang, Appl. Phys. Lett. **104**, 221101 (2014).

[16] M. Liu, J. Zhao, S. Zhou, Y. Gao, J. Hu, X. Liu, and X. Ding, Nanomaterials **8**, 450 (2018).

[17] I.A. Prudaev, I.S. Romanov, V.V. Kopyev, V.N. Brudnyi, A.A. Marmalyuk, V.A. Kureshov, D.R. Sabitov, and A.V. Mazalov, Russ Phys J **59**, 934 (2016).

[18] C. Jia, T. Yu, H. Lu, C. Zhong, Y. Sun, Y. Tong, and G. Zhang, Opt. Express **21**, 8444 (2013).

[19] C. Haller, J.-F. Carlin, G. Jacopin, D. Martin, R. Butté, and N. Grandjean, Appl. Phys. Lett. **111**, 262101 (2017).

[20] J. Iveland, L. Martinelli, J. Peretti, J.S. Speck, and C. Weisbuch, Phys. Rev. Lett. **110**, 177406 (2013).

[21] D.J. Myers, A.C. Espenlaub, K. Gelzinyte, E.C. Young, L. Martinelli, J. Peretti, C. Weisbuch, and J.S. Speck, Appl. Phys. Lett. **116**, 091102 (2020).

[22] A.I. Alhassan, R.M. Farrell, B. Saifaddin, A. Mughal, F. Wu, S.P. DenBaars, S. Nakamura, and J.S. Speck, Opt. Express **24**, 17868 (2016).

[23] N. Okada, H. Kashihara, K. Sugimoto, Y. Yamada, and K. Tadatomo, Journal of Applied Physics **117**, 025708 (2015).

[24] Q. Lv, J. Liu, C. Mo, J. Zhang, X. Wu, Q. Wu, and F. Jiang, ACS Photonics **6**, 130 (2019).

[25] A.C. Espenlaub, D.J. Myers, E.C. Young, S. Marcinkevičius, C. Weisbuch, and J.S. Speck, Journal of Applied Physics **126**, 184502 (2019).

[26] S. Chichibu, T. Azuhata, T. Sota, and S. Nakamura, Appl. Phys. Lett. **69**, 4188 (1996).

[27] S. Marcinkevičius, T.K. Uždavinys, H.M. Foronda, D.A. Cohen, C. Weisbuch, and J.S. Speck, Phys. Rev. B **94**, 235205 (2016).

[28] S. Wu, P. Geiser, J. Jun, J. Karpinski, D. Wang, and R. Sobolewski, Journal of Applied Physics **101**, 043701 (2007).

[29] J. Peretti, C. Weisbuch, J. Iveland, M. Piccardo, L. Martinelli, and J.S. Speck, in edited by K.P. Streubel, H. Jeon, L.-W. Tu, and M. Strassburg (San Francisco, California, United States, 2014), p. 90030Z.

[30] H.K. Gummel, IEEE Trans. Electron Devices **11**, 455 (1964).

[31] D.N. Arnold, G. David, D. Jerison, S. Mayboroda, and M. Filoche, Phys. Rev. Lett. **116**, 056602 (2016).

[32] C.-K. Li, M. Piccardo, L.-S. Lu, S. Mayboroda, L. Martinelli, J. Peretti, J.S. Speck, C. Weisbuch, M. Filoche, and Y.-R. Wu, Phys. Rev. B **95**, 144206 (2017).

[33] E. Kioupakis, P. Rinke, A. Schleife, F. Bechstedt, and C.G. Van de Walle, Phys. Rev. B **81**, 241201(R) (2010).

IV. Minority Carrier Diffusion Length in p-GaN

A. Measurement of Minority Diffusion Length in p-GaN using EES

The following section is reproduced mostly from W. Y. Ho, Y. C. Chow, S. P. DenBaars, S. Nakamura, J. Peretti, C. Weisbuch, and J. S. Speck, "Measurement of minority carrier diffusion length in *p*-GaN using electron emission spectroscopy (EES)," *in preparation*.

The minority carrier diffusion length is one of the critical parameters of a material to be considered in the analysis of various semiconductor device performance.[1–3] Various experimental techniques have been implemented for measurement of the carrier diffusion length, such as electron beam induced current (EBIC),[2,4,5] junction-based photocurrent,[6] time resolved four wave mixing, light induced transient grating (LITG),[7,8] surface photo-voltage spectroscopy,[9] and a combination of photoluminescence (PL) spectroscopy and cross-sectional cathodoluminescence (CL) microscopy.[10] In all the aforementioned techniques, the material of interest was measured with external excitations such as electron or optical beam under zero bias conditions, which is different from the conditions of an electrically active device. In most of the techniques, complicated optics and/or modelling are required as well. In this study, we report on determination of the minority carrier diffusion length in *p*-type GaN, L_e measured from electrically active *p-i-n* junctions using Electron Emission Spectroscopy (EES).

The minority carrier diffusion length is one of the important material parameters to be considered in the analysis of a wide variety of semiconductor devices.[1–3] A range experimental techniques have been implemented for measurement of the carrier diffusion length, such as electron beam induced current (EBIC),[2,4,5] junction-based photocurrent,[6] time resolved four wave mixing, light induced transient grating (LITG),[7,8] surface photo-voltage spectroscopy,[9] and a combination of photoluminescence (PL) spectroscopy and cross-sectional cathodoluminescence (CL) microscopy.[10] In all the aforementioned techniques, the material of interest was measured with external excitations such as electron or optical beam under zero bias conditions, which is different from the conditions of an electrically active device. In most of the techniques, complicated optics and/or modelling are required as well. In this study, we report on determination of the electron diffusion length L_e in *p*-type GaN. L_e was determined from electrically active *p*-*i*-*n* junctions using Electron Emission Spectroscopy (EES).

In EES, a device of interest, typically a diode, is introduced into an ultra-high vacuum (UHV) environment.[11–16] The surface of the device is then activated to achieve negative electron affinity (NEA) by depositing cesium or other low work function materials on the surface.[17–19] By lowering the vacuum level to below the bulk conduction band minimum (CBM), the probability of electrons near the surface escaping into vacuum is increased. These electrons travel from the *n*-region where they were injected by the external circuit at the *n*-contact. In their journey through the active region and *p*-region, these electrons experience recombination and scattering, altering their energies, momenta, and concentration. By measuring the emitted electrons' energy distribution, we are able to infer the processes experienced by the electrons.

The (0001) GaN p-i-n epitaxial structures were grown by metal-organic chemical vapor deposition (MOCVD) on a single side polished (0001) sapphire substrate in the following order: unintentionally-doped (UID)-GaN buffer layer, *n*-type GaN:Si layer ([Si] = 4×10^{18} $cm^{-3)}$, 1 μm UID-GaN drift region, 50/75/150/200/300 nm GaN:Mg ([Mg] = 3.5×10^{19} cm^{-3}), and lastly a highly doped 15 nm *p*-contact layer ([Mg] = 3×10^{20} cm^{-3}). The UID region was designed to be thick to ensure low forward leakage current such that the injected carriers pass through the junction instead of leakage pathways.[20] The *p*-thicknesses were determined by calibrating growth rates using X-ray diffraction, where thickness fringes were utilized for thickness determination on a calibration sample. Since it was reported that the diffusion length is highly dependent on the material quality and doping concentration,[21] for thorough comparison we measured the full width half max of the (0002) and $(20\bar{2}1)$ X-ray diffraction peaks on these samples, which are 220 and 350 arcsec, respectively, giving an estimated threading dislocation density (TDD) of 5×10^8 cm^{-3}.[22] The doping concentrations reported were determined using Secondary Ion Mass Spectroscopy (SIMS).

For each sample, a single EES device of honeycomb pattern of area 0.22 mm^2 was made, comprising of an array of 4602 exposed hexagonal p-GaN with an apothem of 2.5 μm separated by 2 μm wide 30 nm Pd/ 300 nm Au metal strips.[13] The ratio of exposed p-GaN to metal area for the device is 45%:55%. The sample was cleaned using HCl and acidic piranha before being introduced into an UHV EES system as described elsewhere.[11] A submonolayer of Cs was deposited (cesiation) using a SAES cesium source while monitoring photoexcited electrons emitted from *p*-GaN, with which NEA was confirmed when the photoemitted current increased and reached a maximum.[11] The escape probability of an electron at the *p*-GaN surface is affected by the position of the vacuum level and the condition of the cesiated

surface. Since it is a function of the emitting surface, we can use the photoemission quantum yield to quantify the escape probability without complications from electron transport and recombination present in electroemission. Photoemission quantum yield measurements were performed on an exposed area of *p*-GaN with no metal coverage using a calibrated focused monochromatic 355 nm beam from an Energetiq Laser Driven Light Source (LDLS) EQ-99X passed through a monochromator, and the photoemitted electrons were collected using a 90 V biased wire.

EES was performed with the devices biased under pulsed mode in the dark, with variable duty cycles, 100% to 5%, for injection currents ranging from 1 to 45 mA corresponding to average current densities ranging from 0.45 to 20.0 A cm^{-2}, respectively. The injection currents and duty cycles were chosen to be low to avoid self-heating without sacrificing signal-to-noise ratio, and to ensure that the junction voltage is below the built-in voltage. The samples were electrically similar with a maximum voltage difference of 0.27 V at 20 A cm^{-2} between samples of different thicknesses. The energy of the emitted electrons was measured referenced to the Fermi level of the *p* contact using a Comstock AC-901 spherical sector electrostatic analyzer operated in constant pass energy mode with an energy resolution of 90 meV.[12] A corresponding set of pulsed and CW measurements were performed using the 90 V collection wire without energy resolution to quantify the collection efficiency of the energy analyzer and Faraday cup.

With increasing diode current, there was an increased ohmic voltage drop across the metal-semiconductor interface that shifted the measured energy of electrons emitted from the semiconductor surface to higher values.[12,13] Inversely, by comparing the energy shift with the applied diode current (or voltage) we can extrapolate the energy shift to expected zero diode

current which should correspond to the bulk CBM. The high energy thresholds of peaks resolved in the energy distribution curves (EDCs) were extracted from the zero-intercept of the positive slopes in the derivatives of the EDCs (DEDCs).[23–25]

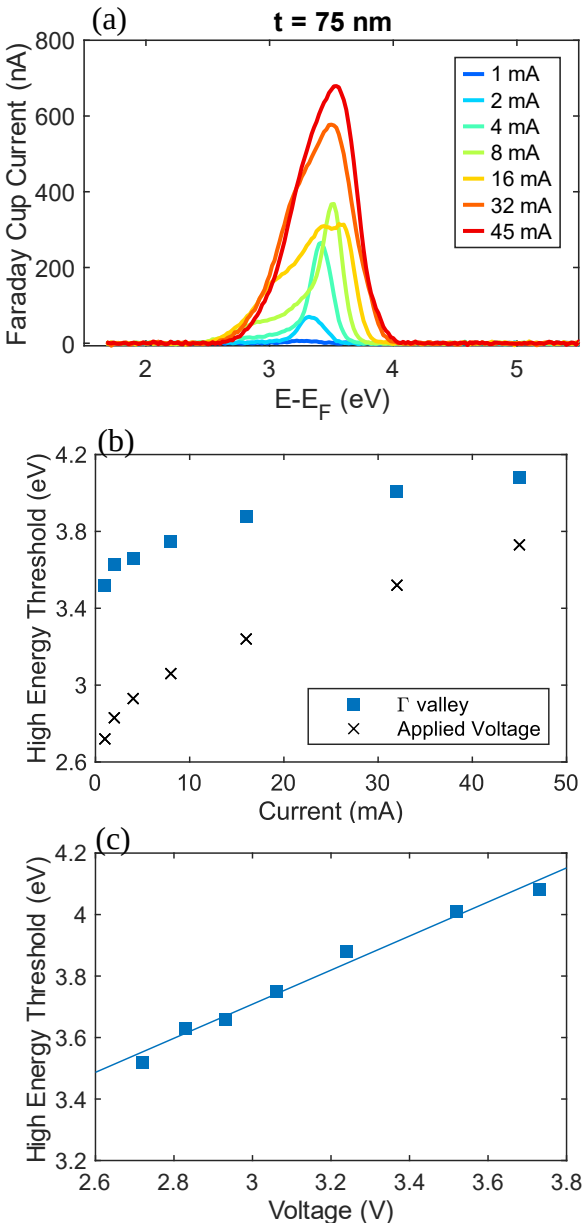

Figure 4.1: The measured energy distribution curves (in terms of Faraday cup current) shown in (a) for the $d_{p-\mathrm{GaN}} = 75$ nm sample, where one distinct peak is observed. The peak has a high energy

threshold of ~3.5 eV at 0.45 A cm^{-2} (1 mA) as shown for the $d_{p-\mathrm{GaN}} = 75$ nm sample in (b), which corresponds to the Γ-valley CBM in GaN and increases with increasing applied diode voltage in (c).

The measured energy distribution curves (EDCs) for the $d_{p-\mathrm{GaN}} = 75$ nm sample at different diode currents are shown in Fig. 4.1 (a), where a main distinguishable peak is observed. The extracted high energy thresholds for this peak increase with increasing applied diode voltage as shown in Figs. 4.1 (b) and (c), indicating its origin to be from the semiconductor. The high energy threshold at 0.45 A cm^{-2} is found to be 3.52 eV above the Fermi level, which corresponds to the bulk CBM (Γ valley) of GaN. The obtained bulk valley minimum is higher than the true value possibly due to additional small voltage drops from the UHV stage clips to the sample p-surface.

The collected currents with and without energy resolution after correction for photoemission quantum yield for various diode currents are plotted in Figs. 4.2 (a) and (b), respectively. Electron current increases by four orders of magnitude with diminished top-layer thickness.

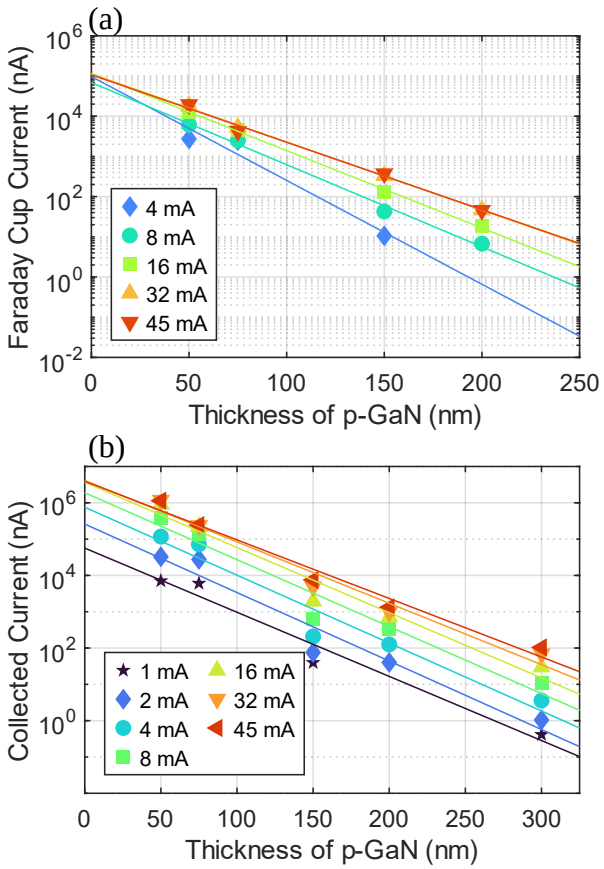

Figure 4.2: The total collected current of electroemitted electrons from (a) the energy analyzer + Faraday cup system, and (b) from the 90 V biased collection wire for different diode currents.

The electron current reaching the surface is governed by the minority carrier diffusion equation. From there, the minority carrier diffusion length, L_e in the p layer is obtained by solving the diffusion equation in the form of:

$$\frac{d^2 n_p}{dx^2} = \frac{n_p}{D_n \tau_n} = \frac{n_p}{L_e^2} \tag{4.1}$$

where n_p is the minority carrier (electrons) concentration in p-GaN, $D_n = \sqrt{k_B T \mu_n / q}$ the diffusion coefficient at temperature T for electron mobility μ_n, τ_n the lifetime of the

electrons, while k_B and q have their usual meanings of Boltzmann constant and electron charge. After applying relevant boundary conditions, this equation has solutions of the form:

$$n_p(x) = n_p(x = 0)e^{-\frac{x}{L_e}}$$

or equivalently:

$$I_{\text{emitted}}(x) = I_0 P_{\text{esc}} e^{-\frac{x}{L_e}}$$

$$\ln[I_{\text{emitted}}(x)] = -\frac{1}{L_e}\ln x + \ln(I_0 P_{\text{esc}}) \tag{4.2}$$

where I_0 is the electron current at the active region and *p*-GaN interface, x is the distance travelled by the minority carriers, and I_{emitted} is the current collected after correcting for the escape probability of the electrons, P_{esc} from the emitting surface in the form of quantum yield.

The photoemission quantum yield measured at 355 nm ranges from 0.3% to 1.3% for the series. The total collected currents for measurements with energy resolution is obtained by summing over the entire EDC, where correction is applied for the pulsed EDCs by dividing by their corresponding duty cycles. All measurements yielded good fits to equation 4.2 (Pearson's coefficients, $R^2 = -0.98$), yielding an average diffusion length of 23.8 nm from the EDCs and 24.5 nm from the collection wire. For the EDCs it is possible that there is signal masking from the background noise for lower current densities in thicker *p*-GaN samples. Hence the obtained peak intensities may be smaller than the true values, resulting in a smaller fitted diffusion length than that obtained from the collection wire. The diffusion lengths obtained appeared to increase with increasing diode current, which we speculate to be due to

an increase in τ_n. With increased excess carriers, we expect reduced loss of electrons through deep traps, hence an increase in the overall lifetime of the electrons.[26–28]

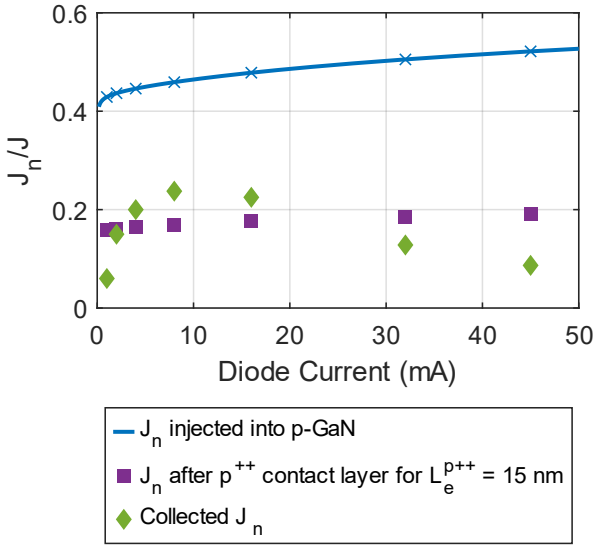

Figure 4.3: The simulated ratio of injected electron current into the UID-GaN and p-GaN region is plotted as a function of diode current. At 1 mA (45 mA), only 43% (corresponding 52%) of the injected diode current is simulated to be injected into the *p*-GaN as electrons.

As the EES system only detects electrons and not holes, to analyze the *y*-intercept of the fits – the expected current collected without *p*-GaN in these *p-i-n* diodes, I_0 – we must first calculate the injected electron current at the interface of the UID-GaN and *p*-GaN. Using a 1D Poisson-drift-diffusion solver based on the Localization Landscape Theory, the current – voltage ($J-V$) characteristics of these devices were simulated.[29–31] The non-radiative recombination lifetimes for electrons and holes in UID-GaN is set to be 100 ns, which is likely a lower bound. The simulated fraction of current injected into p-GaN as electrons, J_n/J is

plotted in Figure 4.3. J_n/J is found to be varying with injected current, varying from 43% for 1 mA to 52% for 45 mA. This is due to the long journey taken by electrons through the thick UID-GaN, where scattering and recombination take place. Assuming a diffusion length of 15 nm for the highly doped 15 nm thick *p*-contact region,[32] the fraction of simulated current collected is within a factor of two of the extrapolated value from the measured data as shown in Figure 4. The factor of two may be due to the division of electron current between emissive p-GaN surface and the metal contacts, which has a fill factor of 45:55. This would imply that most injected electrons which survived to the p-surface are emitted and collected. However, there is a clear trend of decreasing extrapolated electron current injected into the *p*-region which is unaccounted for.

In the literature, minority carrier diffusion length in *p*-GaN measurements based on EBIC techniques reported a wide range of values from 41 to 200 nm, where larger EBIC acceleration voltages appear to correlate to larger measured values.[2,21,33–35] While larger acceleration voltages probes deeper, depth dependent and cross-sectional EBIC measurements in Ref. 24 reported consistent L_e of ~41 nm between the two different EBIC methods.[33] The measured L_e values reported here are on the lower end of this range of values and are in reasonable agreement with Ref. 33.[33] In Ref. 10, there is complication in using the PL intensities due to having two possible sources of carriers generating the PL spectrum – by diffusion from the p-GaN or by direct photoexcitation, yielding an L_e value of 93 ± 7 nm. This value is four times larger than our reported value possibly because of a larger diffusion coefficient or larger recombination lifetimes due to the high photoexcitation conditions employed.[10,26–28,36] The photoexcited carrier densities were in excess of 10^{18} cm^{-3} while our measurements yielded

electron densities ~ 10^{15} to 10^{17} cm^{-3}. This agrees with our observed trend that with higher current densities the measured diffusion length increases.

In conclusion, we have measured electrons emitted from a series of *c*-plane GaN *p*-*i*-*n* devices with variable *p*-GaN thicknesses. We have showed that the electrons originate from the CBM of GaN and decrease in intensity with increasing *p*-GaN thickness, yielding minority carrier diffusion length of ~24.5 nm.

B. Atomic Layer Etching (ALE) for p-GaN Quantitative Studies

In the previous section, we discussed the measurement of minority carrier diffusion length by growing *p*-*i*-*n* junctions with different *p*-GaN thicknesses. Care was taken to ensure that the diode ideality factors, turn-on voltages, and reverse leakage currents are similar – to ensure that the diodes in the grown series are as identical as possible such that any observed differences can be attributed entirely to the difference in *p*-GaN thicknesses. This poses additional cost in growth and material. In theory, similar studies can be performed on LEDs grown with variable *p*-thicknesses to extract the true recombination currents and hot electrons generated by the active region. In the process, it may be possible to study intervalley scattering between the various GaN valleys. However, we are then limited to studies where the epitaxial structures are specially grown for these specific purposes.

One technique that can potentially enable such quantitative research to all LEDs, or other III-Nitride devices, is the use of Atomic Layer Etching (ALE). By performing controlled, low damage etching of the *p*-layer on the same device, we can ensure that the devices are nominally identical below the *p*-region. The devices of interest no longer must be grown

customized for the experiment and can be a run-of-the-mill commercial device. The technology of ALE dates to 1990, where the first ALE etching of Si was demonstrated.[37] ALE of GaAs Ge trails after with first reports in 1996,[38] Ge in 1997,[39] and GaN in 2002.[40]

In each cycle, etching is usually achieved by first dosing the sample surface with Cl_2 gas, with which Cl adsorbs onto the dangling bonds material surface. This step lowers the energy required for thermal desorption of the Cl-terminated top layer. Once the surface is saturated with chlorine, the chamber was evacuated. In the third step, the energy required for such desorption is provided typically by an Ar^+ ion plasma. The chamber is once again pumped down in preparation for the next cycle.

However, the technology for GaN is far from mature – with most recent publications reporting some form of damage to the etched surface and/or sidewalls.[41–43] Fukumizu et al. observed degradation of near band edge emission of AlGaN surface layer etched using Cl_2/Ar ALE chemistry, with increased damage for increased exposure to the Ar plasma.[42] Ruel et al. reported degradation of sheet resistance of the etched surface, with a 500% change when a He ion ALE process was used. They also reported recovery using additional N_2 annealing.[43]

The following work discusses the various characterization performed to justify or disqualify use of present ALE technology for EES purposes. Firstly, the degree of etch damage affects the emitting surface and transport properties, introducing surface traps which may alter the cesiation behavior, quantum yield, and emission spectra. Secondly, the etch damage will modify transport properties throughout the damaged region – introducing scattering centers and altering diffusion lengths. If the depth of damage is large, it also places an upper limit on etch depth, as further etches will result in damages to the active region, altering the devices altogether.

The Oxford PlasmaPro 100 Cobra is an inductively-coupled plasma (ICP) etcher with ALE capabilities. The ALE performed in this chapter uses the standard Cl_2/Ar^+ as adsorption gas and sputtering ion source, with the parameters listed in Table 1 as recommended by the supplier:

Cl_2 exposure time (t_{Cl})	**0.04 s**
Chamber pressure during Cl_2 dose, P_{Cl}	15 mTorr
Cl_2 flow rate	50 sccm
Cl_2 exhaust time	6.00 s
Ar^+ exposure time (t_{Ar})	3.50 s
Chamber pressure during Ar^+ dose, P_{Ar}	10 mTorr
Ar flow rate	100 sccm
Ar^+ plasma power	10 W
Ar exhaust time	1.50 s
T_{sub}	20℃

Table 4.1: The conditions during atomic layer etching in the Oxford PlasmaPro 100 Cobra.

For comparison, accompanying studies were performed in a PlasmaTherm (Uniaxis) Reactive Ion Etcher using BCl_3/Cl_2 with bias power of 15 W at 14 mTorr pressure, which is henceforth referred to as Reactive Ion Low Power Etching (RI-LPE).[44]

i. Etch rate reproducibility

To use the etch technique reliably, we must first ensure that the etch rate is self-limiting (to be ALE) and reproducible. This is also crucial if we are to compare the technique with other etch techniques. Samples were grown for the purpose of etch calibration using ammonia molecular beam epitaxy (MBE), plasma-assisted MBE (PAMBE) and metal-organic chemical vapor deposition (MOCVD), which typically comprise of a *p*-GaN or UID-GaN on AlN. The range of growth techniques and GaN doping is essential to account for etch rate difference

due to crystal quality and doping, if any. The layer thicknesses are then determined by measuring fringe separation of the (002) scan using X-Ray Diffractometer (XRD).

Different etch calibration runs were performed over a few different days, where the difference is in one or more of the following: i) number of etch cycle, ii) day of run, or iii) pre-etch conditions. The different etch experiments performed are listed in Table 4.2, while the average etch rate per cycle is plotted in Fig. 4.4.

Run	**Sample (Source, type)**	**Wet clean**	**Pre-etch conditioning**
1	Ammonia MBE, UID	BHF	10 mins Cl_2/O_2
2	PAMBE, UID	HCl	10 mins Cl_2/O_2
3	MOCVD, UID	HCl	10 mins Cl_2/O_2, 50-cycle ALE

Table 4.2: The different etch runs performed for etch rate calibration.

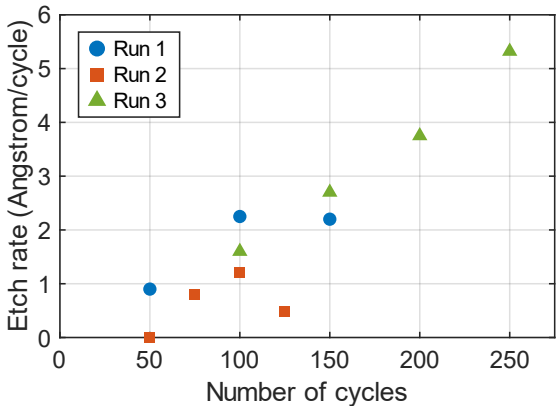

Figure 4.4: The average etch rate per cycle for the different etch runs performed. For Runs 1 to 3, there is a strong dependence of etch rate on the number of etch cycles. The data point at 125 cycles is an outlier due to machine error and should not be considered.

In Runs 1 to 3, we observe a submonolayer etch per cycle (< 2.3Å/cycle) for number of etch cycles < 100. In these runs, every etch was performed on a different day on the same

sample, and the number of cycles was randomized. Since there is a minimum number of etch cycles required for etch to take place, it was concluded that there is an etch barrier for ALE of GaN, possibly due to the presence of a native oxide. While the difference in etch rate per cycle of Run 1 and Run 2 may be due to crystal quality differences between ammonia MBE and PAMBE grown UID-GaN, the larger etch barrier for Run 2 and Run 3 suggests that the native oxide does affect the etch barrier and a pre-etch BHF treatment is preferred over an HCl dip. Another possible source of etch barrier is the chamber conditions pre-etch, which may be contaminated by other etch gases and can be solved by a longer pre-etch chamber clean and blank ALE runs for chamber conditioning. In Run 3, a 50-cycle conditioning ALE step was performed, but it clearly does not affect the etch barrier significantly.

Another major concern in Run 3 was that the etch rate per cycle increases linearly with number of etch cycles. This implies that the etch is not self-limiting, which is undesirable. We observed that the samples heat up from the ion bombardment during the sputter step. Since etch was performed by supplying the required energy for the top layer to desorb through Ar ions, increasing the sample temperature will reduce the amount of ion energy required. It is possible that the current etch conditions are in the sputtering regime rather than ALE regime. It is also possible that the "activated" layer was more than one monolayer, ie. the chlorine atoms supplied in the chemisorption step bonded with more than one monolayer. This may be solved by having shorter Cl_2 dose time or longer Cl_2 exhaust time.

We repeated the experiment with a longer pre-etch chamber clean, increasing from 10 to 30 mins of Cl_2/O_2. To decouple the effect of crystal quality from the etch parameters, we used MOCVD grown samples only for Run 4. Samples for Runs 5 and 6 are co-loaded to remove run-to-run variation to distinguish effect of sample doping on the etch rate. The different runs

are detailed in Table 4.3, while the etch rate per cycle for all the runs are summarized in Figure 4.5.

Run	Sample (Source, type)	Wet clean	Pre-etch conditioning
4	MOCVD, Mg-doped	BHF	30 mins Cl_2/O_2, 75-cycle ALE
5	MOCVD, UID	HCl	30 mins Cl_2/O_2, 75-cycle ALE
6	MOCVD, Mg-doped	HCl	30 mins Cl_2/O_2, 75-cycle ALE

Table 4.3: The different etch runs performed for etch rate calibration with increased pre-etch chamber clean.

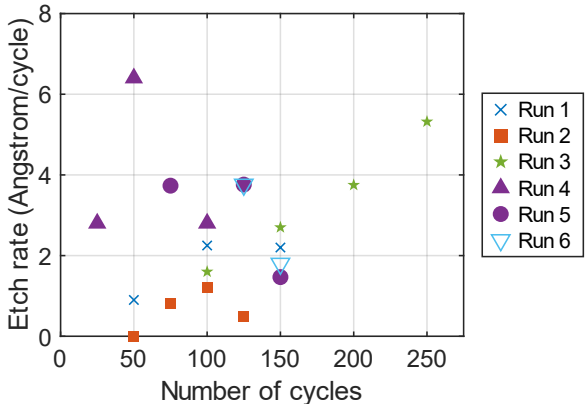

Figure 4.5: The average etch rate per cycle for the different etch runs performed. For Runs 1 to 3, there is a strong dependence of etch rate on the number of etch cycles.

The etch barrier is clearly removed for Runs 4 to 6. The etch rate per cycle is found to be unaffected by the doping of the material. For most etches an etch rate of approximately one monolayer per cycle was obtained. A few anomalies were measured at 50 cycles and 150 cycles, the cause of which was not identified.

ii. **Smoothness of etch and lithographic compatibility**

With the etch rate per cycle now reasonably consistent, we turn our attention to the damage resulting from the dry etch. If the dry etch damage is substantial, we may observe a large change in surface morphology of the etched surfaces. In Figure 4.6, atomic force microscopy (AFM) of etched PAMBE samples indicate that there is no added surface roughness, with the etch being mostly conformal, with a small smoothing effect at larger etch cycles.

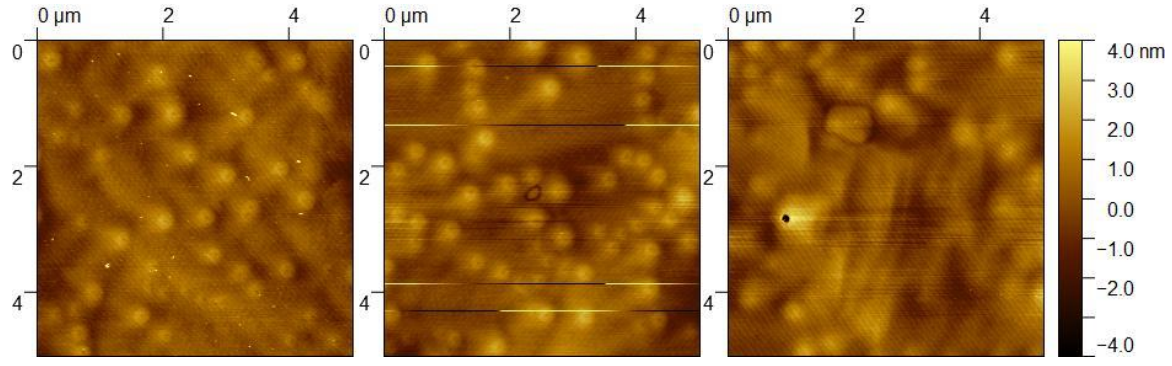

Figure 4.6: Atomic Force Micrographs of a PAMBE grown UID-GaN sample after different number of ALE cycles. The average r.m.s. roughness remains in ~1 nm, unchanged from unetched sample to post 225 cycle of etches. A deep hole was exposed after 225 cycles, which may be a previously buried defect in the sample. Images courtesy of Zachary Biegler.

The average roughness remains ~1 nm from pre-etch to post 225 etch cycles. A deep hole was exposed after 225 cycles of etching, which may be a previously buried extended defect in the sample. This hinted at the possibility of exposing filled-in V-defects in LEDs for V-defect characterization. We hence repeated the etches using commercial *c*-plane LEDs grown, with lithographically defined features to ensure lithography compatibility of the etch technique. This is essential for EES, where there is advantage to etching only the exposed

apertures to ensure ohmic *p*-contact. As native oxides serve as an etch barrier, a potential hard mask for the etch is SiO_x. For characterization of the etched surface, we employed a scanning electron microscope (SEM) and AFM, as shown in Figure 4.7. A comparison was made with RI-LPE, as indicated in Figure 4.8.

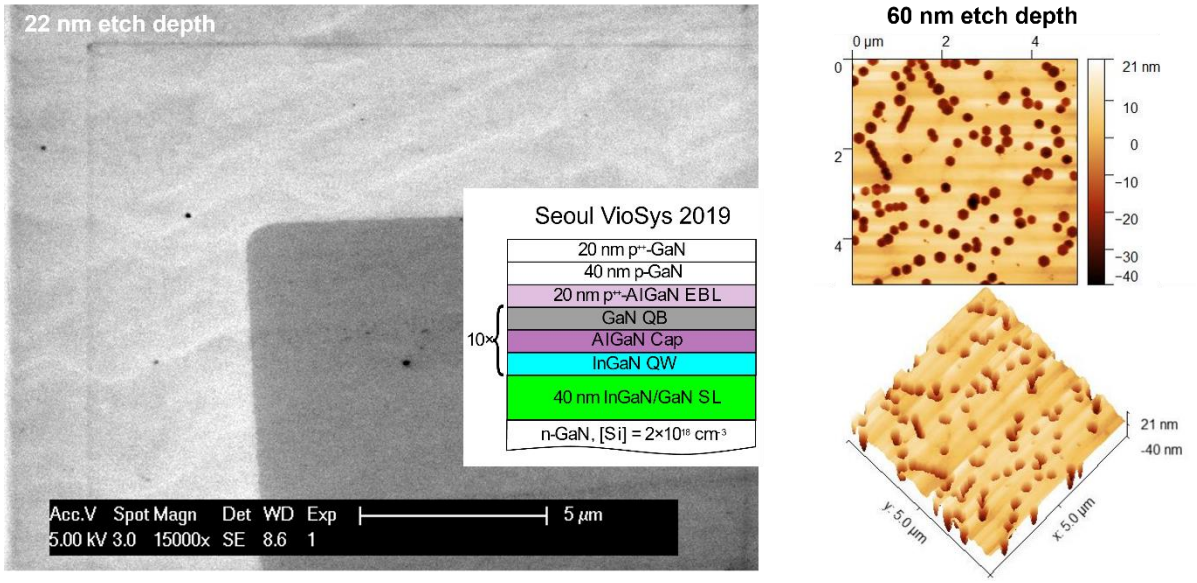

Figure 4.7: At shallow etch depths (22 nm) the etch was conformal and smooth as demonstrated by the SEM image on the left ; while at deeper etch depths (66 nm) V-defects were exposed and is clearly resolved using AFM (right). SEM image courtesy of Tanay Tak, AFM images courtesy of Kai Shek Qwah.

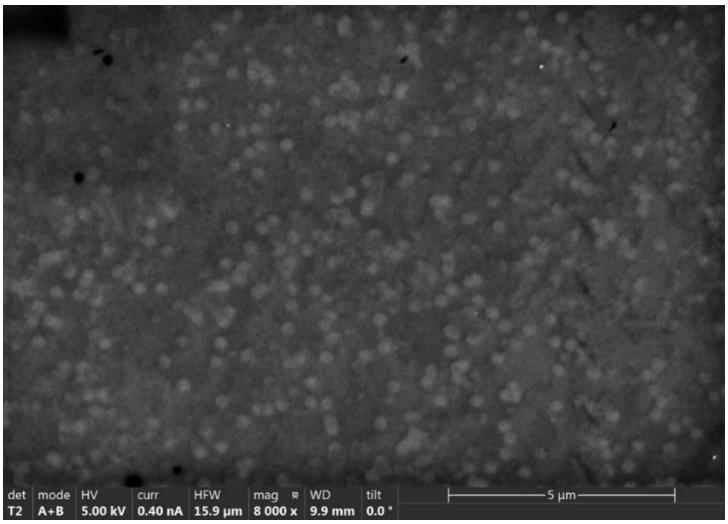

Figure 4.8: SEM image showing numerous craters arising either from damage or due to material removal by RI-LPE. Image courtesy of Zachary Biegler.

The etched surface at 22 nm etch depth as observed in SEM is smooth with no visible craters, with clear patterning arising from the SiO_x hard mask and ensuring its lithography compatibility. The etched surface at 22 nm using RI-LPE showed numerous craters, which are damaged regions from the dry ion bombardment. The lack of such craters in ALE is encouraging that the dry etch damage may be sufficiently low for EES purposes.

When a deeper etch was employed (150 cycles), it was observed that the etched surface was full of hexagonal shaped pits which extends below and past the top quantum wells. A quick calculation using the 2×2 μm AFM scans indicated a density of 6×10^8 cm^{-3}, which corresponds well to the expected V-defect density in this sample. The well-defined pits indicate that the etch conditions employed suggest selective etching of GaN over AlGaN, making ALE a great tool for systematic etch back of LEDs for quick V-defect characterization without the need for growth interrupts.

iii. **Photoluminescence of single quantum well LED**

We can characterize the depth of the damage by etching structures containing single quantum wells.[45,46] The epitaxial structure grown by MOCVD is schematically shown in Figure 4.9. A blue $In_{0.15}GaN$ quantum well is grown sandwiched between UID-GaN layers with pre-well superlattice structure on double-side polished sapphire. The top UID-GaN is 100 nm thick, which will be systematically etched towards the quantum well using ALE and RI-LPE.

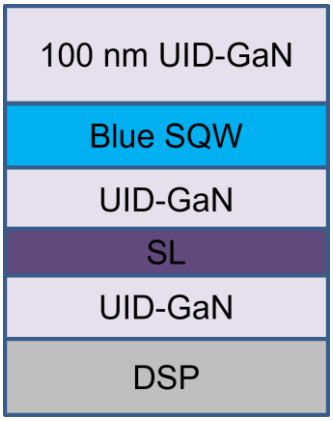

Figure 4.9: The epitaxial structure grown for determination of the depth of damage.

Should the QWs be damaged due to the dry etch, we would expect a drop in photoluminescence (PL) intensity.[45,46] The distance from the QW at which the PL intensity decrease is first observed corresponds to the depth of the damage.[45,46] The etch depth was measured using XRD, and the PL spectrum resonantly excited using a 375 nm pump laser for different etch depth using ALE and RI-LPE is plotted in Figure 4.10 (a) and (b), respectively.

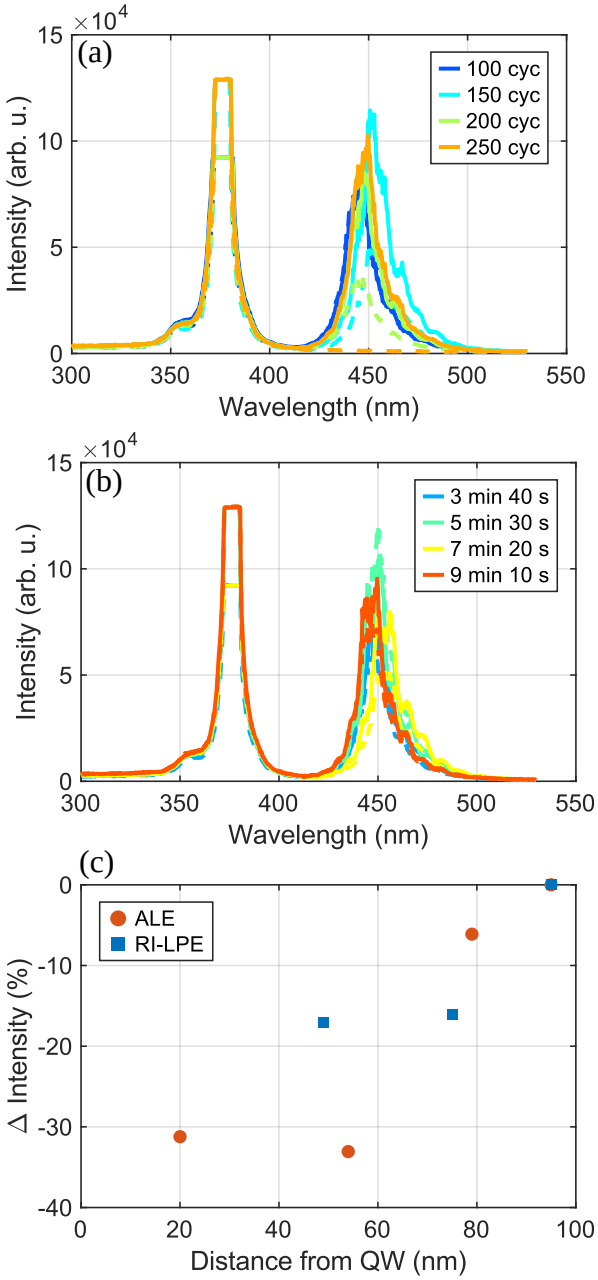

Figure 4.10: The PL spectrum before (solid lines) and after (dashed lines) the (a) ALE and (b) RI-LPE etches are plotted. The integrated change in intensity of PL is shown in (c).

The damage is lower for ALE at small etch depths, while at larger etch depths past 40 nm ALE appears to have a larger etch damage. Regardless, at 80 nm etch depth corresponding to

20 nm from the quantum well the PL intensity is unchanged from that of ~55 nm from the quantum well, which is a 30% loss in signal. This implied that from 150 to 200 cycles of ALE there is no accumulated damage due to the additional cycles. It is possible that though the damage is ~55 nm deep, it is minimal. Similarly for RI-LPE, even though the damage is 80 nm deep, the damage is not observed to accumulate from the additional 3 mins of etch time. A repeat of this experiment for both etching techniques to larger etch depths closer to the quantum well is required to ensure that the drop in PL intensity is a real trend on not an artifact of noise.

iv. **Sheet resistance from circular transmission line measurements**

We attempt to quantify the degree of damage due to the etch by measuring the sheet resistance, R_S of the etched regions using circular transmission line measurements (CTLMs). In CTLM measurements, the metal contact of interest is patterned such that there exists an annular gap between the inner circular metal pads and the outer metal pads.

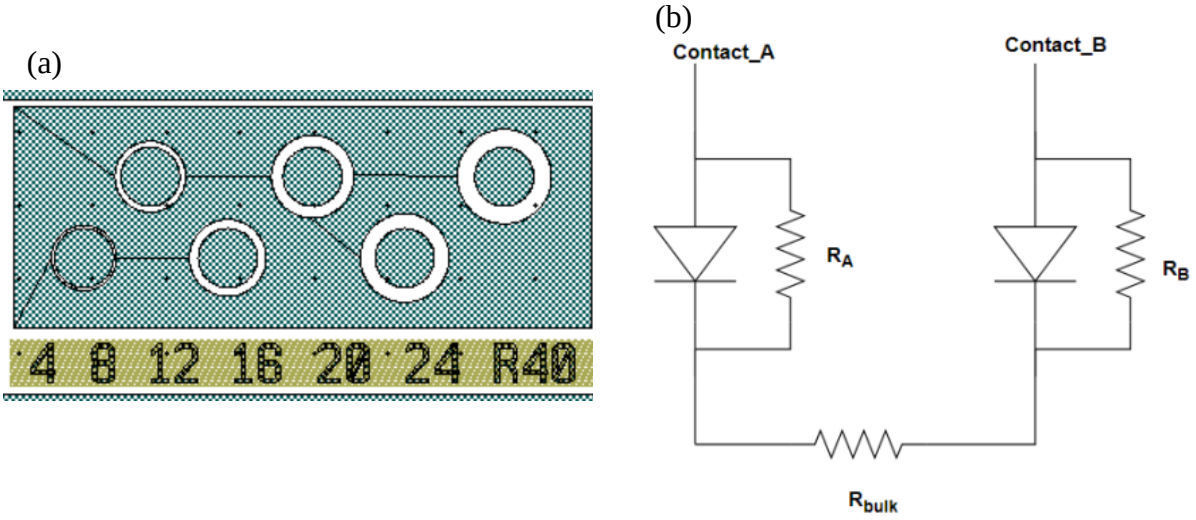

Figure 4.11: (a) Schematic of the CTLM structures used in this section. The equivalent electrical circuit of a measurement is drawn in (b).

The $I-V$ across the different annular gaps as shown in Fig. 4.11 are measured, which will have varying resistances due to the larger distances between the metal pads. The full analytical solution to the $I-V$ assuming ohmic behavior is hence:

$$V_{\text{measured}} = \frac{I_{\text{applied}} R_S}{2\pi}\left[\ln\left(\frac{r_1}{r_0}\right) + \frac{L_T}{r_0}\cdot\frac{I_0\left({}^{r_0}/_{L_T}\right)}{I_1\left({}^{r_0}/_{L_T}\right)} + \frac{L_T}{r_1}\cdot\frac{K_0\left({}^{r_1}/_{L_T}\right)}{K_1\left({}^{r_1}/_{L_T}\right)}\right]$$

where I_{applied} and V_{measured} are the applied current and measured voltage (or vice versa); r_0 and r_1 are the inner and outer radii of the annulus as indicated in Fig. 4.11; L_T is the transfer length of the contact-semiconductor interface; and I_α, K_α are modified Bessel functions of the first and second kind of order α, respectively.[47–49] The specific contact resistivity of the interface is hence $\rho_C = R_S {L_T}^2$.

Two 100 nm *p*-GaN samples were grown using MOCVD on top of thick UID-GaN and single side polished sapphire. The doping of the samples are [Mg] $= 2 \times 10^{20}$ cm^{-3} and [Mg] $= 5 \times 10^{19}$ cm^{-3}, respectively. The highly doped sample, henceforth referred to as HDp, correspond to a typical highly doped *p*-contact layer. The lower doped sample, henceforth referred to as LDp, correspond to standard doping in the *p*-layer. The samples are subjected to 100/200/300 cycles of ALE for 22/44/66 nm etch depth. A parallel set of etches of same depth was performed using RI-LPE. The *p*-metal contact, 30/300 nm of Pd/Au, was patterned and deposited post-etch.

While in application the CTLM analytical equation can be applied to any reasonably ohmic contact, it is important to distinguish between an ohmic contact and a Schottky contact. In the latter, the diode contribution will show up as a current barrier, which is evident in Figure

4.12 (b). As such, a direct application of the CTLM equation will overestimate the sheet resistance while underestimating the specific contact resistance.

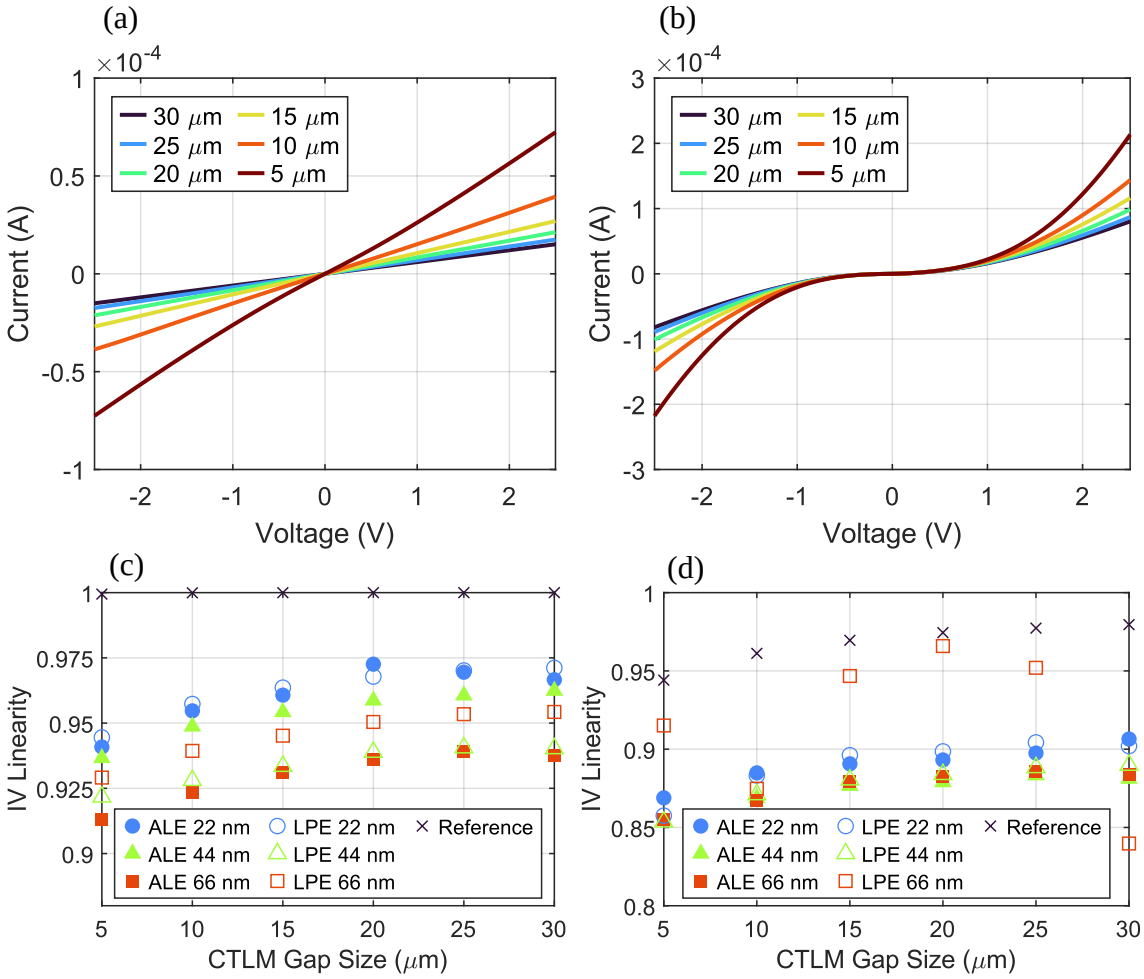

Figure 4.12: The $I-V$ curves of different gap sizes for the unetched HDp and LDp samples contacted by 30/300 nm Pd/Au is plotted in (a) and (b), respectively. The corresponding Pearson's coefficients are plotted in (c) and (d), respectively.

The ohmicity of the contacts can be represented by their linearity in terms of Pearson's coefficients. An ohmic contact will have Pearson's coefficient of 1, and the contact is Schottky otherwise. For the unetched HDp, we observed perfectly ohmic behavior as expected (Fig. 4.12 (a) and (c)). For LDp, we observe a Schottky contact even for the unetched reference

(Fig. 4.12 (b) and (d)). In general, the larger gap size devices have higher linearity due to the larger resistance component compared to the diode component of a Schottky contact. We note that the LPE 66 nm etched LDp sample has erratic linearity with increasing gap size, indicating large damage and cannot be characterized using CTLM.

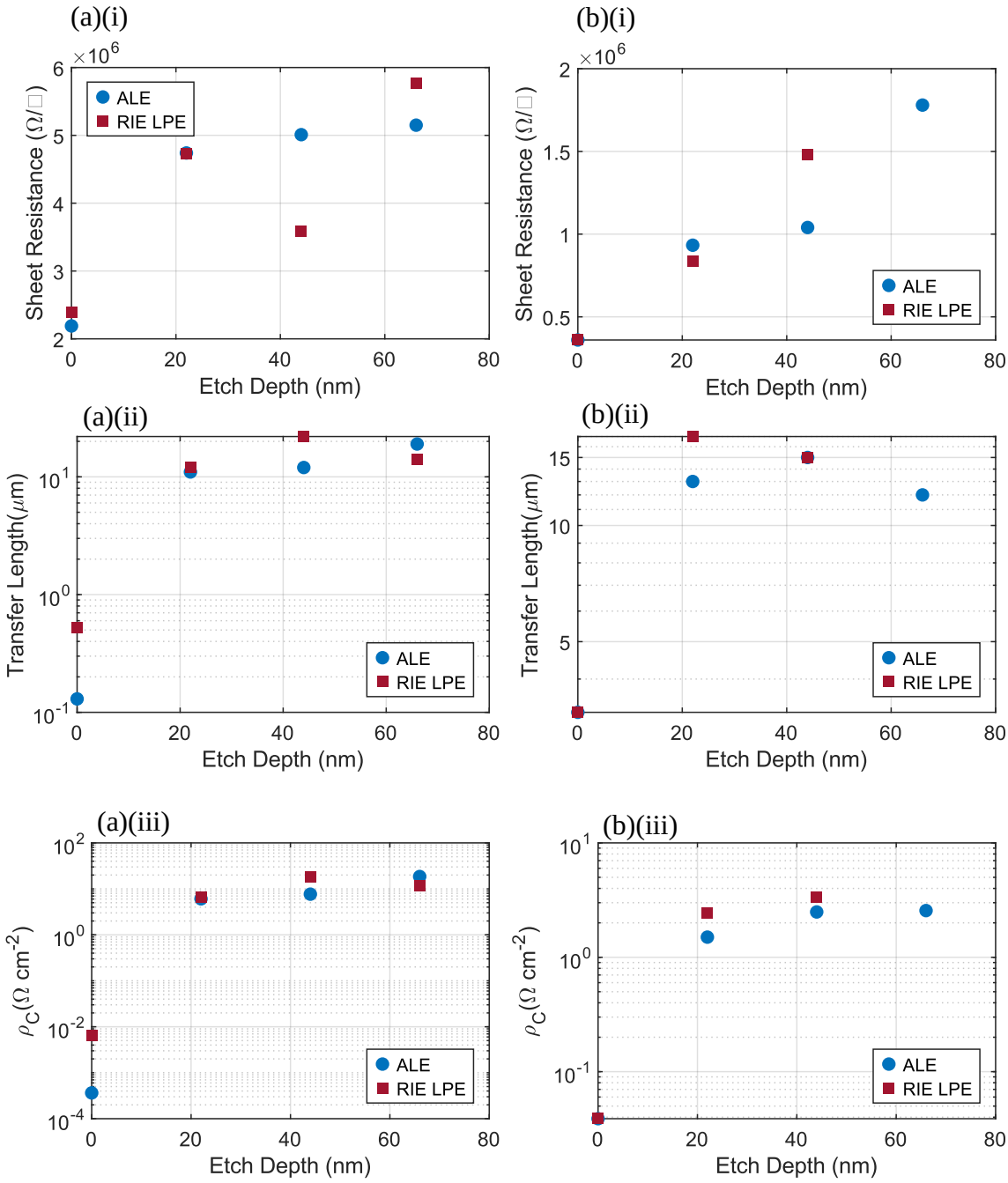

Figure 4.13: The fitted sheet resistance, transfer length and specific contact resistances for HDp and LDp etched using ALE and RI-LPE. In both etch techniques, the sheet resistances increased after dry etching.

For HDp, there is a sharp increase in sheet resistance, transfer length and hence specific contact resistivity from reference to 22 nm etch, whether by ALE or by RI-LPE, as shown in Fig. 4.13 (a)(i) – (iii). This may be attributed to the change in [Mg] doping with depth. Mg is known to ride surfaces and accumulate, which typically aids in high [Mg] doping at *p*-GaN surfaces for contact. This effect is more pronounced in highly doped *p*-GaN. There is little difference comparing 22 nm, 44 nm, and 66 nm etched HDp samples in both techniques, hinting at little to no damage for both ALE and RI-LPE.

In contrast, the etched LDp samples demonstrated a clear trend with increasing etch depth, as shown in Fig. 4.13 (b)(i). This is true for both ALE and RI-LPE. Since the doping is lower, the [Mg] doping is expected to be uniform throughout the etched regions investigated. Hence, we can conclude that the longer the sample was exposed to dry etching, the larger the sheet resistance is. The sheet resistance doubled from unetched to 22 nm etch depth. The RI-LPE 66 nm on LDp sample cannot be characterized using CTLM, possibly due to the roughness of the etched surface yet also indicative of large damage.

In conclusion, our studies generally indicate that ALE is only slightly advantageous in performance to RI-LPE in terms of damage. Morphologically, ALE is significantly superior to RI-LPE, being highly “conformal” with no added roughness due to etch. A damage recovery step post-etch is highly desirable and should be developed before employing either of the investigated dry etch techniques for quantitative study purposes. The finite thickness of damaged region places a lower bound on the remnant *p*-layer thickness in these studies, which

can be designed around experimentally. Ideally, further damage characterization experiments should be carried out, ie. Hall measurements should be conducted for mobility measurements.

References

[1] H.C. Casey, B.I. Miller, and E. Pinkas, Journal of Applied Physics **44**, 1281 (1973).

[2] Z.Z. Bandić, P.M. Bridger, E.C. Piquette, and T.C. McGill, Appl. Phys. Lett. **73**, 3276 (1998).

[3] W. Götz, N.M. Johnson, J. Walker, D.P. Bour, and R.A. Street, Appl. Phys. Lett. **68**, 667 (1996).

[4] L. Chernyak, A. Osinsky, H. Temkin, J.W. Yang, Q. Chen, and M. Asif Khan, Appl. Phys. Lett. **69**, 2531 (1996).

[5] Z.Z. Bandić, P.M. Bridger, E.C. Piquette, and T.C. McGill, Appl. Phys. Lett. **72**, 3166 (1998).

[6] D. Wee, G. Parish, and B. Nener, Journal of Applied Physics **111**, 074503 (2012).

[7] T. Malinauskas, R. Aleksiejūnas, K. Jarašiūnas, B. Beaumont, P. Gibart, A. Kakanakova-Georgieva, E. Janzen, D. Gogova, B. Monemar, and M. Heuken, Journal of Crystal Growth **300**, 223 (2007).

[8] E.V. Lutsenko, A.L. Gurskii, V.N. Pavlovskii, G.P. Yablonskii, T. Malinauskas, K. Jarašiūnas, B. Schineller, and M. Heuken, Phys. Status Solidi (c) **3**, 1935 (2006).

[9] Y. Lin, E. Flitsyian, L. Chernyak, T. Malinauskas, R. Aleksiejunas, K. Jarasiunas, W. Lim, S.J. Pearton, and K. Gartsman, Appl. Phys. Lett. **95**, 092101 (2009).

[10] S. Hafiz, F. Zhang, M. Monavarian, V. Avrutin, H. Morkoç, Ü. Özgür, S. Metzner, F. Bertram, J. Christen, and B. Gil, Journal of Applied Physics **117**, 013106 (2015).

[11] J. Iveland, L. Martinelli, J. Peretti, J.S. Speck, and C. Weisbuch, Phys. Rev. Lett. **110**, 177406 (2013).

[12] J. Iveland, M. Piccardo, L. Martinelli, J. Peretti, J.W. Choi, N. Young, S. Nakamura, J.S. Speck, and C. Weisbuch, Appl. Phys. Lett. **105**, 052103 (2014).

[13] D.J. Myers, K. Gelžinytė, W.Y. Ho, J. Iveland, L. Martinelli, J. Peretti, C. Weisbuch, and J.S. Speck, Journal of Applied Physics **124**, 055703 (2018).

[14] D.J. Myers, K. Gelžinytė, A.I. Alhassan, L. Martinelli, J. Peretti, S. Nakamura, C. Weisbuch, and J.S. Speck, Phys. Rev. B **100**, 125303 (2019).

[15] D.J. Myers, A.C. Espenlaub, K. Gelzinyte, E.C. Young, L. Martinelli, J. Peretti, C. Weisbuch, and J.S. Speck, Appl. Phys. Lett. **116**, 091102 (2020).

[16] W.Y. Ho, Y.C. Chow, D.J. Myers, F. Wu, J. Peretti, C. Weisbuch, and J.S. Speck, Appl. Phys. Lett. **119**, 051105 (2021).

[17] M.C. Benjamin, M.D. Bremser, T.W. Weeks, S.W. King, R.F. Davis, and R.J. Nemanich, Applied Surface Science **104–105**, 455 (1996).

[18] M. Eyckeler, J. Vac. Sci. Technol. B **16**, 2224 (1998).

[19] T.U. Kampen, M. Eyckeler, and W. Mönch, Applied Surface Science **123–124**, 28 (1998).

[20] C.A. Robertson, Defect-Mediated Carrier Transport Mechanisms in Vertical GaN p-n Diodes, University of California, Santa Barbara, 2019.

[21] K. Kumakura, T. Makimoto, N. Kobayashi, T. Hashizume, T. Fukui, and H. Hasegawa, Appl. Phys. Lett. **86**, 052105 (2005).

[22] C. Lynsky, R.C. White, Y.C. Chow, W.Y. Ho, S. Nakamura, S.P. DenBaars, and J.S. Speck, Journal of Crystal Growth **560–561**, 126048 (2021).

[23] H.-J. Drouhin, C. Hermann, and G. Lampel, Phys. Rev. B **31**, 3859 (1985).

[24] J. Peretti, H.-J. Drouhin, and D. Paget, Phys. Rev. B **47**, 3603 (1993).

[25] M. Piccardo, L. Martinelli, J. Iveland, N. Young, S.P. DenBaars, S. Nakamura, J.S. Speck, C. Weisbuch, and J. Peretti, Phys. Rev. B **89**, 235124 (2014).

[26] G. Bemski, Phys. Rev. **100**, 523 (1955).

[27] J.S. Blakemore, Phys. Rev. **110**, 1301 (1958).

[28] G.B. Abdullaev, Z.A. Iskender-Zade, E.A. Dzhafarova, and V.E. Chelnokov, phys. stat. sol. (b) **21**, 423 (1967).

[29] H.K. Gummel, IEEE Trans. Electron Devices **11**, 455 (1964).

[30] D.N. Arnold, G. David, D. Jerison, S. Mayboroda, and M. Filoche, Phys. Rev. Lett. **116**, 056602 (2016).

[31] C.-K. Li, M. Piccardo, L.-S. Lu, S. Mayboroda, L. Martinelli, J. Peretti, J.S. Speck, C. Weisbuch, M. Filoche, and Y.-R. Wu, Phys. Rev. B **95**, 144206 (2017).

[32] D.J. Myers, Electron Emission Spectroscopy of III-N Semiconductor Devices, PhD. Thesis, University of California, Santa Barbara, 2019.

[33] K.C. Celio, A.M. Armstrong, A.A. Talin, A.A. Allerman, M.H. Crawford, G.W. Pickrell, and F. Leonard, IEEE Electron Device Lett. **42**, 1041 (2021).

[34] S. Guermazi, A. Toureille, C. Grill, and B. El Jani, Eur. Phys. J. AP **9**, 43 (2000).

[35] J.C. Gonzalez, K.L. Bunker, and P.E. Russell, Appl. Phys. Lett. **79**, 1567 (2001).

[36] T. Malinauskas, K. Jarasiunas, M. Heuken, F. Scholz, and P. Brückner, Phys. Status Solidi (c) **6**, (2009).

[37] Y. Horiike, T. Tanaka, M. Nakano, S. Iseda, H. Sakaue, A. Nagata, H. Shindo, S. Miyazaki, and M. Hirose, Journal of Vacuum Science & Technology A: Vacuum, Surfaces, and Films **8**, 1844 (1990).

[38] G.C. DeSalvo, C.A. Bozada, J.L. Ebel, D.C. Look, J.P. Barrette, C.L.A. Cerny, R.W. Dettmer, J.K. Gillespie, C.K. Havasy, T.J. Jenkins, K. Nakano, C.I. Pettiford, T.K. Quach, J.S. Sewell, and G.D. Via, J. Electrochem. Soc. **143**, 3652 (1996).

[39] K. Ikeda, S. Imai, and M. Matsumura, Applied Surface Science **112**, 87 (1997).

[40] D. Buttari, S. Heikman, S. Keller, and U.K. Mishra, in *Proceedings. IEEE Lester Eastman Conference on High Performance Devices* (IEEE, Newark, DE, USA, 2002), pp. 461–469.

[41] K.J. Kanarik, S. Tan, W. Yang, T. Kim, T. Lill, A. Kabansky, E.A. Hudson, T. Ohba, K. Nojiri, J. Yu, R. Wise, I.L. Berry, Y. Pan, J. Marks, and R.A. Gottscho, Journal of Vacuum Science & Technology A: Vacuum, Surfaces, and Films **35**, 05C302 (2017).

[42] H. Fukumizu, M. Sekine, M. Hori, K. Kanomaru, and T. Kikuchi, Journal of Vacuum Science & Technology A **37**, 021002 (2019).

[43] S. Ruel, P. Pimenta-Barros, F. Le Roux, N. Chauvet, M. Massardier, P. Thoueille, S. Tan, D. Shin, F. Gaucher, and N. Posseme, Journal of Vacuum Science & Technology A **39**, 022601 (2021).

[44] C. Gupta, C. Lund, S.H. Chan, A. Agarwal, J. Liu, Y. Enatsu, S. Keller, and U.K. Mishra, IEEE Electron Device Lett. **38**, 353 (2017).

[45] J.G. Nedy, N.G. Young, K.M. Kelchner, Y. Hu, R.M. Farrell, S. Nakamura, S.P. DenBaars, C. Weisbuch, and J.S. Speck, Semicond. Sci. Technol. **30**, 085019 (2015).

[46] J.-M. Lee, C. Huh, D.-J. Kim, and S.-J. Park, Semicond. Sci. Technol. **18**, 530 (2003).

[47] S.S. Cohen and G.S. Gildenblat, *Metal-Semiconductor Contacts and Devices. Volume 13, Volume 13*, (1986).

[48] B. Jacobs, M.C.J.C.M. Kramer, E.J. Geluk, and F. Karouta, Journal of Crystal Growth **241**, 15 (2002).

[49] J.H. Klootwijk and C.E. Timmering, in *Proceedings of the 2004 International Conference on Microelectronic Test Structures (IEEE Cat. No.04CH37516)* (IEEE, Awaji Yumebutai, Japan, 2004), pp. 247–252.

V. Summary and Future Outlook

In summary, a quantitative method to investigate the origins and dependence of hot electrons detected in Electron Emission Spectroscopy (EES) on carrier density n had been presented. Using the square root of the light output power (LOP), $\sqrt{LOP}$ as a proxy for the carrier density n, it was demonstrated in Chapter 2 that the dominant cause of droop in state-of-the-art industry blue LEDs is 3-body Auger recombination. Hot electron currents were also demonstrated to increase at a much faster rate than overflow currents with increasing current density. Thus, overflow currents cannot be the cause of droop. Thermal droop studies using the same devices showed a strong increase in trap-related recombination mechanisms with increasing temperature, pointing towards thermal activation of defects and hence increase in Shockley-Read-Hall (SRH) recombination and trap-assisted Auger recombination (TAAR) with increasing temperature as the cause for thermal droop.

Extending such analysis to UCSB grown green LEDs led to surprising detection of two high energy peaks at ~2.3 eV and ~1.7 eV above the conduction band minimum (CBM), as described in Chapter 3. These peaks, to the best of our knowledge, are the first detection of electrons from higher energy valleys on top of the side valley (SV) at ~0.9 eV above CBM (SV1). A correlation of their detection with thin pre-well InGaN layer, higher In composition in the quantum well, and presence of AlGaN in the active region was observed. The peaks were shown to have 2-body origins, indicating that they are generated by TAAR. It was thus

concluded that pre-well InGaN layers reduces defects in the active region. The location of these defects is likely at the (In)GaN/AlGaN interfaces.

With a quantitative method lined out, it is of interest to measure the absolute hot electron currents in order to quantify how large Auger currents are in comparison to the supplied current. It was demonstrated in Chapter 4 that EES can be used as a quantitative method for measurements of absolute currents. Through measuring emission current and spectra of *p*-*i*-*n* devices with variable *p*-GaN thicknesses, a minority electron diffusion length of ~24 nm was extracted, which is in good agreement with literature reported values. The extrapolated emission currents at the active region/*p*-GaN interface were in within a factor of two of the supplied current, with is the proof-of-concept for use of EES as a quantitative method for analyzing LEDs. Atomic layer etching (ALE) was investigated as a potential technique for systematic thinning of *p*-region of grown LEDs, demonstrating lithographic compatibility, smooth etches and low damage to the etched surface.

For the future, of utmost interest is comparing EES spectra across devices of variable QW In composition, from violet to red. We have demonstrated thus far that going from blue to green TAAR increases, but these samples are significantly different in epitaxial structures and growth conditions. A systematic study will be required for understand the green gap. If one compares single quantum well samples, a parallel study using differential carrier lifetime measurements can be performed to obtain the recombination coefficients and carrier density.

It is also important to investigate intervalley transfer in the *p*-region to decouple its effects from that of the active region for the absolute current measurements. This can be achieved by measuring *p*-AlGaN-*i*-*n* junctions with variable *p*-thicknesses. The AlGaN electron blocking layer to *i* (EBL-*i*) interface generates hot electrons which traverses the *p*-region in SV1. A

useful parallel experiment to that discussed in Chapter 4 involves *p*-*i*-*n* junctions with variable *i*-thicknesses. It should, in theory, be possible to match the emission currents to simulations to calculate the lifetimes of electrons in the unintentionally doped (UID) region (*i*-region). If these experiments can be replicated using InGaN, it will also allow for electron lifetime measurements in the UID quantum wells.

With all these experiments performed, it is possible to then grow a series of LEDs with variable *p*-GaN thicknesses to quantify the absolute Auger currents. Alternatively, ALE can be performed on state-of-the-art LEDs to systematically thin the *p*-region for these measurements. Similar quantitative analysis can then be performed to distinguish TAAR and 3-body Auger electron currents. In both cases, by measuring the absolute hot electron currents it also enables measurement of "missing current" not detectable in EES, which should correspond to SRH recombination. Thus, through EES a full quantitative measurement and analysis of an LED should be possible, distinguishing the contributions of the various recombination mechanisms.

Appendix A:

Electron Emission Spectroscopy System

The Electron Emission Spectroscopy system in University of California, Santa Barbara was designed to operate under ultra-high vacuum (UHV) conditions. A schematic of the chamber is shown in Fig. A1.

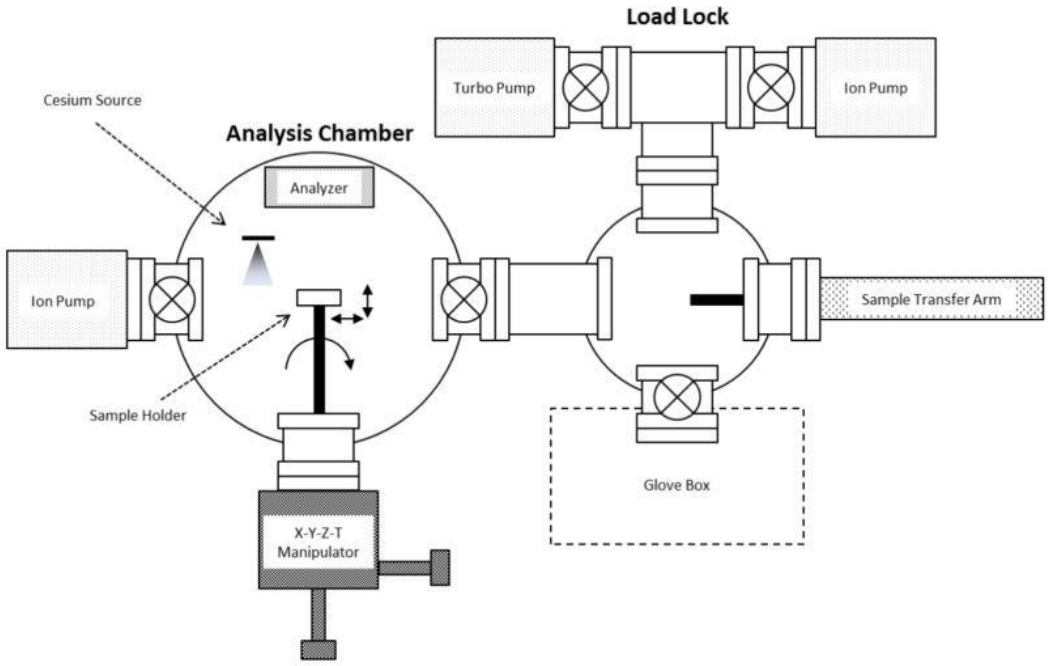

Figure A1: The schematic of the EES system, reproduced from Ref. 1.[1]

The load-lock chamber allows fast entry/exits of samples without sacrificing the UHV of the measurement chamber. The Electron Emission Spectroscopy system in University of California, Santa Barbara was designed operate at pressures of ~10^{-11} Torr to ensure large

mean free path of emitted electrons in the vacuum. Further details of the chamber design can be found in references 1 and 2.[1,2]

The energy of the emitted electrons was measured referenced to the Fermi level of the *p* contact using a Comstock AC-901B spherical sector electrostatic analyzer operated in constant pass energy mode. One can solve for the pass energy by solving Poisson's equation for a hemispherical analyzer that is invariant with respect to angular coordinates as depicted in Fig. A2:

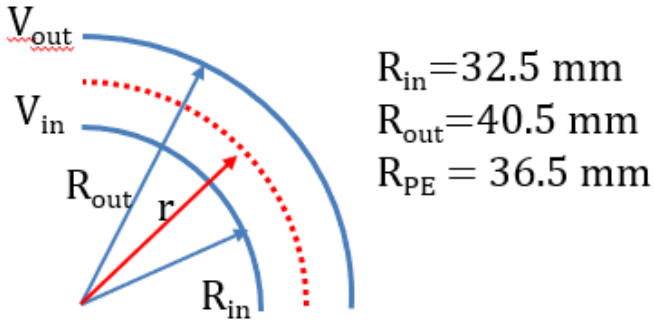

Figure A2: Schematic of the spherical sections comprising the energy analyzer.

$$\nabla^2 V = \frac{1}{r^2}\frac{\partial}{\partial r}\left(r^2 \frac{\partial V}{\partial r}\right) = 0$$

which has solution of form:

$$V_{out} - V_{in} = k \cdot \left(-\frac{1}{R_{out}} + \frac{1}{R_{in}}\right)$$

$$k = (V_{out} - V_{in}) \cdot \frac{R_{in} R_{out}}{R_{out} - R_{in}}$$

$$= 0.1645\ \Delta V \qquad \text{(A1)}$$

An electron travelling with speed v with corresponding kinetic energy, KE $= \frac{1}{2}mv^2$ in the analyzer along radius r experiences a centripetal force due to the electric field $\varepsilon(r)$:

$$\text{Electric field, } \varepsilon(r) = -\frac{\partial V}{\partial r}$$

$$= -\frac{0.1645 \cdot \Delta V}{r^2} \text{ V m}^{-1}$$

$$\text{Centripetal force, } \frac{mv^2}{r} = \frac{2\ \text{KE}}{r} = -q\varepsilon(r)$$

$$\therefore \text{KE}(r) = q \cdot \Delta V \cdot \frac{0.1645}{2r}$$

Only electrons with the right kinetic energy matching the pass energy, will maintain the right radius to exit the analyzer:

$$\text{KE}(R_{\text{PE}}) = q \cdot \Delta V \cdot \frac{0.1645}{2 \cdot 0.0365} \quad \text{(A2)}$$

$$= q \cdot \Delta V \cdot (2.2538)$$

For $\Delta V = V_{in} - V_{out} = 5$ V,

$$\text{Pass Energy} = 11.27\ eV$$

The resolution of the analyzer is given by:

$$\frac{\Delta E}{\text{PE}} = \frac{W}{R_{\text{PE}}(1 - \cos \emptyset) + L \sin \emptyset} \quad \text{(A3)}$$

$$= 0.8\ \%$$

where W is the entrance and exit slit diameter of 1 mm, $\emptyset$ is the angle subtended by the spherical sectors of 160°, and L is the distance from the exit sector to the center of the slit assembly.[3–5] It is straightforward to measure a spectrum by modifying the pass energy via

changing the voltage difference ΔV, however the energy resolution will vary across the spectrum. It is hence desirable to operate in the constant pass energy mode where the pass energy is fixed, and the energy of the incoming electrons is changed to match the spectrum by modifying the sample potential relative to the analyzer (or ground). A schematic of the configuration, and the relative potentials of the sample and analyzer, is shown in Fig. A3.

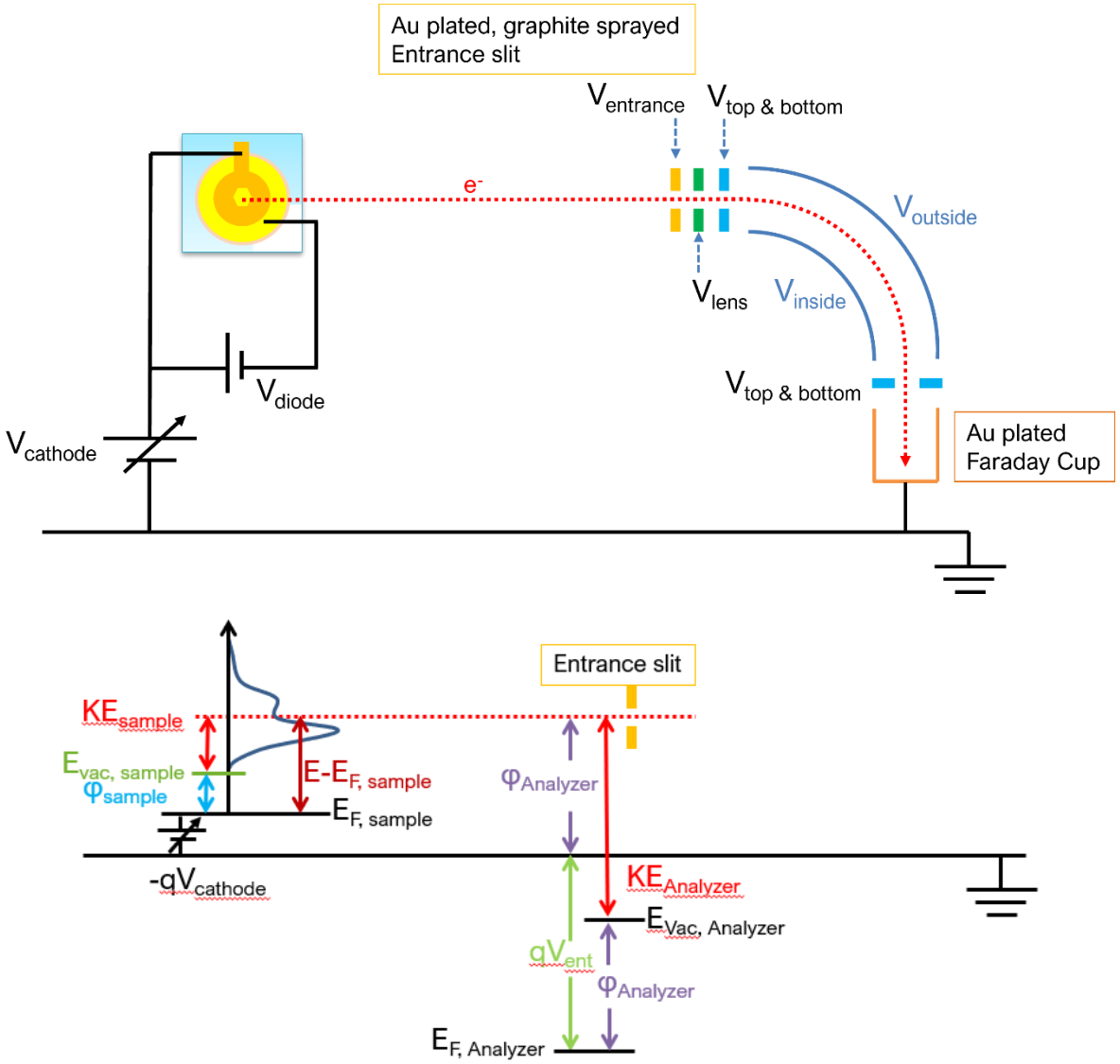

Figure A3: (a) Schematic of the constant pass energy mode configuration. (b) The relative potentials of sample, excited electrons and analyzer drawn referenced to ground.

We obtain:

$$-qV_{cathode} + \left(E - E_{F,sample}\right) = \varphi_{Analyzer} \tag{A4}$$

We can calibrate the 'workfunction', or energy barrier seen by an electron coming from infinity to the vicinity of the analyzer, $\varphi_{\text{Analyzer}}$ by shining a laser of energy $h\nu$ on a cesiated gold sample and utilizing the photoelectric effect. The use of cesium is to lower the workfunction of gold to increase yield and hence signal-to-noise ratio. The low energy threshold of the spectrum corresponds to the position of the vacuum level referenced to the sample's Fermi level. The high energy threshold must correspond to ballistic electrons photoexcited by the laser and by conservation of energy:

$$-qV_{cathode} + h\nu = \varphi_{Analyzer} \tag{A5}$$

In Fig. A4 the energy distribution curve (EDC) for photoemission of gold due to a 532 nm laser and the derivative (DEDC) are plotted.

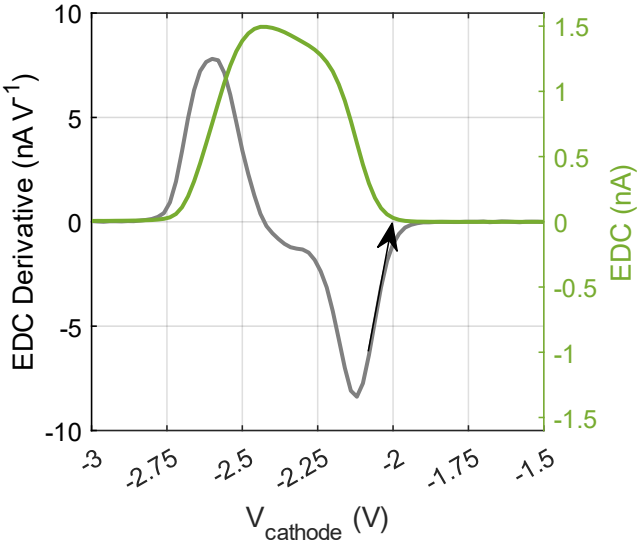

Figure A4: The EDC and DEDC curves for photoemission of gold due to a 532 nm (2.33 eV) laser.

The arrow indicates the zero-intercept position, V_{HET} from the high energy positive slope of the DEDC, or the high energy threshold. Eq. A5 becomes:

$$-qV_{\mathrm{HET}} + 2.33\ \mathrm{eV} = \varphi_{Analyzer} \qquad \text{(A5)}$$

References

[1] J. Iveland, Electron Emission Spectroscopy of InGaN/GaN Light Emitting Diodes, PhD. Thesis, University of California, Santa Barbara, 2015.

[2] D.J. Myers, Electron Emission Spectroscopy of III-N Semiconductor Devices, PhD. Thesis, University of California, Santa Barbara, 2019.

[3] I. Langmuir, Phys. Rev. **2**, 450 (1913).

[4] Comstock AC-901 Energy Analyzer.

[5] C. Tusche, Y.-J. Chen, C.M. Schneider, and J. Kirschner, Ultramicroscopy **206**, 112815 (2019).

[6] W.B. Joyce and S.H. Wemple, Journal of Applied Physics **41**, 3818 (1970).

Appendix B:

Fabrication Considerations for EES

A. The EES Device

Since it is in the utmost interest to introduce a clean sample and reduce impurities in the chambers, the mounting process is typically carried out in the nitrogen gas purged glove box connected to the load-lock fast entry-exit door. This meant that the mounting pins, which also functions as the electrical connection pins of the stage must be large, in millimeters, compared to standard LED device sizes, which are in micrometers. An intermediate large contact pad isolated from the p-layer is hence required. A schematic depiction is shown in Fig. B1.[1,2] The insulation layer is typically made of SiO_x which can be etched and patterned using buffered hydrofluoric acid (BHF) and deposited conformally using plasma-enhanced chemical vapor deposition (PECVD). If an alternative is desired, one must ensure that the insulator is chemically robust to hydrochloric acid (HCl), and preferably acidic piranha (sulphuric acid, H_2SO_4 : hydrogen peroxide H_2O_2 = 4:1), which are chemical reagents used for cleaning of samples prior to introduction in the EES system. In this sense, it is fortunate that Ga-face *c*-plane III-Nitrides are chemically robust.

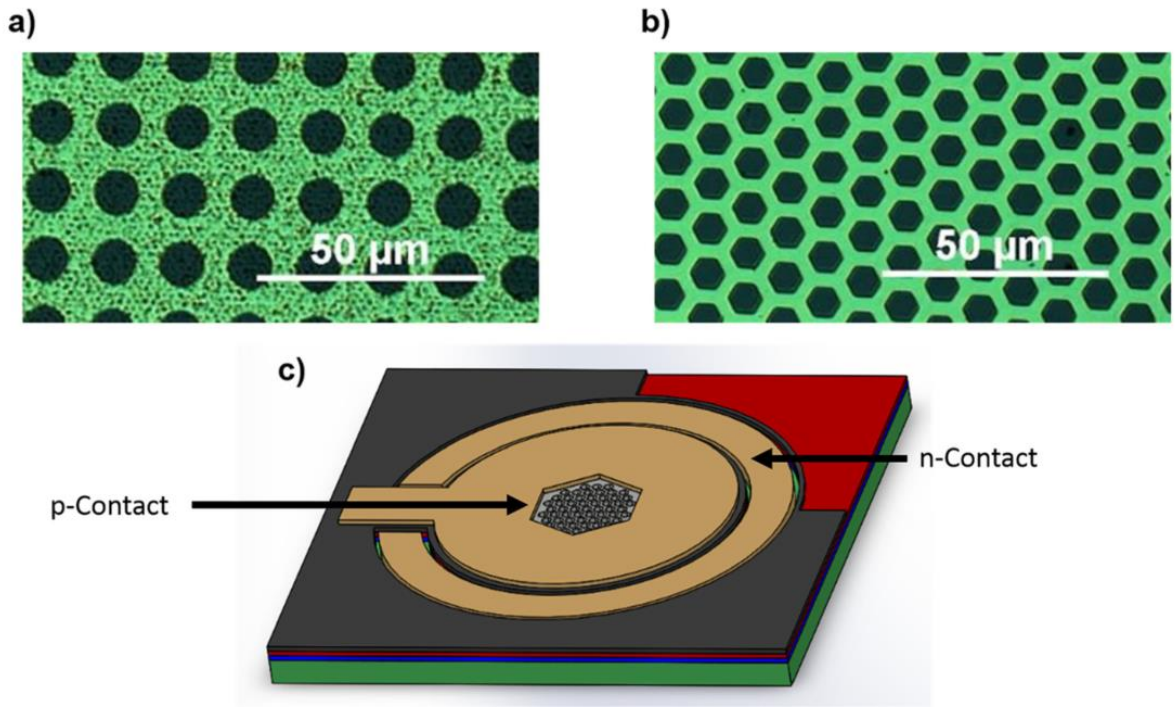

Figure B1: A circular aperture design was depicted in (a), which was improved upon to maximize exposed *p*-GaN region while ensuring sufficient current spreading within the apertures, as shown in (b).[1] The schematic of an EES device, not drawn to scale, reproduced from Ref. 1 and 2 was drawn in (c). The red layer corresponds to *p*-GaN, dark grey areas are SiO_x while golden layers correspond to metal contacts.

In previous generations of EES devices, it was also found that the emitted electrons must see a uniform electric field after emission, as large *p*- and *n*-pads will form a directional electric field pushing the electrons towards the *p*-pads and away from the analyzer.[3] For thicker *p*-layer samples, the signal-to-noise ratio will also be low, requiring larger exposed areas of the *p*-surface. This is complicated by the low conductivity of *p*-GaN, limiting the distance between any emitting *p*-surface and the nearest metal contact. The natural solution is to have an array of open apertures, of which the honeycomb array provides the best packing

density.[2] The device is hence a hexagon containing a honeycomb array, where each individual hexagon aperture has an apothem of typically 3.5 μm and the metal strips are 3 μm wide, as shown in Fig. B1. One can easily adjust the apothem and number of apertures to keep the total device size the same if current is sufficiently spreading within the apertures for the assumption of uniform injection to hold.

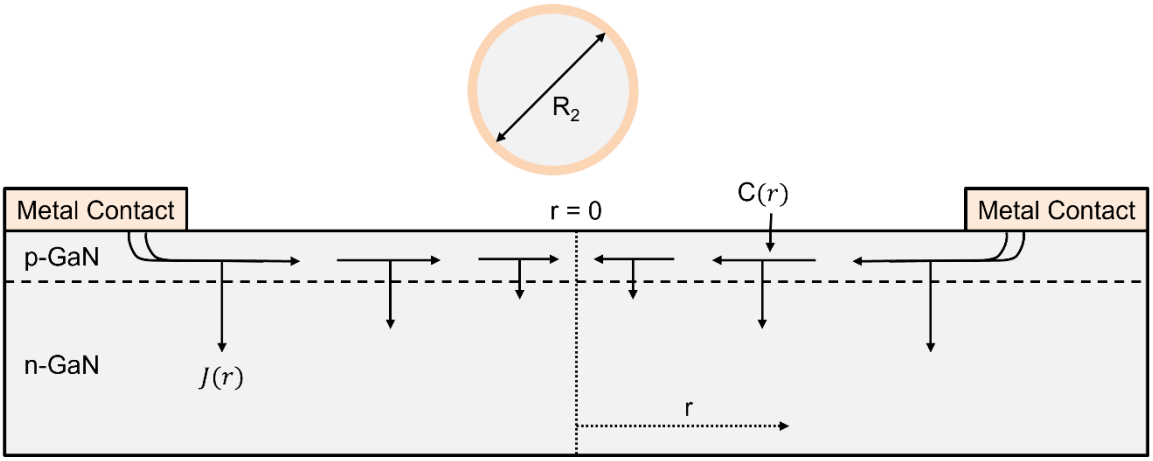

Figure B2: A schematic of current spreading in a circular aperture with radius R_2, which has an analytical solution and can be used to approximate current spreading profile in a hexagonal aperture. Diagrams reproduced from Ref. 4. $C(r)$ is the lateral current in the *p*-GaN.

We can approximate the current spreading profile of the current injected into the open *p*-GaN hexagons using analytical solutions for circular apertures on *p-n* junctions presented by W. B. Joyce in reference 3 and depicted in Figure B2.[4] The area under the metal contact is taken to be equipotential, hence the current density at different radius is taken to be constant under the metal contact and there is no lateral current. The current density at radius r inside the aperture is:

$$\frac{J(r)}{J(R_2)} = \left(1 - \frac{\rho I_2}{8\pi\eta k_B T t}\right)\left(1 - \left(\frac{r}{R_2}\right)^2\right)^{-2}$$

where I_2 is the total current supplied to the aperture, R_2 is the radius of the aperture, $\rho = R_s t$ is the bulk resistivity of the *p*-GaN, t the thickness of the p-layer, η the ideality factor of the diode and T is the temperature. $J(R_2)$, or J_2, is the current density at the metal edge. R_s can be obtained from circular transmission line measurements (CTLMs) while η can be obtained from fitting the $J - V$ curves of an LED. For the following discussion we will be using $\rho =$ 1.33 Ω cm.

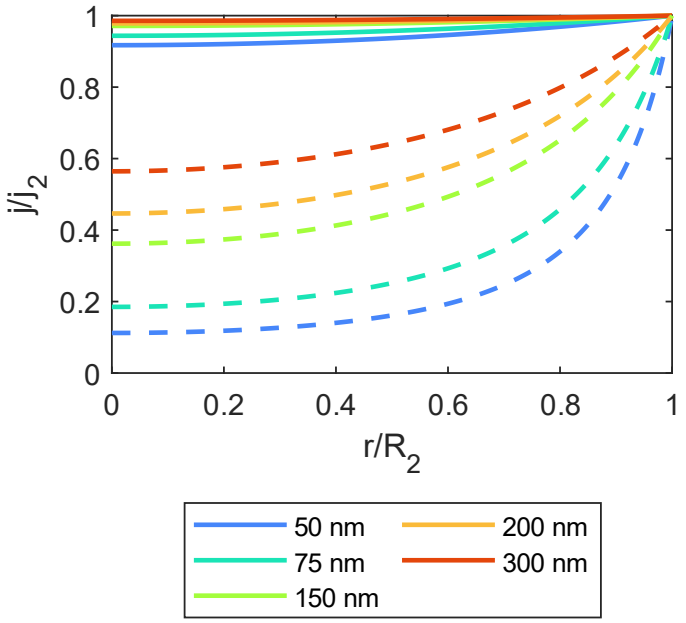

Figure B3: The current spreading profile across a circular aperture for 4602 circular apertures, corresponding to the EES device with 2.5 μm apothem hexagonal apertures. A clear dependence on p-GaN thickness is demonstrated, where larger thicknesses has better lateral current spreading. Solid

lines correspond to 1 mA current passing through the metal-semiconductor edge while dashed lines correspond to 45 mA.

The calculated current profiles for $\eta = 2.015$ and different *p*-thicknesses are shown in Fig. B3, where 1 mA and 45 mA of current is supplied to 4602 $\emptyset = 5\ \mu m$ circular apertures. The aperture size is implicitly included in the choice of I_2 for the calculation. Naturally the true current supplied should be lower due to the finite size of metal contacts, which is not accounted for in the equation. Hence this set of calculations serve as a worst-case scenario estimation for the diodes, while general trends hold and illustrate all the necessary diode physics.

With thicker *p*-thicknesses, the sheet resistance of the *p*-GaN reduces and there is less ohmic drop in the lateral direction. The carriers also have to travel a longer distance vertically to reach the diode. Combining these two effects, the lateral current profile is more uniform compared to the thinner *p*-GaN diodes. The 6-fold increase in sheet resistance from 300 nm to 50 nm translated to a drop of the aperture center current density, J_0 from $0.6J_2$ to $0.1J_2$. On average, this would imply a larger average current density in the aperture for the thicker *p*-GaN.

The more astounding outcome is the strong dependence on current supplied. Comparing 1 mA to 45 mA for 50 nm, which are typical current choices for the EES devices, J_0 reduced from $0.9J_2$ to $0.1J_2$. This can be understood as the larger potential changes arising from the finite resistance of the *p*-layer as per Ohm's Law. Since the current density at the junction is strongly dependent on the potential as illustrated by the diode equation, $J(\boldsymbol{R}) =$

$J_S\left[e^{qV(\boldsymbol{R})/\eta k_B T} - 1\right]$, where J_S is the reverse-bias saturation current density, the junction current density will decrease significantly with decreasing potential.

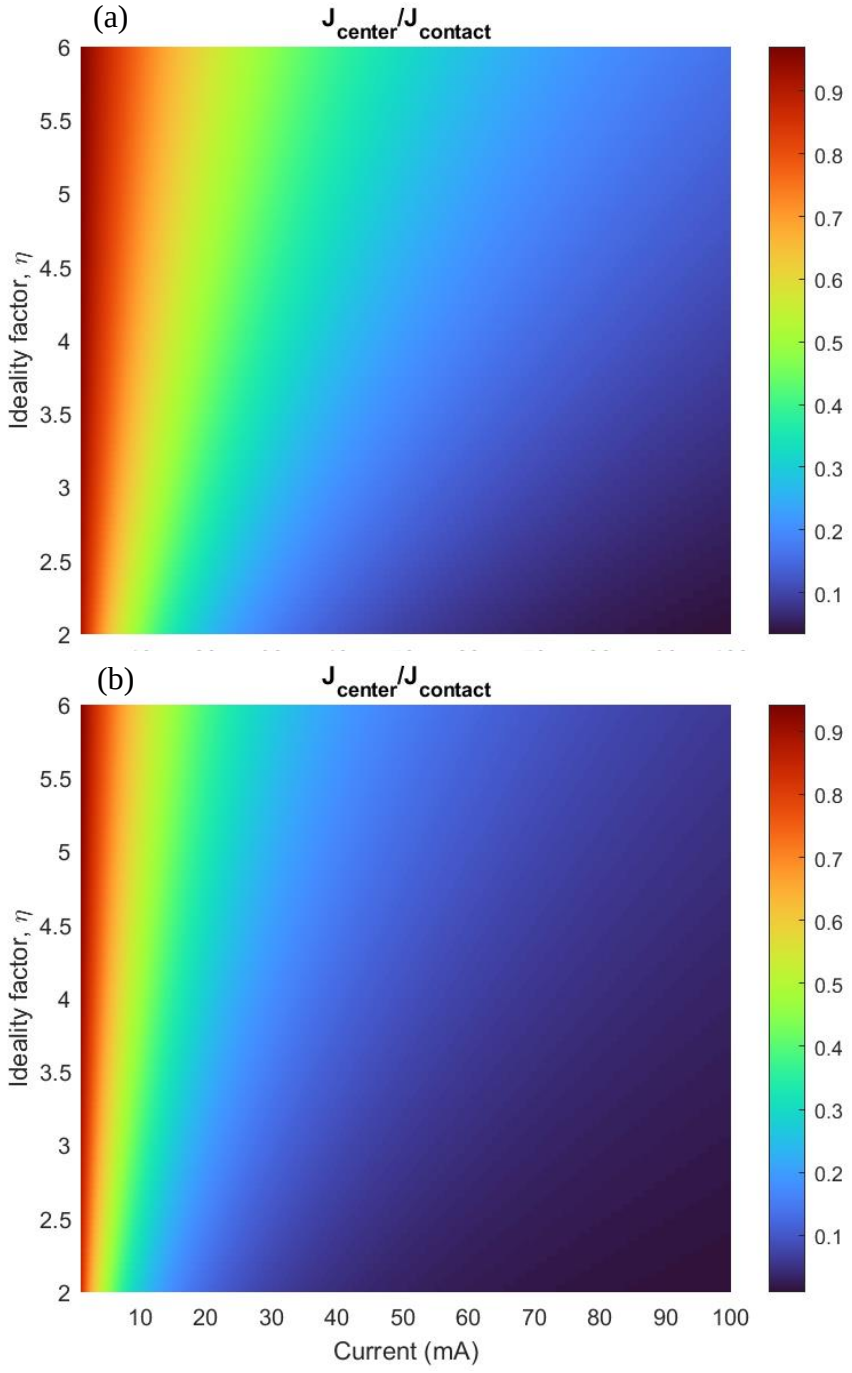

Figure B4: The current density at the center of the aperture is found to decrease with decreasing ideality factor and increasing current. The spreading profile is more uniform for (a) smaller aperture (4602 $\emptyset = 5\ \mu m$ apertures) than the (b) larger apertures (2257 $\emptyset = 7\ \mu m$ apertures).

One can compare the current spreading behavior by just comparing J_0, where a higher J_0 corresponds to a more uniform lateral current profile. The values of J_0 for various ideality factor and supplied currents are plotted in Figure B4 (a) and (b) for 4602 ($\emptyset = 5\ \mu m$) and 2257 ($\emptyset = 7\ \mu m$) circular apertures, respectively. The metal fill factors for the corresponding EES devices are 55% and 57%, respectively, which means these calculations should be fair comparisons between the two. The smaller aperture design has superior current spreading profiles compared to the larger aperture design. Even then for an ideal LED with $\eta = 2.0$, the 5 μm device has more than 50% current drop past 10 mA.

Thus far the current spreading profile was calculated for an infinitesimal metal ring contact, while the real device contains finite widths of the metal. This implies that the spreading profile thus far are the worst-case scenarios as there will be significant current flowing under the metal contacts (at least 50%). One can numerically solve for the correct

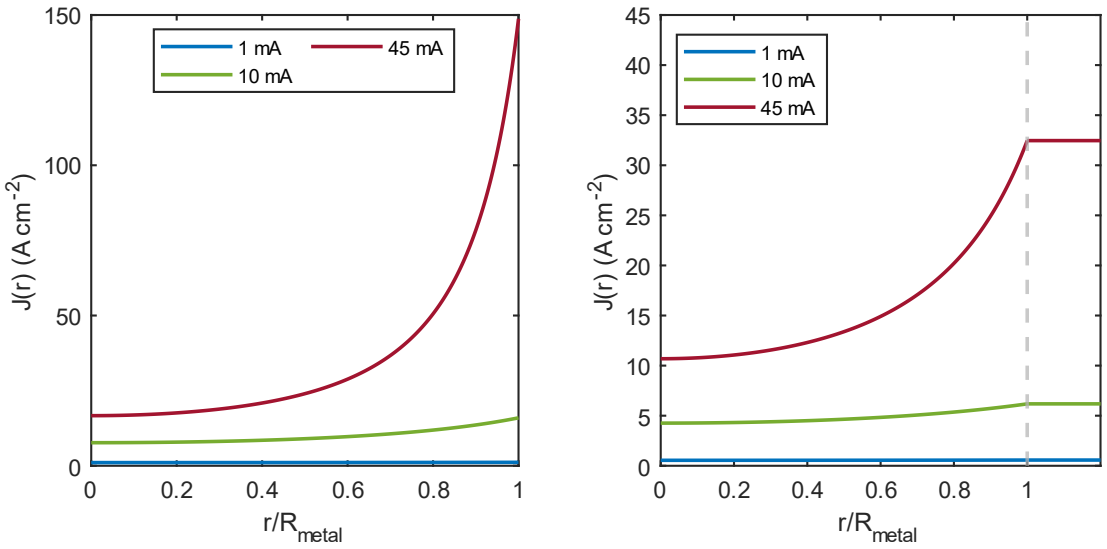

profile by assuming, reasonably, that the potential has no radial dependence under the metal and hence $J(\boldsymbol{R})$ must be constant.

Figure B5: Comparing the current spreading profile with infinitesimal (left) and finite (right) metal contact for $\emptyset = 5\ \mu m$ apertures.

Evidently from Figure B5, the inclusion of finite metal contact decreases the actual current supplied to the open aperture, preferentially spreading under the metal contact. For low current densities the profile is fairly uniform for both cases but at larger currents the difference is huge. Since 45 mA correspond to an average current density of 20 A cm^{-2} on the device, the inclusion of the metal contact clearly provides a better numerical outcome. Even so, a 50% drop from metal to center of aperture is calculated. This difference will be more significant in the droop regime.

The calculation for both $\emptyset = 5\ \mu m$ and $\emptyset = 7\ \mu m$ devices with finite metal contacts of widths $1\ \mu m$ and $1.5\ \mu m$, respectively, showed that the small difference in aperture sizes

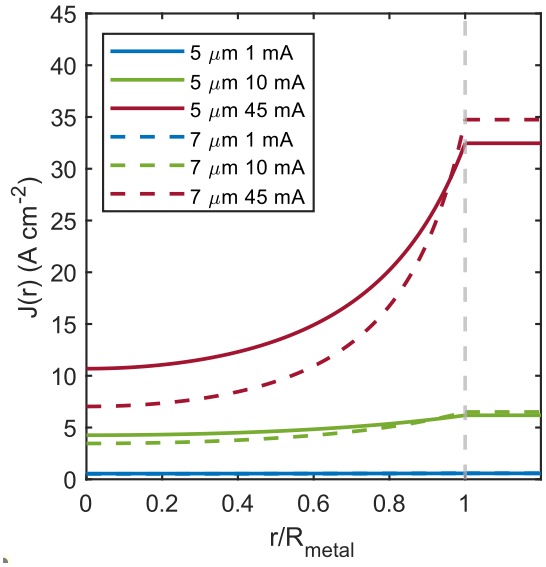

result in clear differences even at low currents of 5 mA, as depicted in Figure B6. . The current drop off is more significant in the larger aperture device.

Figure B6: Comparing the current spreading profile with finite metal contact for $\emptyset = 5\ \mu m$ and 7 μm apertures.

In theory we can always push the limits of lithography to obtain better filling factors with smaller aperture sizes and thinner metal contacts, but it will be extremely difficult in practice to obtain features smaller than a micron. The question is then: is it important to try? In the case of LEDs, the non-uniform current profile would change the local carrier density and hence local recombination rates. In the case of absolute quantification, one would expect a flattening of the emission current with decreasing thicknesses, which may result in lower measured diffusion lengths and/or extrapolated absolute currents in the absence of loss in the *p*-region. These effects are exacerbated by larger aperture designs, so there is interest in verifying these results experimentally to justify the extensive work required to realize the smaller aperture designs.

At this point, we return to a key assumption of the calculations – that the *p*-region is equipotential in the lateral dimension under the metal contact. This should be true – as metals spread current extremely well. For an ohmic contact, carriers should see little to no barrier and be injected uniformly from the metal to the resistive *p*-region. For a Schottky contact, as long as the barrier is uniform across the metal-GaN interface one would expect a similar outcome. This brings us to the next consideration in the EES device design – the *p*-contact metal choice. The metal choice ideally forms a good ohmic contact to the top *p*-layer, which typically in III-nitrides is *p*-GaN. A good ohmic contact ensures minimal resistive heating

during measurements – ensuring constant sample temperature to avoid complications from thermal effects and minimizing risk of decesiation. Given the loading nature of the system, the metal stack must also be physically and chemically robust – it must adhere well to the *p*-GaN, and is inert to BHF, HCl, and acidic piranha. On a side note, the typical EES *n*-contact metal stack Ti/Au forms a good ohmic contact and is thermally, physically, and chemically robust.

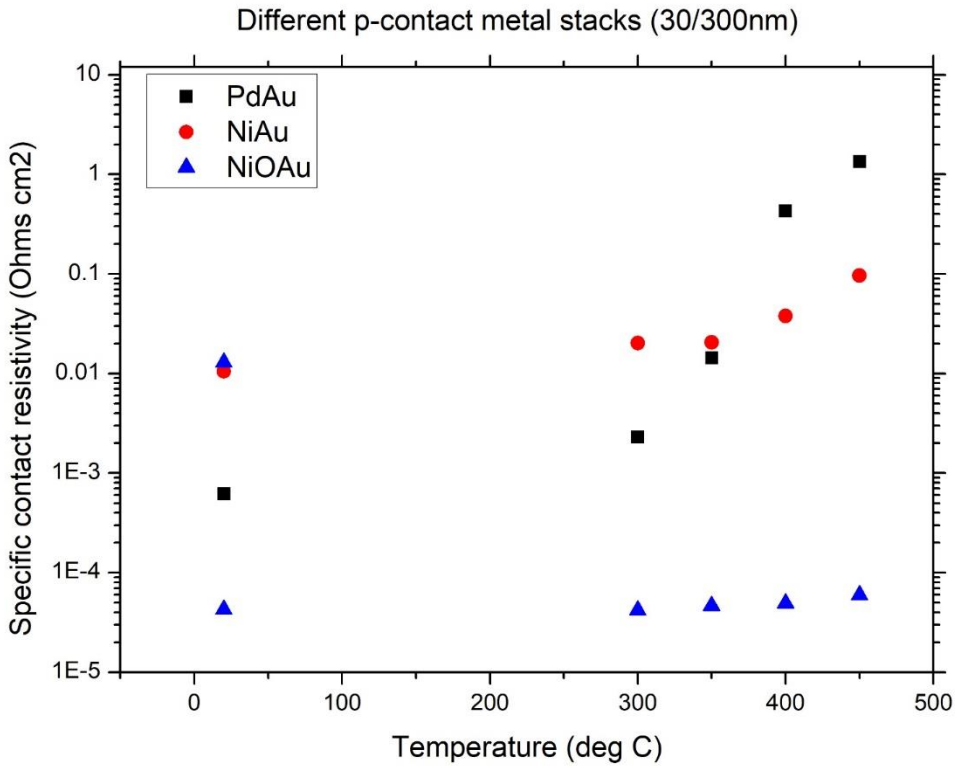

Figure B5: The thermal aging trend of various metal stacks contacted to p-GaN. Pd/Au is shown to degrade with long durations of thermal aging.

A typical metal stack is 30/300 nm Pd/Au. However, Pd/Au on *p*-GaN is shown to degrade with long durations of heating, as shown in Figure B5. The data was obtained by measuring

CTLMs after 30 mins of thermal aging in ~2×10^{-8} Torr high vacuum conditions, comparing as-deposited Pd/Au, Ni/Au and Ni/Au annealed at 500℃ in O_2 ambient (NiOAu). This is detrimental in thermal droop experiments which requires heating of the sample up to 200℃ for a minimum of 30 minutes, as a non-reversible change has taken place on the device which may complicate repetition of measurements and analysis. Another desired improvement is thermal robustness of the contact up to 400℃, which is the temperature to clean samples *in situ* for high vacuum systems. In both cases, NiOAu is outperforms in terms of specific contact resistivity. However, the attempt to change from PdAu to NiOAu for an EES device failed, showing unidentified phase transitions/alloying/degradation of the NiOAu metal, requiring more experiments for optimization.

B. The Heidelberg Maskless Aligner (MLA)

The UCSB Nanofabrication Facility is equipped with many different lithography tools – the classic Suss MJB-3 UV400 contact aligner, the industrial GCA 200 I-Line Wafer Stepper and finer ASML Deep-UV Stepper, the holographic interference lithography system for gratings, and a new form of direct write lithography, namely the Heidelberg Maskless Aligner (MLA) 150. The MLA is advantageous over the contact aligner by bypassing edge bead removal, has better resolution ($\geq$ 500 nm features), and machine vision assisted alignment. Most importantly, the MLA does not need a photomask, enabling rapid design changes fitting a research and development environment.

I will discuss a few tips on designing masks suited for use in the MLA150. The MLA150 accepts files in the form of .cif and .gds. These computer-aided design (CAD) files can be made using L-Edit or K-Layout, among other software. A brief tutorial on L-edit was provided in Ref. 1, while there are YouTube videos discussing use of K-Layout.[2] Firstly, in the spirit of all good mask design practices, the mask extents should be well defined and consistent across the different layers. This ensures that the different layers are the same size regardless of the true drawing areas, and aids in calculations of alignment mark positions.

The machine vision algorithms on the MLA150 accepts one of three different basic designs as alignment marks – i) the cross, ii) the box and, iii) lines. Alignment is performed by providing the tool with the expected positions of the center of the alignment marks (x, y) with respect to the to-be-exposed layer, irrespective of whether there is an actual cross/box/line drawn in the layer. Once a measurement was performed to obtain the position of the alignment marks (X, Y) on the sample with respect to the sample center, the sample rotation θ and offsets $(\Delta x, \Delta y)$ were obtained by:

$$\begin{pmatrix} X_1 & X_2 & \dots \\ Y_1 & Y_2 & \dots \end{pmatrix} = \begin{pmatrix} \cos\theta & \sin\theta \\ -\sin\theta & \cos\theta \end{pmatrix} \begin{pmatrix} x_1 & x_2 & \dots \\ y_1 & y_2 & \dots \end{pmatrix} + \begin{pmatrix} \Delta x & \Delta x & \dots \\ \Delta y & \Delta y & \dots \end{pmatrix}$$

A pictorial depiction is shown in Fig. B6. It is hence in the interest of the user to keep the coordinates (x, y) simple and be consistent in the choice of the origin position across layers – in essence, use mask extents, and keep the mask centered on origin or completely in the positive quadrant for all layers. MLA150 has the capability to auto-center masks drawn during design import. In the case of quarter wafers, keeping all drawn features in the positive quadrant for the first exposure layer allows easy offsetting of the sample to avoid exposing features on edge beads.

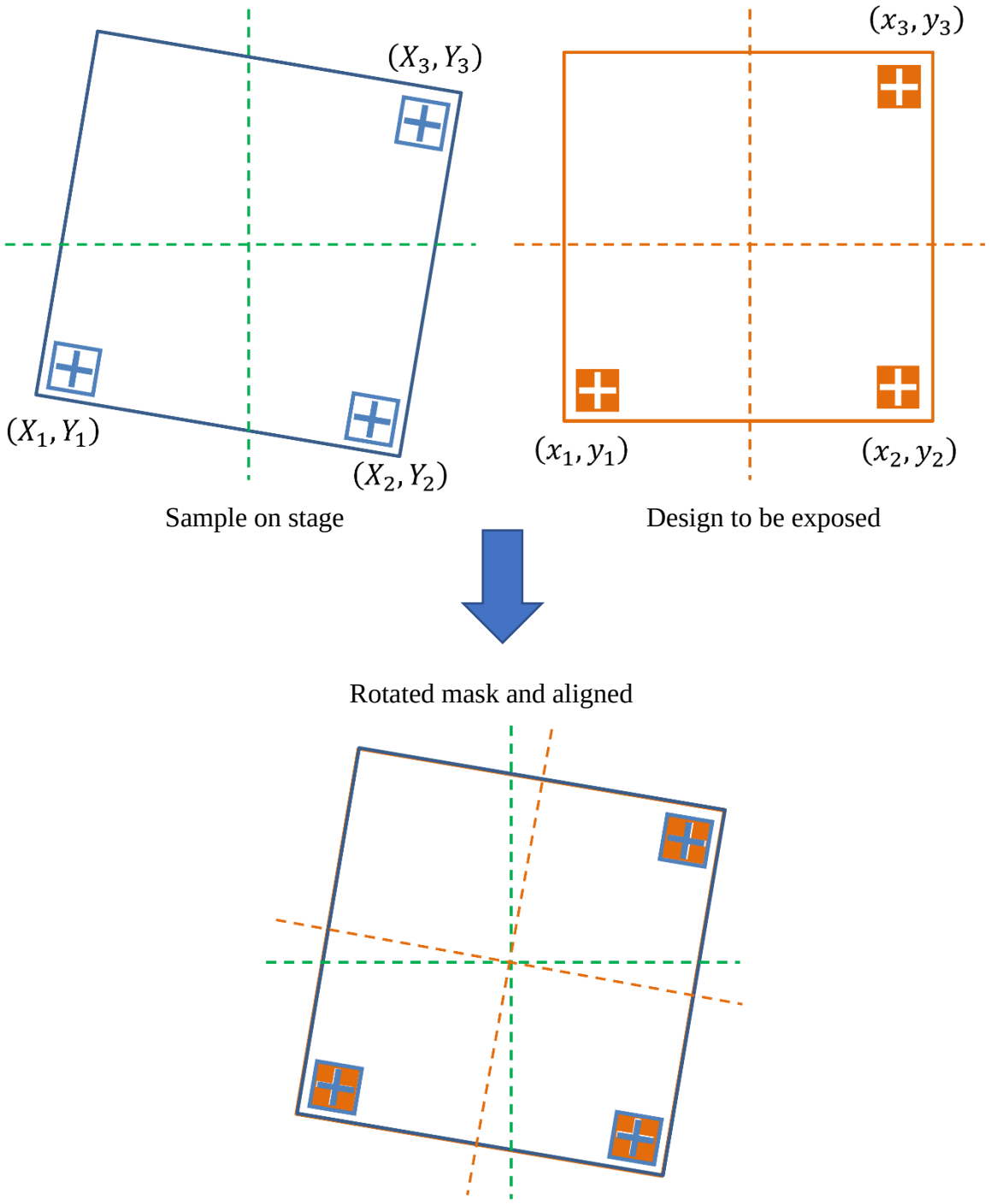

Figure B6: A loaded sample with its alignment features is drawn in blue, where their measured coordinates with respect to the stage center labelled. The green dashed lines represent the axes of the stage. The to be exposed layer is drawn in orange. Instead of rotating the loaded sample, in MLA150 the mask is rotated instead.

References

[1] D.J. Myers, K. Gelžinytė, W.Y. Ho, J. Iveland, L. Martinelli, J. Peretti, C. Weisbuch, and J.S. Speck, Journal of Applied Physics **124**, 055703 (2018).

[2] D.J. Myers, Electron Emission Spectroscopy of III-N Semiconductor Devices, PhD. Thesis, University of California, Santa Barbara, 2019.

[3] J. Iveland, Electron Emission Spectroscopy of InGaN/GaN Light Emitting Diodes, PhD. Thesis, University of California, Santa Barbara, 2015.

[4] W.B. Joyce and S.H. Wemple, Journal of Applied Physics **41**, 3818 (1970).